The Influence of Titanium on Metal - Ceramic Interfaces

Elad Nussbaum

The Influence of Titanium on Metal - Ceramic Interfaces

Research Thesis

SUBMITTED AS PARTIAL FULFILLMENT OF THE REQUIREMENTS FOR THE DEGREE OF MASTER OF SCIENCE IN MATERIALS ENGINEERING

Elad Nussbaum

Submitted to the Senate of the
Technion - Israel Institute of Technology

Nisan 5771 Haifa April 2011

Acknowledgments

This research thesis was done under the supervision of Prof. Wayne D. Kaplan, in the department of Materials Engineering at the Technion - Israel Institute of Technology.

I would like to express my gratitude to Prof. Wayne D. Kaplan for the guidance, patience and cooperation for this research.

I would like to thank Rafael - Advance Defense Systems, for giving me the opportunity and financial support to conduct and accomplish this research, for the use of different facilities and for endless support. Special thanks is given to Dr. Efraim W. and Yigal F. for the close support all along the way, Nathan G., Zvika B., Nava C., Avi M., Michal S., Yoram M. and Arie M. for supporting and backing me up when I was gone, Shlomit Z. and Ziv U. for consultation, brain storming, support and help in analysis and Dr. Shay Z. for consultation and help in XRD analysis and more.

I would also like to thank the members of the Metal-Ceramic Interface group at the faculty of Materials Engineering at the Technion - Israel Institute of Technology.

A special thanks is given to Hila Sadan-Meltzman for endless hours of discussion, TEM sessions, numerous phone calls and SMS and for guidance. Thanks is also given to Dr. Tzipi Cohen-Haims for FIB assistance, Dr. Yaron Kauffmann, Mor Baram and Miri Drozdov for TEM help and fruitful discussions, Mike Lieberthal for support and help in computing issues, Moshe Katz for the great technical support in conducting dewetting experiments and Dr. Alex Berner for consulting and great help in understanding and calculating detection limits.

Dedication

I would like to dedicate this work to my own family, my wife and two kids (who were born during the period of this research), for standing by me, supporting, helping and waiting patiently for the four long years this research lasted.

Table of Contents

Abstract ..... *I*

List of Symbols and Acronyms ..... *III*

1. Introduction *1*

2. Literature Survey *3*

2.1 Surface Energy of Solids *3*

2.2 ECS - Equilibrium Crystal Shape *8*

2.3 Thermodynamic Parameters at Metal-Ceramic Interfaces *14*

2.3.1 Contact Angles and Thermodynamic Work of Adhesion *14*

2.3.2 Extraction of Thermodynamic Parameters - Experimental Procedures *18*

2.3.2.1 Sessile Drop Experiments *18*

2.3.2.2 Dewetting Experiments *20*

2.3.2.3 Winterbottom Analysis *22*

2.3.2.4 Segregation to Surfaces and Interfaces *26*

2.3.2.5 Orientation Relationship (OR) at Solid-Solid Interfaces *27*

2.4 Metal-Ceramic Joining, Spreading and Reactive Spreading *28*

2.4.1 Adsorption/Ridge Controlled Spreading (Adsorption First Approach) *31*

2.4.2 Reaction Product Controlled Spreading *37*

2.5 Gold - Titanium - Sapphire System *43*

2.5.1 Equilibrium Shapes *46*

2.5.1.1 Equilibrium Shape of Gold *46*

2.5.1.2 Equilibrium Shape of Sapphire *47*

3. Research Goals *48*

4. Experimental Methods and Procedures *49*

4.1 Dewetting and Equilibration Experiments (Au-Ti-Sapphire System) *49*

4.2 Microstructural Characterization of a Commercial Active Gold Brazing Alloy *52*

4.3 Characterization Methods 53
4.3.1 TEM Sample Preparation 54

5. Results 55

5.1 Dewetting and Equilibration Experiments (Au-Ti-Sapphire System) 55
5.1.1 Particle Shape and Morphology 55
5.1.2 SEM and EDS Characterization 56
5.1.3 TEM Characterization 58
5.1.4 Particle Shape and Morphology - 2nd Dewetting Experiment 63
5.1.5 TEM Characterization - 2nd Dewetting Experiment 66
5.2 Commercial Active Brazing Alloy - Gold ABA® 77
5.2.1 SEM and EDS Characterization of the Gold-Sapphire Interface 77
5.2.2 TEM Characterization of the Gold-Sapphire Interface 79

6. Discussion 83

6.1 Dewetting and Equilibration Experiments 83
6.1.1 Equilibrated Particle Shape and Morphology 83
6.1.2 Gold-Sapphire Interface 90
6.1.3 Au(Ti)-Sapphire Interface Energy 91
6.2 Gold-ABA®-Sapphire Interface Structure 94

7. Summary and Conclusions 98

8. Recommendations for Future Work 101

Appendix 1 - Detection Limit - Theory and Calculations 102
A.1.1 Theoretical Background 102
A.1.2 Thin Specimens 104
A.1.3 Detection Limit Calculations 110

References 114

List of Figures

Figure 1: Surface energy variation with orientation around the edge of the stereographic triangle. Curves are shown for the pure solvent (Ni), and for a Ni-0.1at%Au alloy at three temperatures [9]. 4

Figure 2: Anisotropy of surface energy of TiO_2 (rutile), computed based on first principles calculations [11]. 5

Figure 3: Secondary electron SEM image of a gold particle equilibrated on c(0001) sapphire for 100 hr in air, exhibiting (111) facet at the top [17]. 8

Figure 4: SEM image of an equilibrated lead crystal at 200°C [18], displaying (111) and (100) type facets at the surface. 8

Figure 5: High magnification SEM micrograph of an individual pore exposed by polishing after 24 hr anneal at 1900°C of a sapphire substrate. Pore showing that c-, r-, and a-type plane facets formed during annealing [19]. 9

Figure 6: Two dimensional section of the Wulff plot for an FCC crystal oriented along $<1\bar{1}0>$ direction [21]. 9

Figure 7: Equilibrium crystal shape of copper grown on sapphire: (a) photomicrograph viewed along a <110> direction, (b) schematic ECS produced using Wulffman freeware and (c) one quarter of the ECS from the Wulff construction (right) [25]. 11

Figure 8: Cross section of a Pd cluster based on the Wulff construction using theoretical surface energies for the three low index Pd surfaces. (110) facet develops only for clusters with $w \geq 80\,\overset{0}{A}$ [26]. 12

Figure 9: Schematic illustration of a liquid metal droplet equilibrated on a flat solid substrate. Different surface and interface energies and contact angle are marked. 15

Figure 10: Work of adhesion and observed adhesive strength vs. interfacial free energy [6]. 16

Figure 11: Tensile strength as a function of W_{ad} for common FCC metal/sapphire (0001) interfaces [35]. 16

Figure 12: Schematic illustration of dihedral angles formed at the triple junction upon substrate dissolution. 17

Figure 13: Experimental evidence of the dissolution of the substrate under the molten metal drop at high temperatures: (a) sapphire surface after the removal of small Ni drops after 12 hr at 1500°C [38]. (b) Sapphire surface after the removal of Al drop after 2 hr at 900°C [4]. 18

Figure 14: Schematic illustration of (a) receding contact angle and (b) advancing contact angle. 20

Figure 15: Evolution of a 3000 $\overset{0}{A}$ thick gold film on a graphite substrate annealed under UHV at 1000°C for: (a) 15 min, (b) 10 hr, (c) 50 hr, (d) 70 hr, images taken from [45]. 21

Figure 16: Two particle-substrate configurations describing partial wetting: (a) where $\gamma_{PV} > (\gamma_{SP}-\gamma_{SV}) > 0$, in which $\theta > 90^0$ and (b) where $-\gamma_{PV} < (\gamma_{SP}-\gamma_{SV}) \leq 0$, in which $\theta < 90^\circ$ [47]. 25

Figure 17: Schematic illustration of the expected shape of a ridge that would form by local diffusion in response to horizontal and vertical forces at the junction [81]. 32

Figure 18: Schematic illustration of reactive spreading introducing the four stages [82]. 34

Figure 19: Schematic presentation of the RPC model describing the change in contact angle and interfacial reaction product layer in a reactive metal-ceramic system [93]. 38
Figure 20: (a) Drop base radius vs. time curve for the reactive Al/C_v system at 1100K in a vacuum of 10^{-3} Pa [93]. (b) Schematic representation of the Al/C_v system in light of the RPC model [91]. Here, $\theta_1 = \theta_s$ and $\theta_F = \theta_{Al/Al_4C_3}$ 39
Figure 21: Schematic representation of the bulk sapphire structure: (a) three dimensional view of a rhombohedral unit cell, (b) two dimensional view of the unit cell projected in the <11$\bar{2}$0> direction showing atomic arrangement and Al and O layers [] and (c) top view illustration of the (0001) sapphire surface [113]. 44
Figure 22: Layered coating sputtered on c(0001) sapphire substrate for dewetting experiments. 49
Figure 23: (a) Schematic illustration of furnace setup used for dewetting experiments. (b) Au-Ti phase diagram [129]. Working point chosen (titanium concentration and dewetting temperature) is marked in red. 50
Figure 24: Secondary electron SEM micrographs of dewetted particles equilibrated on c(0001) sapphire substrate after 24 hr at 900°C, in an Ar+7% H_2 atmosphere. 52
Figure 25: (a) Secondary electron (SE) SEM micrographs of dewetted particles on c(0001) sapphire, exhibiting unexpected structure growth on top of the surface. Particles were equilibrated for 24 hr at 900°C. (b), (c) High resolution SE-SEM micrograph showing structure growth on curved surfaces and on clearly visible facets. 55
Figure 26: X-ray diffraction 2θ scan (intensity Vs. 2θ) using CuKα radiation (35°<2θ<145°) taken from the dewetted sample (24 hr at 900°C). 56
Figure 27: Backscattered electron SEM micrograph of particle equilibrated on c(0001) sapphire for 24 hr at 900°C. No phase contrast is visible across the surface of the particle. 57
Figure 28: (a) Secondary electron SEM micrographs of the eutectic microstructure that formed on the equilibrated particle surface (900°C for 24 hr on c(0001) sapphire), combined with EDS scans showing the presence of Si. (b) No Si is detected on the Au free particle surface. 57
Figure 29: Secondary electrons high resolution SEM micrograph (FEI Strata 400-S FIB) of gold particle equilibrated on c(0001) sapphire at 900°C for 24 hr, exhibiting a clean surface and clearly visible faceting. 58
Figure 30: High Angle Annular Dark Field (HAADF) STEM micrograph (FEI Titan 80-300 kV S/TE) of the cross sectioned and equilibrated particle (24 hr at 900°C) revealing the facets that formed at the surface. A step is noticeable at the gold particle-sapphire interface (circled). 59
Figure 31: (a), (b) High Angle Annular Dark Field (HAADF) STEM micrographs (FEI Titan 80-300 kV S/TE) showing two nanometer sized particles rich in titanium residing next to the cross sectioned gold particle. Micrographs are shown together with the left side of the EDS spectra taken from the marked red circles, (a.1) and (b.1), respectively. Titanium concentrations are 15.2 and 5.3 at.% in (a) and (b), respectively. 60
Figure 32: XRD results of: (a) pure Ti plate and (b) Ti plate that was put through the same dewetting experiment (900°C for 24 hr under constant flow of Ar+7%H_2). 61

Figure 33: Evolution of a 3000 $\mathring{A}$ thick gold film on a graphite substrate annealed under UHV at 1000°C for: (a) 15 min, (b) 10 hr, (c) 50 hr and (d) 70 hr. Images taken from [132]. 62

Figure 34: Secondary electron SEM micrographs of dewetted particles (2nd dewetting experiment) equilibrated on c(0001) sapphire substrate after 1 hr at 900°C, in atmosphere of pure argon (99.9995%) passed through an oxygen trap: (a) tilted at 52°, (b) and (c) taken at 0°. Slight discoloration is visible due to sample charging effects in (a) and surface texture in (c) is due to Cr deposition. Small facets are visible on the surface in (b) and (c). 64

Figure 35: XRD results of the sample from 2nd dewetting experiment. Dewetting was carried out at 1100°C and equilibration at 900°C for 1 hr. Entire process was carried out under a constant flow of gettered 99.9995% Ar (yielding a $P(O_2)$ of 10^{-21} atm). 65

Figure 36: (a) High Angle Annular Dark Field (HAADF) TEM micrograph of a cross sectioned gold particle dewetted at 1100°C and equilibrated at 900°C for 1 hr under gettered 99.999% Ar. (b) EDS spectrum from the area marked by three red arrows in (a), indicating the local enrichment of Ti near the particle's free surface. Titanium concentration detected there was ~0.4 at.%. 67

Figure 37: (a) Secondary electron SEM micrograph taken at the FIB of a particle where Ti was detected at the surface. (b) Left side of EDS spectra taken from the point marked with a red cross in (a) indicating the presence of Ti. 68

Figure 38: Aberration corrected TEM micrograph (C_S=-4.6 μm) of a cross sectioned particle. Particle and substrate are coated with a thin layer of Cr followed by a carbon deposition layer for particle protection. 69

Figure 39: High Angle Annular Dark Field (HAADF) TEM micrograph of the gold-sapphire interface together with EDS spectrum, showing the presence of Ti at the interface. 70

Figure 40: (a) High Resolution aberration corrected TEM (HRTEM) micrograph (C_S=-4.6 μm) of the gold-sapphire interface (2nd dewetting experiment), (b) digital magnification of (a) together with the dimensions of the partially ordered adsorbate layer. 71

Figure 41: (a) Exit wave (phase) reconstructed from 21 aberration corrected (C_S=-4.6 μm) HRTEM micrographs of the gold-sapphire interface (2nd dewetting experiment), (b) digital magnification of (a). 72

Figure 42: High Angle Annular Dark Field (HAADF) micrographs together with EDS spectrums of (a) triple point and (b) free sapphire surface indicating the presence of Ti in both places. (c) High resolution aberration corrected TEM micrograph (C_S=-3.4 μm) of the sapphire surface where Ti was detected. 74

Figure 43: (a) High Angle Annular Dark Field (HAADF) TEM micrograph of the triple point of the gold particle. An adsorption layer of a Ti-containing compound on the sapphire substrate is indicated by orange arrows. (b) High Resolution aberration corrected TEM (HRTEM) micrograph (C_S=-3.4 μm) of the triple point. Cr protective layer is also visible. An area containing Ti and O peaks alone is confined by a red line. 75

Figure 44: (a) Bright Field TEM micrograph and (b) selected area diffraction pattern for the equilibrated gold particle and the sapphire substrate. The diffraction pattern is oriented the same as the BF micrograph. 76

Figure 45: (a) Backscattered Electrons SEM micrograph (FEI E-SEM QUANTA 200) of a cross sectioned sample of gold-ABA® alloy, vacuum brazed between two c(0001) sapphire discs at 1080°C for 30 min, showing general structure of the interface. (b), (c) EDS spectra of the boxes marked as (a) and (b), respectively. (d) BSE SEM and EDS line scan across the interface showing Ti enrichment in black contrast areas. 78

Figure 46: High angle annular dark filed (HAADF) STEM micrograph of the metal-ceramic interface between gold-ABA® and c(0001) sapphire. Non-continuous and isolated 'islands' of reaction products (black) are visible. Interface is indicated by broken green line. 80

Figure 47: (a) High Resolution STEM micrograph of the reaction product grain shown in the red box in Figure 46 and (b) EDS spectra of a scan across that grain marked in (a) showing the presence of Ti and O alone, indicating that this is a grain of titanium oxide (Ti_xO_y), probably TiO_2 or Ti_3O_5. 81

Figure 48: (a), (b): High resolution transmission electron microscopy (HRTEM) images of different titanium oxides that formed at the gold ABA®-sapphire c(0001) interface. Ordered grains are visible. 82

Figure 49: Gold-silicon phase diagram [136]. 84

Figure 50: Comparison of gold dewetted on sapphire: (a) this work, gold+1.86 at.%Ti dewetted on c(0001) sapphire under constant flow of Ar+7%H_2, equilibrated at 900°C for 24 hr, and (b) Sadan and Kaplan [17], pure gold dewetted on c(0001) sapphire and equilibrated at 1000°C for 100 hr in air. 85

Figure 51: SEM micrograph of (a) pure gold crystallites and (b) gold crystallites alloyed with 1.0 at.% Ge on α-SiC, both after solid state annealing at 1123K for 72 hr [123]. 86

Figure 52: Schematic γ-plot of gold-sapphire interface energies, displaying two cusps relating to Au(200) and Au(111) (red) that were detected as preferred orientations on sapphire by Sadan and Kaplan [17] and Fecht and Gleiter [59], compared to Au-1.86 at.% Ti, where only Au(111) was detected as a preferred orientation (current work, blue). 87

Figure 53: Calculated γ-plot showing surface energy variation with orientation for a Ni-0.1 at. % Au alloy at three different temperatures and for the pure solvent (Ni). 88

Figure 54: Schematic γ-plot of the convoluted ECS in two dimensions for an fcc single crystal: (a), (b) above the surface and (c), (d) interface energy. Dashed red line and blue line represent pure Au and Au-1.86 at.% Ti on c(0001) sapphire, respectively. The change caused by the addition of titanium is seen in (d) where cusps of {111} interface planes become deeper while cusps of {100} interface planes remain unchanged. 89

Figure 55: Schematic illustration of the triple junction between the gold particle, sapphire substrate and vapor phase [140]. Different surface and interface energies are presented, together with torque terms. 91

Figure 56: Aberration corrected TEM micrograph (C_S=-4.6 μm) of the cross sectioned gold particle from the 2nd dewetting experiment where Ti was detected at the gold-sapphire interface, together with R_1 and R_2 measurements relating to Winterbottom's analysis [47]. R_1 and R_2 were measured from the lamella that was extracted from the center of the particle. 93

Figure 57: Illustration of interaction/excited volume created in thick and thin samples, showing the basic differences in probe size, the volume that is excited and sample thickness. Image taken from []. . 102
Figure 58: (a) Illustration of beam broadening inside a thin specimen. (b) Beam broadening as a function of specimen thickness at three different accelerating voltages, for the same material. 103
Figure 59: Adsorption path length, x, and detector angle, α. 106
Figure 60: Illustration of the interaction of the incident beam with the specimen used to formulate the fluorescence correction term. Image taken from [153]. 107
Figure 61: Backscattered electrons SEM micrograph of the microstructure of AuTi sample prepared in an electrical arc furnace. Three phases are visible. 111
Figure 62: High angle annular dark field TEM micrograph of the white phase grain together with position of 15 EDS scan boxes taken along it. 112

List of Tables

Table 1: Contact angles of common liquid metals used as base metals for brazing alloys on Al_2O_3. 29

Table 2: Contact angles and interface energies of the gold-sapphire system. (*) These values were determined using surface energy values of 1.4 [J/m^2] for Au(111) and 1.24 [J/m^2] for sapphire (0001). 45

Table 3: Measured and integrated intensities, together with simulated intensities of gold reflections from XRD of the 2nd dewetting experiment. Simulated intensities were taken from gold's JCPDS card (#04-0784). A preferred orientation of Au(111) on c(0001) sapphire is noticeable. 66

Abstract

Metal-ceramic interfaces are at the heart of numerous industrial and research applications in many fields of interests. Common fields of usage are microelectronics, medicine, automotive and aerospace, thin and thick films technology, vacuum systems, lasers and much more. As such, they have been studied and investigated since the middle of the 20^{th} century. Two common routes to create metal-ceramic joins are metallization and active brazing processes. In the first process, a metallic layer is deposited on the ceramic surface that is later brazed to a metal member, while in the second process, active element additions (such as Ti, V, Zr, etc) to brazing alloys allows one step joining to be carried out. Two leading theories for the role of the active element in the reactive wetting/spreading are common today. The first (held by N. Eustathopoulos et al.) claims that improvement in wetting is due to the creation of a reaction product at the interface (by reaction of the active element with the ceramic) while the second (held by E. Saiz, R. M. Cannon and A. P. Tomsia et al.) claims that adsorption of the active element alone at the interface is responsible for the improvement in wetting. This work is aimed at clarifying the effect titanium has (as an active element addition) on metal-ceramic interfaces.

A complex gold-titanium-gold thin film was dewetted on basal plane sapphire substrates in the liquid state, under controlled atmosphere. Dewetting resulted in the formation of a large number of micron and sub-micron particles that were then annealed in the solid state at $900^{\circ}C$ for equilibration. Dewetted samples were examined using XRD to determine the preferred orientation, and SEM and TEM for gold-sapphire interface characterization.

The particles that were created during dewetting were round in shape and contained small facets. XRD showed that Au(111) is the preferred orientation of the particles on the c(0001) sapphire substrate and the same low-index orientation relationship between gold and sapphire was confirmed for a single particle using electron diffraction. Since titanium is not expected to segregate to the particle surface (due to its higher surface energy compared to gold), the fact that only one preferred orientation was observed indicates that titanium has adsorbed at the metal-ceramic interface where it increased the anisotropy of the interface energy.

Characterization of the gold-sapphire interface revealed that a partially ordered adsorbate layer containing titanium formed, with a thickness of ~1 nm. Titanium excess at the gold-sapphire interface was determined to be 2.2 $^{\text{Ti atoms}}/_{\text{nm}^2}$, corresponding to an average of 0.2 monolayers. Titanium adsorption was also observed on the sapphire surface adjacent to the gold particles. Titanium excess at the sapphire surface was determined to be 4.6 $^{\text{Ti atoms}}/_{\text{nm}^2}$, corresponding to 0.5 monolayers.

As a means of general comparison to conventional active brazing, a ceramic-ceramic joint was prepared by vacuum brazing two c(0001) sapphire substrates with gold-ABA® active brazing alloy. The interface formed after brazing at 1080°C for 30 min, was characterized using TEM. Non-continuous reaction products ("islands") of titanium oxides formed at the interface, due to reduction of the sapphire surface by titanium. It is not known whether these oxides formed during brazing or during cooling, since the sample was examined only after the brazing process.

The results obtained from this work show that titanium adsorbs at the gold-sapphire interface and support the theory that reduction of interface energy and improvement in wetting are achieved by adsorption of the active element at the metal-ceramic interface.

List of Symbols and Acronyms

γ	Surface energy
Γ	Excess surface concentration
T	Absolute temperature
R	Universal gas constant
C_i	Impurity concentration
W	Reversible work
$r_{(hkl)}$	Radius vector
$\boldsymbol{n}_{\{hkl\}}$	Normal to (hkl) plane
t_i	Unit vector in the plane of the i^{th} interface
t	Time needed for equilibration
D_S	Surface diffusivity
v	Number of atoms per unit of surface area
Ω	Atomic volume
a	Lattice parameter
k	Boltzman's constant
r	Particle radius
$\gamma_{SV}, \gamma_{SL}, \gamma_{LV}$	Substrate-vapor, substrate-liquid and liquid-vapor surface energies, respectively
θ	Contact angle
W_{ad}	Thermodynamic work of adhesion
h, r_{MAX}	Height and maximum radius of droplet, respectively
ρ, σ	Density and surface tension of the metal, respectively
ϕ_S, ϕ_L, ϕ_V	Equilibrium dihedral angles in the solid, liquid and vapor, respectively
F	Helmholtz free energy
dy	Variation in the free energy of the system
C_S, C_b	Surface and bulk concentrations, respectively
ΔG^{segr}	Free energy for mole solute segregation
t_{cc}	Spreading time
η	Liquid viscosity
r_o	Initial droplet radius
$v_{cr}^{adsorption}$	Critical spreading velocity
D_{liq}	Diffusivity in the liquid
X_R	Adsorbate fraction in the liquid
D_{sl}	Diffusion coefficient at the solid-liquid interface
F_d	Driving force for spreading
θ_e	Equilibrium contact angle
U	Spreading rate
V	Droplet volume

List of Symbols and Acronyms (continued)

n_V	Number of reactive solute moles per unit volume of the reaction product
e	Reaction product layer thickness
C_o	Nominal drop reactive solute concentration
C_e	Concentration of reactive solute in equilibrium with the reaction product
P	Preferred orientation
$I_{(hkl)}$, $I'_{(hkl)}$	Measured and theoretical integrated intensity, respectively
b	Beam broadening inside a thin specimen
Z	Atomic number
E_0	Incident beam energy
t	Sample thickness
C_A, C_B	Weight fractions of elements A and B, respectively
I_A, I_B	Measured characteristic x-ray intensities of elements A and B, respectively
k_{AB}	k-factor for element A in matrix of element B.
I_{oA}, I_{oB}	Initial x-ray intensity of elements A and B, respectively
$(\mu/\rho)^{A}_{Spec}$	Mass absorption coefficient of A
x	Absorption path length
I_A^F / I_A	Ratio of the fluorescence intensity to primary intensity
$\omega_{A(B)}$	fluorescence yield of element A(B)
r_A	absorption edge jump ratio of element A
A_A, A_B	Atomic weights of elements A and B, respectively
I_A	intensity measured for element B
I_A^b	Background intensity under the peak of element A
d	Probe size
w	Width of scan normal to the area scanned
Γ_{min}	Minimum detectability (in atoms/nm^2)

SEM	Scanning electron microscope
SE	Secondary electrons
BSE	Backscattered electrons
TEM	Transmission electron microscope
HRTEM	High resolution transmission electron microscope
STEM	Scanning transmission electron microscope
HAADF	High angular annular dark field
FIB	Focused ion beam
XRD	X-ray diffraction
EDS	Energy dispersion spectroscopy
FEG-SEM	Field emission gun scanning electron microscope
ED	Electron diffraction
CCD	Charged couple device

1. Introduction

The study of metal-ceramic interfaces, in terms of structure and related properties, began somewhere in the early decades of the 20th century. As time went by, more and more applications involving metal-ceramic interfaces have evolved. These include metal-ceramic joining and brazing, interfaces in microelectronics, dental and surgical implants, fuel cells, thin and thick film technologies, functional metallic coatings, metal-ceramic composites, electrical insulators, vacuum feed-throughs and many more.

Since the number of these applications and the need for a reliable by-demand metal-ceramic joint are constantly increasing, so is the need to truly understand and control the metal-ceramic interface and related properties. Technological advancements and improvements over the last three-four decades have enabled observation and analysis of interfaces down to the atomic level, and led to the understanding that superior joint properties will be achieved through interfacial engineering.

Most industrially important oxide ceramics have an ionic nature and are not readily wet by most metals. Alumina (single and polycrystalline) for example, is one of the most used and studied ceramics. This issue has raised the need for ways to generate reliable metal-ceramic joins, which will overcome the poor wetting of oxides.

Two common (and with the largest database) routes for metal-ceramic joining are the metallization technique and direct joining. The metallization technique was first used somewhere in the late 1930's, whereas the direct joining (or reactive joining) technique began somewhere in the 1960's. As opposed to the metallization route, reactive joining is based on a single-step process to join ceramics to metals, but is considered more sensitive to the starting materials and process parameters.

The exact mechanism that allows direct joining is still under debate amongst both academic and industrial researchers. Two rather distinct mechanisms, adsorption and reaction product control, are claimed to be responsible for improved wetting, when an active element (mainly titanium) is added to allow single-step reactive joining.

In order to correlate the governing mechanism and exact metal-ceramic interface structure with mechanical properties of the joint, thermodynamic parameters must be explored. These can include surface and interfacial energies, contact angles, work of

adhesion and more. Some properties are measurable in the solid-liquid (solid ceramic, liquid metal) state whereas others can be analyzed at the solid-solid state only.

This research is aimed at understanding the role that active element play, and the dominant mechanism involved when such an element is added to a braze filler metal with a defined objective, to improve wetting and allow single step joining of metals to ceramics.

Characterization of the metal-ceramic interface was carried out using scanning electron microscopy (SEM), X-ray diffraction (XRD), energy dispersive spectroscopy (EDS), selected area electron diffraction (SAED), and atomic scale observations using transmission electron microscopy (TEM), with specimens prepared by dual-beam focused ion beam (dual-beam FIB).

The system chosen for analysis is based on sapphire, the single crystalline form of aluminum oxide as the ceramic substrate, gold as the base metal and titanium as the active element. The main experimental procedure used is dewetting in a controlled atmosphere.

2. Literature Survey

2.1 Surface Energy of Solids

The term *'interface'* is a general expression used to describe a boundary between phases, and/or the region that separates them. Phases can be solid, liquid or vapor and common interfaces are metal-ceramic, metal-metal, grain boundaries, etc. The interface plays the role of a mediator between phase properties and its structure and characteristics can influence bulk material properties.

In order for an interface to exist, it must have some amount of energy, implying that work has to be done (gained or spent) in order to create it. The reversible work *dW*, needed for a change in interfacial area *dA*, at constant temperature, volume and chemical potential is the surface energy, γ :

$$\gamma = \left(\frac{dW}{dA} \right)_{T,V,m} \quad \left[J/m^2 \right] \tag{1}$$

Liquids (and amorphous phases) have a limited degree of order, and atoms or molecules are relatively free to move, hence the surface energy of liquids is not related to any orientation or direction. Thus, for liquids the surface energy is isotropic (equal in all directions). Upon reaching equilibrium (assuming no gravitational or other external forces applied), liquids will have the shape of a sphere. This way the minimum energy requirement is achieved for the smallest surface area possible, according to eq.(1).

On the other hand, solid surfaces exhibit different surface energies for differently oriented surfaces, implying *anisotropy*. For solids, equilibrium shapes will differ from a sphere. The final form will depend on crystallographic parameters, the number of surface bonds, atom mobility, the presence of impurities, and the degree of atomic surface rearrangement. Some typical surface energy values are 0.06 J/m^2 for liquid Cs [1], 1.9 J/m^2 for liquid Ni [2], 1.94 J/m^2 for solid Ti [3], 1.279±0.078 J/m^2 for Al_2O_3 [4] and 1.19 J/m^2 for solid TiC [1]. Surface energy values can also be correlated with material properties such as the melting point [5] and heat of sublimation and/or evaporation [6] (surface energy increases with an increase in both). The surface energy of liquid metals decreases linearly with temperature. Values for solid metals are

typically ~20% higher than that of the liquid at T_m and also decrease with temperature [1].

The anisotropic nature of surface energy of solids was thoroughly investigated, in order to extract energy terms for different metal and ceramics for different crystallographic orientations. McLean and Mykura [7] showed that FCC iron exhibits an energy minimum for three different surface family planes: {110}, {110} and {111}. Planes belonging to these families will be preferred as surface planes, and in this case the equilibrium shape of FCC iron will again differ from a sphere. Other evidence of the anisotropic nature of the surface energy in solids was also given by Mykura [8] for nickel, who found lower energy orientations similar to those of FCC iron. Wynblatt and Chatain [9] have demonstrated the effect of alloying on minimum energy configurations, as can be seen in the γ-plot, which is a plot of surface energy vs. angle of orientation (Figure 1).

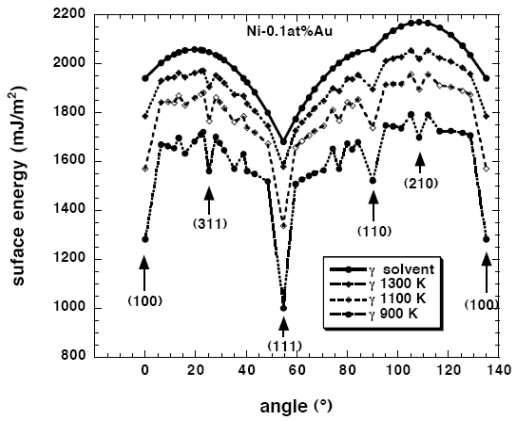

Figure 1: Surface energy variation with orientation around the edge of the stereographic triangle. Curves are shown for the pure solvent (Ni), and for a Ni-0.1at%Au alloy at three temperatures [9].

In Figure 1, the anisotropy of surface energy for pure nickel and nickel alloyed with 0.1 at. % Au can be seen. The segregation of gold to the alloy's surface and grain boundaries increases the anisotropy of the alloy from that of pure nickel, which is typical for FCC metals, exhibiting {100}, {110} and {111} low-index planes as the ones with minimum surface energies. Alloying with gold promotes two more energy minimums seen as cusps in the plot, which are not common for FCC metals [7-8], at (311) and (210). In addition, the lowest energy orientation is (111).

When dealing with metal and metal alloys, one can predict that impurity segregation to surfaces and grain boundaries is bound to change the surface energy of

the base metal, according to the *Gibbs adsorption isotherm*. The change in surface energy caused by a change in impurity concentration, for a dilute binary system [6], can be written as:

$$\Gamma = -\frac{1}{R \cdot T} \cdot \frac{d\gamma}{d \ln C_i} \tag{2}$$

where $d\gamma$ is the unit change in surface energy caused by a unit change in impurity concentration C_i, R is the universal gas constant, T is the absolute temperature and Γ is the excess surface concentration per unit area (that can be defined as the number of molecules of the i^{th} species per unit area of the surface). The Ni-0.1at.% Au system mentioned above is a good example of this.

Impurity and dopant segregation usually take place to the higher energy surface planes, in this way achieving a reduction in the surface energy and in the surface energy anisotropy. Nevertheless, some experimental evidence exists for the opposite phenomena, as in the case of Bi-saturated copper studied by Chatain et al. [10]. In this system dramatic changes occurred upon saturation of copper with bismuth (compared to pure copper). In the case of pure copper, all possible surface orientations are stable, but after saturating with bismuth, only {111}, {100}, {110} and {320} orientations remain stable. The weak surface energy anisotropy of pure copper is increased four times after bismuth saturation.

Surface energy anisotropy exists for oxides as well, as evidenced by the work of Ramamoorthy et al. [11], who examined the energy of different TiO_2 surfaces (see Figure 2).

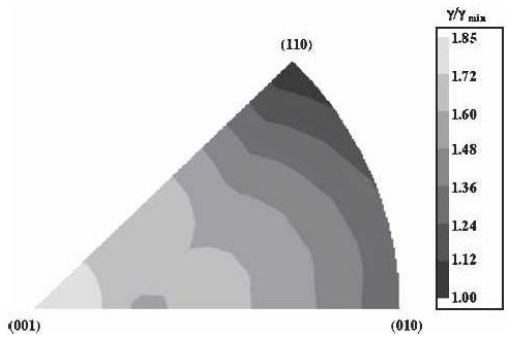

Figure 2: Anisotropy of surface energy of TiO_2 (rutile), computed based on first principles calculations [11].

It can be seen from the stereographic triangle that the (001) surface has the highest energy while (110) has the lowest surface energy. The anisotropy of the surface energy is clearly seen.

Surface energy also tends to change with temperature. Nikolopoulos [12] established a linear correlation of surface and grain boundary energy with temperature for polycrystalline Al_2O_3. Using measurements of contact angles and the multiphase equilibrium method at the temperature range of 1473-1923K, the correlation was found to be:

$$\text{Surface energy: } \gamma_{Al_2O_3} = 2.559 - 0.784 \cdot 10^{-3} \cdot T \quad \left[J/m^2\right] \tag{3}$$

$$\text{Grain boundary energy: } \gamma_{Al_2O_3 - Al_2O_3} = 1.913 - 0.611 \cdot 10^{-3} \cdot T \quad \left[J/m^2\right] \tag{4}$$

Rearrangement and movement of surface atoms caused by thermal treatments and in some cases by impurity surface segregation can induce a change in the surface energy. For example, the Al-terminated sapphire surface was shown to have a lower surface energy compared to an O-terminated surface [13].

At high temperatures and under vacuum, surface planes can move inward, towards the underlying planes, or upward and surface atoms can slightly move and change their positions (clearly, surface atoms are less limited than bulk atoms) in what is known as *surface relaxation and reconstruction processes*, respectively. These movements are usually smaller than bulk d-spacing, but are large enough to change the surface electronic and atomic structure, and often leave the surface unit cells with dimensions that differ from those of the bulk unit cells, thus lowering the surface energy. During such processes, the covalent nature of bonds can change, as found for example, by Gautier et al. [14] for Al-O bonds in the reconstructed α-Al_2O_3 surface, where it was shown that $\left(\sqrt{31}\times\sqrt{31}\right)\boldsymbol{R}\pm 9^0$ reconstructed surface is more covalent than the (1X1) surface. There are certain cases in which surfaces that exhibit dangling bonds are unstable. These surfaces can reconstruct by coalescing the dangling bonds, thus stabilizing the surface and reducing its energy [15]. Changes induced at the surface due to relaxation processes can cause a reduction of surface energy, as found by Manassidis et al. [16] for (0001) α-Al_2O_3 surface, where a reduction of more than 50% was

calculated for a relaxed (0001) surface (3.98 J/m^2 and 1.76 J/m^2 for the unrelaxed and relaxed surfaces, respectively).

2.2 ECS - Equilibrium Crystal Shape

Atoms located at the surface usually have a higher energy than the same atoms in the bulk, due to the fact that a surface atom does not experience the same force and electronic balance and the same attractive and repulsive forces a bulk atom experiences. Since the higher energy states are not favorable, surface atoms will seek to minimize their surface energy.

Solids usually exhibit surface energy anisotropy. When a solid particle is allowed to equilibrate on a substrate (below T_m of both) its final shape must reflect the anisotropy in surface energy as well as the influence of the substrate. As in the case of FCC iron [7] mentioned in the previous section, planes belonging to {100}, {110} and {111} families will have the lowest surface energies and will be preferred as surface planes. The geometrical meaning of a minimum energy state is that an equilibrated particle will exhibit a minimum ratio of surface energy to volume, thus presenting its lowest energy planes as surface planes. The shape of a particle fulfilling this condition will be a faceted polyhedron known as the *ECS - **E**quilibrium **C**rystal **S**hape* of the particle. The facets appear at lower temperatures (lower than T_m), as the crystal is cooled. The first temperature at which a facet appears at the surface is known as the *roughening temperature*. Two examples of ECS shapes for gold and lead, by Sadan & Kaplan [17] and Heyraud & Metois [18], respectively, are presented in Figure 3 and Figure 4.

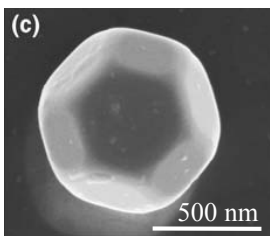

Figure 3: Secondary electron SEM image of a gold particle equilibrated on c(0001) sapphire for 100 hr in air, exhibiting (111) facet at the top [17].

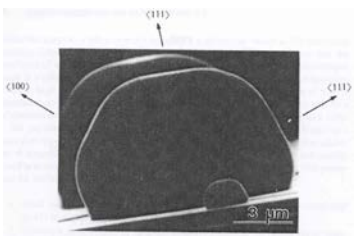

Figure 4: SEM image of an equilibrated lead crystal at 200°C [18], displaying (111) and (100) type facets at the surface.

The equilibrated particles seen in Figure 3 and Figure 4 show surface faceting. Facets at the surface are actually lower energy planes such as {111} and {100}.

Equilibrium shapes are also known for ceramics, where pores equilibrated through annealing are usually examined. These pores exhibit a faceted structure, as can be seen for an etched pore in sapphire, annealed for 24 hr at 1900°C [19] (Figure 5).

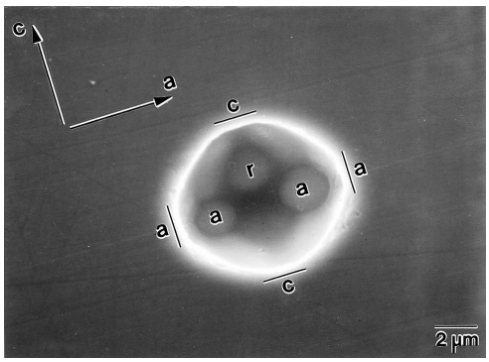

Figure 5: High magnification SEM micrograph of an individual pore exposed by polishing after 24 hr anneal at 1900°C of a sapphire substrate. Pore showing that c-, r-, and a-type plane facets formed during annealing [19].

One useful way of examining the ECS of a solid particle equilibrated on a solid surface was formulated in the work of Wulff [20], known as the *Wulff Plot* and *Wulff Construction*.

Starting with the Wulff plot, the surface energy of a solid particle, γ_{SV}, is plotted as a function of the surface orientation. The radius vector, $r_{(hkl)}$, represents the orientation of the surface, meaning it represents the normal to the surface, and the magnitude of $r_{\{hkl\}}$ is the magnitude of the surface energy in that direction; $\gamma_{SV} \cdot \boldsymbol{n}_{\{hkl\}}$. It follows that $\boldsymbol{r} = \gamma_{SV} \cdot \boldsymbol{n}_{\{hkl\}} \cdot (\boldsymbol{n}_{\{hkl\}})$. The treatment for the particle is two-dimensional, but it applies to three dimensions also. A two dimensional Wulff plot of an FCC crystal oriented along $<1\bar{1}0>$ direction [21] is shown in Figure 6.

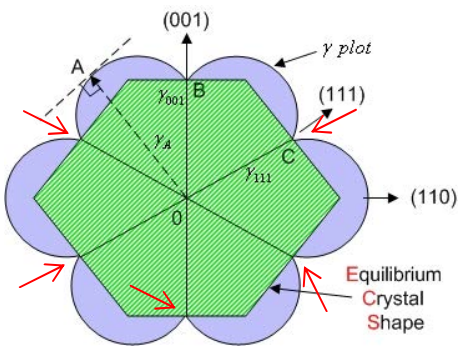

Figure 6: Two dimensional section of the Wulff plot for an FCC crystal oriented along $<1\bar{1}0>$ direction [21].

The procedure that derives a particle's ECS from the Wulff construction is [22]:

a. Draw a radius vector from the origin, 'O' (termed the *Wulff Point*), so the vectors intersect the Wulff plot (as in Figure 6).
b. Draw lines normal to the radius vectors drawn in (a).
c. The ECS of the particle is the shape that is enclosed by these lines (the green crossed shape in Figure 6).

In the Wulff plot, only one quarter is needed to describe the entire ECS, since it has the same symmetry of the crystal. Cusps can be seen on the plot as minima (red arrows). If we observe a system made up of one component that has two phases, α and β, separated by some interface, the construction of the Wulff plot is explained as follows: we assume the α phase to be solid and the β phase to be vapor, liquid or solid. By assuming that both phases posses some sort of an equilibrium shape (without volume changes), the shape of the interface can be determined. The free energy minimization condition is then given by the demand that $\int \gamma(n)\,dA$ will be minimal. The integral is taken over the entire interface (or surfaces) with a normal vector n. For liquids, where γ is independent of orientation, the condition for equilibrium gives the interface (or free surface) the shape of a sphere (which has the minimal surface area), whereas for solids who exhibit surface energy anisotropy, the equilibrium shape will be some polyhedron. In the polyhedron, low energy planes (facets) will be exposed or 'pushed' to the surface. When cusps appear in the Wulff plot, a polyhedron-type shape appears in the ECS, and the larger facets represents planes with lower energies. The larger the anisotropy in the particle's surface energy, the greater is the number of facets that will appear in the polyhedron. By examining the shape achieved from the Wulff construction, ratios of surface energies to radius vectors can be compared:

$$\frac{\gamma_1}{\boldsymbol{R}.\boldsymbol{V}_1}=\frac{\gamma_2}{\boldsymbol{R}.\boldsymbol{V}_2}=\boldsymbol{const}. \tag{5}$$

Using this equality, if one of the surface energies is known, all other surface energies of the particle (relating to each facet in the ECS) can also be determined.

The γ-plot achieved from the Wulff construction can also be used to extract information about *surface torque* through the slope, $(\partial\gamma/\partial\theta)$. The torque of a surface (or boundary) can be regarded as the rate of change of its energy with orientation (or

inclination). One of the first to address torque terms together with energies was Herring [23], through:

$$\sum_{i=1}^{n} \gamma_i \cdot \boldsymbol{t}_i + \left(\frac{\partial \gamma}{\partial \alpha} \right)_i \cdot \boldsymbol{n}_i = 0 \qquad (6)$$

where γ_i is the energy of the i^{th} boundary (or surface); t_i is a unit vector in the plane of the i^{th} interface, normal to the line of intersection of the interfaces; I is a unit vector along the line of intersection and $n_i = I \times t_i$ and α_i is the angle at which the ith boundary rotates about I [24]. When considering interfacial (or surface) energies alone and torque terms are neglected, equation (6) reduces to the sine law.

The torque term will be constant in the case of isotropy in surface energy, since the slope of the γ-plot is a straight line (and therefore $(\partial\gamma/\partial\theta)$ is constant). When surface energy is anisotropic, the torque term will have its largest values in the cusps (minimum energy points), where the change in surface energy γ due to a change in orientation θ is the largest.

The Wulff construction is widely used in the analysis of equilibrium shapes of different crystals (both pure and doped). An example of an ECS comprised of many facets can be seen in the work of Chatain et al. [25] who examined the equilibrium shape of copper (see Figure 7).

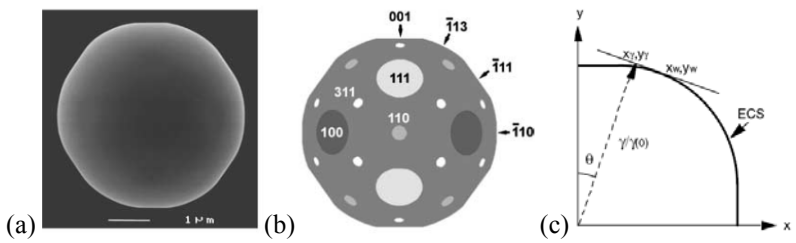

Figure 7: Equilibrium crystal shape of copper grown on sapphire: (a) photomicrograph viewed along a <110> direction, (b) schematic ECS produced using Wulffman freeware and (c) one quarter of the ECS from the Wulff construction (right) [25].

Hansen et al. [26] also examined ECS of palladium nano-crystals on Al_2O_3 using the Wulff construction and obtained a value of 2.8±0.2 [J/m^2] for the work of adhesion of Pd (see Figure 8).

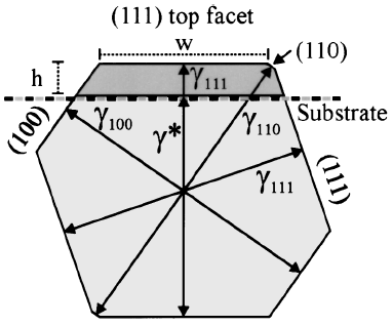

Figure 8: Cross section of a Pd cluster based on the Wulff construction using theoretical surface energies for the three low index Pd surfaces. (110) facet develops only for clusters with $w \geq 80\,\overset{0}{A}$ [26].

The formation of an ECS is enabled through diffusion processes, where atoms shift and move to different surfaces and interfaces. Certain factors can influence the time needed for a solid particle with a given dimension to achieve equilibrium. Nichols and Mullins [27] were able to put all these factors into one equation allowing the calculation of time needed for a solid particle with a radius *r* to achieve equilibrium:

$$t = \frac{r^4}{24 \cdot B} \quad [\text{sec}] \tag{7}$$

B is defined as:

$$B = D_S \cdot \gamma \cdot \nu \cdot \Omega^2 / kT \tag{8}$$

where *r* is the particle's radius, *k* is Boltzmann's constant; *T* is the absolute temperature; γ is the surface energy; D_S is the surface diffusivity; *v* is the number of atoms per unit of surface area of the particle and Ω is the atomic volume (for FCC copper for example, Ω is $a^3/4$, where *a* is the lattice parameter of copper [25].

As evidenced by equations (7) and (8), the most influencing parameter on time needed for equilibration, besides the size of the particles (expressed by r), is the temperature, expressed both by T directly and through the diffusion parameter D_S (exponential dependence upon T). The immediate experimental meaning of this is that relatively high temperatures must be used in order to achieve equilibration in reasonable times. Besides temperature, the strong dependence upon particle size has an experimental constraint, where the smallest possible particles have to be chosen for microscopic observation.

The Wulff shape enables one to know what is the ECS of the examined particle, which is comprised of lower energy facets (in most cases), or from stable facets. At high temperatures, unstable surface planes other than those predicted by the Wulff shape can 'break-up' into a number of more stable and lower energy planes. Although this seems in contrast to the demand for minimum surface area (as more facets are created), the condition for minimum surface energy is fulfilled, and the total surface energy of the particle is reduced [28].

2.3 Thermodynamic Parameters at Metal-Ceramic Interfaces

Metal-ceramic interfaces are highly abundant in today's industry and have been so since the middle of the 20th century. Such interfaces can be found in the automotive and aerospace industry, in brazing, microelectronics, vacuum systems, fuel cells, high voltage applications and more. Metal-alumina interfaces are of special interest due to their role in microelectronic packaging, metal-ceramic composites, catalytic applications, gas sensors and much more [29, 30, 31].

The vast majority of the applications mentioned above demand a reliable, high strength and in most cases vacuum tight metal-ceramic joint or interface. In order to design and engineer such joints and interfaces, their complete thermodynamic description must be known. This includes different surface and interface energies, work of adhesion, contact angles and more.

2.3.1 Contact Angles and Thermodynamic Work of Adhesion

Since most processes start with the melting of some metal upon a ceramic substrate in order to form a joint or interface, it is important to start with this description. The shape of a liquid droplet on top of a flat solid substrate can provide significant information from its contact angle, and the most common and easy way to extract such information is by the *sessile drop* experiment (see Figure 9). In the sessile drop configuration, a metal is placed upon a flat solid substrate and the entire system is heated in a pre-selected atmosphere to its melting point, where the liquid metal is allowed to equilibrate on the substrate. At this point, the capillary forces drive the homogeneous liquid to spread and form a shape with a constant curvature. The contact angle is driven towards the macroscopic equilibrium value derived from *Young's equation*.

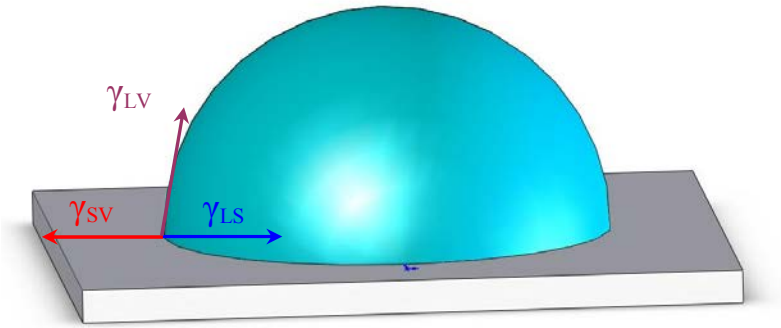

Figure 9: Schematic illustration of a liquid metal droplet equilibrated on a flat solid substrate. Different surface and interface energies and contact angle are marked.

The mathematical relation that is evidenced from the triple point area (junction of three phases, liquid, solid and vapor) is actually an energy balance, given by *Young's equation* [32]:

$$\gamma_{SV} = \gamma_{SL} + \gamma_{LV} \cdot \cos\theta \tag{9}$$

where γ_{SV}, γ_{SL} and γ_{LV} are the solid-vapor, solid-liquid and liquid-vapor interfacial energies, respectively and θ is the contact angle of the liquid on the substrate. The energy balance is taken for the horizontal components alone and ignores the perpendicular portion of $\gamma_{LV} \cdot \sin\theta$ as well as possible torque terms. Rearrangement of equation (9) yields:

$$\left|\cos\theta\right| = \left|\frac{\gamma_{SV} - \gamma_{SL}}{\gamma_{LV}}\right| \leq 1 \tag{10}$$

From equations (9) and (10) it can be seen that complete wetting of the liquid on the solid substrate will occur when θ reaches 0°. Wetting is divided into three ranges, complete wetting ($\theta=0^{\circ}$), partial wetting ($0^{\circ}<\theta<180^{\circ}$) and non-wetting ($\theta=180^{\circ}$).

The driving force for the creation of a new metal-ceramic interface is the decrease in the free energy that accompanies the creation of a new contact area between the metal and the ceramic substrate. The *thermodynamic work of adhesion* is the work gained (or spent) from the creation of that interface and is given by the *Dupré* equation [33]:

$$W_{ad} = \gamma_{LV} + \gamma_{SV} - \gamma_{LS} \qquad \left[J/m^2\right] \tag{11}$$

Combining equations (9) and (11) yields:

$$W_{ad} = \gamma_{LV} \cdot (1 + \cos\theta) \tag{12}$$

Different solid-liquid and liquid-liquid interactions in different systems will yield different values of contact angle and work of adhesion. Good wetting (low contact angles) is usually obtained in systems that exhibit strong liquid-solid interactions, but also in systems exhibiting weak liquid-solid and liquid-liquid interactions [34]. Liquid copper, for example, exhibits a contact angle of 128° on Al_2O_3 (1423K in high vacuum) [34]. This system has strong liquid-liquid and weak solid-liquid interactions and poor wetting is observed. In contrast, liquid copper on tungsten exhibits a contact angle of 10° (1373K in vacuum or H_2 atmosphere) [34]. This system has strong liquid-liquid and solid-liquid interactions and good (yet not complete) wetting is observed.

As evidenced from equation (11), high values of W_{ad} will be achieved with high surface energies of the liquid metal and solid substrate and low solid-liquid interface energy.

When fracture occurs at the metal-ceramic interface, the metal and the ceramic usually absorb a considerable amount of the fracture energy and the equality in equation (11) becomes an inequality with the $W_{fracture}$ side higher. A large number of metal-ceramic systems exhibit such a relation, as can be seen in Figure 10 from the work of Hondros et al. [6].

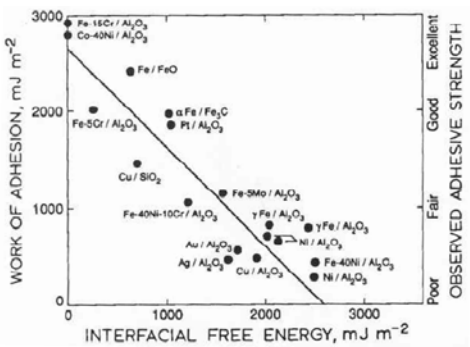

Figure 10: Work of adhesion and observed adhesive strength vs. interfacial free energy [6].

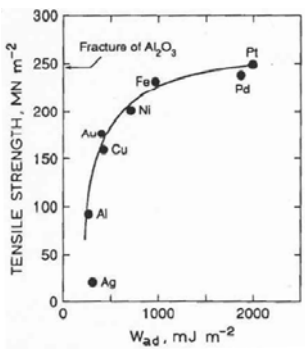

Figure 11: Tensile strength as a function of W_{ad} for common FCC metal/sapphire (0001) interfaces [35].

For common metals on sapphire, a correlation exists between W_{ad} and the tensile strength. As W_{ad} increases so does the tensile strength since γ_{SL} decreases, as evidenced by the work of Klomp [35] in Figure 11, describing room temperature tensile strength of solid state bonded FCC metals/sapphire (0001) interfaces, as a function of W_{ad} at $0.9T_m$.

The Young equation is only valid when the solid is perfectly rigid and insoluble and the liquid drop can advance or recede only in a direction parallel to the substrate's surface. In most metal-ceramic systems, high temperatures are used and experimental temperatures can be very close to T_m of the metal (and sometimes higher). At these temperatures, local diffusion and transport at the metal-ceramic interface are enhanced, leading to partial dissolution of the substrate and sometimes to solution-precipitation. This can cause shape changes of the solid at the triple point and in order to achieve equilibrium, the triple line has to move horizontally and vertically [36,37]. In such cases, Young's equation is not valid and the dihedral angles that form at the triple junction can be measured (see Figure 12).

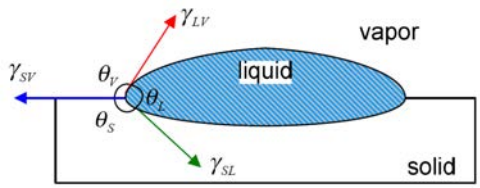

Figure 12: Schematic illustration of dihedral angles formed at the triple junction upon substrate dissolution.

The relation between dihedral angles and the surface energies is given by the sine law:

$$\frac{\sin \mathrm{f}_S}{\mathrm{g}_{LV}} = \frac{\sin \mathrm{f}_L}{\mathrm{g}_{SV}} = \frac{\sin \mathrm{f}_V}{\mathrm{g}_{SL}} \qquad (13)$$

where $\mathrm{f}_S, \mathrm{f}_L$ and f_V are the equilibrium dihedral angles in the solid, liquid and vapor, respectively. Using equation (13), and if one of the surface energies is known, the remaining surface energies can be extracted upon measuring the dihedral angles. Two of the many experimental evidences of the dissolution of the substrate at high temperatures are given in the work of Saiz et al. [38] and Levi and Kaplan [4] (see Figure 13).

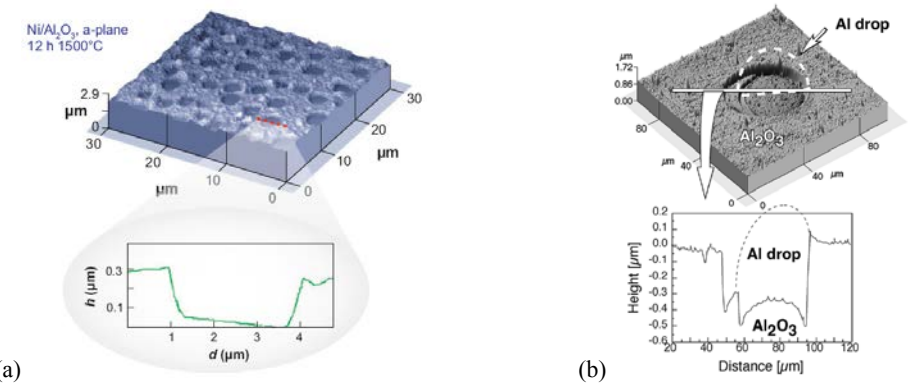

Figure 13: Experimental evidence of the dissolution of the substrate under the molten metal drop at high temperatures: (a) sapphire surface after the removal of small Ni drops after 12 hr at 1500 °C [38]. (b) Sapphire surface after the removal of Al drop after 2 hr at 900 °C [4].

In cases where the drop radius is large compared to a possible ridge that can form on the substrate surface at the triple junction, the macroscopic contact angle, θ, will tend to match the one given by Young's equation, and for longer times or when the drops are smaller, full two dimensional equilibrium can be attained [38].

2.3.2 Extraction of Thermodynamic Parameters - Experimental Procedures

Thermodynamic parameters such as contact angles (macroscopic Young's contact angle and dihedral angles), surface and interface energies and thermodynamic work of adhesion can be determined experimentally. Experimental procedures used to extract these parameters can be carried out in the solid state or in the mixed solid-liquid state, where the substrate (ceramic) is solid and the metal is in liquid state. The two most common methods are the *sessile drop* and the *dewetting* experiments.

2.3.2.1 Sessile Drop Experiments

In sessile drop experiments, a metal is melted upon a flat and rigid substrate and allowed to equilibrate in the liquid state. At this stage, depicted in Figure 9, the equilibrium shape of the drop is determined mainly by the surface energy balance, where in some cases (mostly with larger millimeter size drops), gravitational effects have to be taken into consideration. The energy balance, as given in equation (9), is used to calculate surface energies of the solid substrate or the liquid metal or the

interfacial solid-liquid energy. The contact angle, as given by Young's equation, is the macroscopic contact angle which can serve as an indicator to the degree of wetting of the liquid metal.

Sessile drop experiments are rather easy to perform but suffer from large inaccuracies. These stem from various reasons:

a. The parameters chosen for each experiment, temperature, soaking time and atmosphere change the thermodynamic state. Different temperatures change the viscosity of the liquid metal and thus it's degree of spreading on the substrate. A known example of temperature influence on contact angle is the Al-SiC system [39]. In this system, above a certain temperature there is a significant decrease in the liquid contact angle from 155° to 45° between 900°C and 1000°C, respectively. This decrease is attributed to the decomposition and breakdown of a passive oxide thin film at the ceramic-metal interface. The contact angle oscillates between these values. Metals that have a strong affinity to oxygen are not suitable for sessile drop experiments carried out in relative high $P(O_2)$ atmospheres. Oxygen in the furnace (even in a vacuum atmosphere) can adsorb at the liquid surface and even react with the liquid metal. Two opposite examples can be found in contact angles measured for Au-Al_2O_3 and Sn-Al_2O_3 systems. Gold has a low affinity to oxygen, and small range of measured contact angles from 131±2° in vacuum or in He, He-O_2 atmosphere [40] to 140±3° in vacuum or in Ar, Ar-H_2 atmospheres [41]. Tin on the other hand, that has a higher affinity for oxygen, has contact angles in the range of 108-174° [42]. Obviously atmosphere has an influence and before conducting such an experiment the atmosphere composition has to be known and tightly controlled.
b. Substrate roughness plays an important role in the spreading of liquid metals. Rough surfaces can inhibit drop spreading by simply sinking the liquid metal in the 'hill and valley' surface topography instead of allowing it to spread and achieve equilibrium. Eustathopoulos et al. [34] states that an average roughness much less than 100 nm is needed for a contact angle measurement accuracy of few degrees. Surface roughness is rarely treated or measured in reports on contact angle measurements. The use of single crystalline substrate (nanometer scale surface roughness) can ease some of these problems as their polishing displays better results and no grain boundary grooving takes place at high temperatures.

c. Contact angle hysteresis can also influence the accuracy of measurement and can result in a 5-20 degrees difference [34]. Hysteresis is caused by the fact that the triple junction advances and/or recedes. Advancing contact angles are usually higher then receding ones, $\theta_{adv.} > \theta_{rec.}$ (see Figure 14).

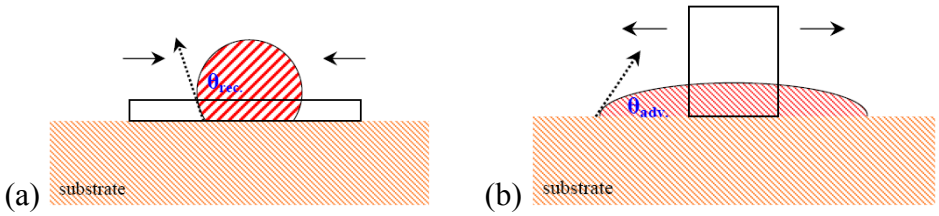

Figure 14: Schematic illustration of (a) receding contact angle and (b) advancing contact angle.

d. In order to calculate the solid-liquid interface energy from sessile drop experiment, the values of γ_{SV} and γ_{LV} must be known (according to equation (9)) for the experimental conditions used in the specific sessile drop experiment.
e. The presence of impurities in the atmosphere or in the liquid metal can result in segregation to different interfaces, which will inevitably change the contact angle and energies.

Sessile drop experiments can be conducted with accuracies hardly better than $\sim\pm5^{\circ}$ (as for the non reactive close to ideal Au/Al_2O_3 system [34]) and demand atmosphere control, small surface roughness values, and knowledge of impurity levels. Nevertheless, it is a rather easy established experiment that can indicate general trends in the behavior of liquid metals on solid substrates.

2.3.2.2 Dewetting Experiments

As mentioned above, while sessile drop experiments are usually carried out in the liquid state, *dewetting experiments* can be conducted in both the solid and liquid state. In sessile drop experiments, rather large volume/mass droplets are needed in order to increase the accuracy of the measurement of contact angles and the calculation of surface energies. As an example, Eustathopoulos et al. [43] used the formulation of Sangiorgi et al. [44] to estimate the droplet mass for a hypothetic metal with density of 8 gr/cm^3, γ_{LV} of 1300 mJ/m^2 and θ of 120°. For drop dimensions measured with an

accuracy better than 0.1% and surface energy calculated with an accuracy of about ±2%, a 3 gr drop mass is needed. This is a rather large mass needed to obtain high accuracies.

Dewetting experiments, on the other hand, utilizes much smaller particles. During conventional metal-ceramic dewetting procedures, a thin film is deposited on the ceramic substrate, using regular sputtering, thermal evaporations and the like. The coated substrate is then heated to a temperature in which the film is liquefied, and then cooled to a lower temperature (usually ~0.9-0.95T_m) where it is held for a pre-chosen amount of time to allow equilibration of the solid particles. Alternatively, dewetting can be conducted entirely in the solid state. During the thermal cycle, the solid film is disrupted and breaks up at temperatures close to its melting point. The disruption of the solid film is due to the drive to minimize surface energies. The dewetting experiment results in the creation of a large number of solid particles, isolated on the solid substrate. An example of the dewetting process carried out in the Au-graphite system annealed under UHV at 1000°C can be seen in Figure 15, from the work of Heyraud and Metois [45].

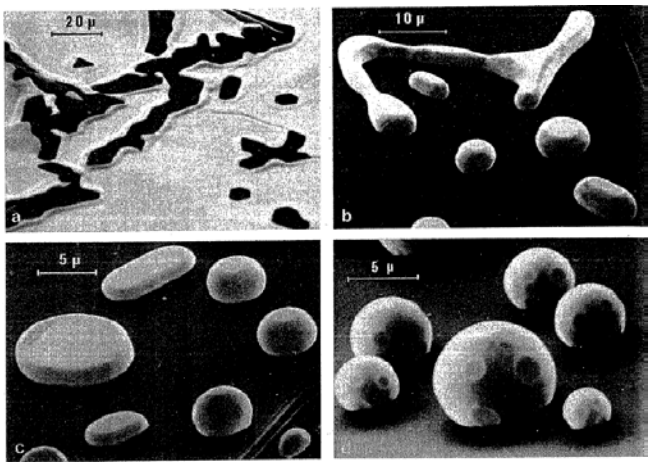

Figure 15: Evolution of a 3000 $\overset{0}{A}$ thick gold film on a graphite substrate annealed under UHV at 1000°C for: (a) 15 min, (b) 10 hr, (c) 50 hr, (d) 70 hr, images taken from [45].

As it equilibrates, a particle will eventually evolve into its ECS, as mentioned in section (2.2 ECS - Equilibrium Crystal Shape). Since the shape evolution is taking place in the solid state and dictated by diffusion processes, it requires longer times compared to liquid droplet shape evolution under viscous flow. Normal experimental durations require the examination of smaller particles when the dewetting process is used, usually

1-10 μm in diameter. The time needed for equilibration of particles with a given diameter can be estimated using equation (7) given by Nichols and Mullins [27]. The final shape will be determined by the extent of surface energy anisotropy of the particle. Heyraud and Metois [45] observed an isotropy of 3.4% in the surface energy of gold crystallites equilibrated on a graphite substrate. The ECS of gold was found to be comprised of facets belonging to the {111} and {100} plane families.

As opposed to sessile drop experiments, where the drop coordinates (radius and height) and contact angle are measured in-situ, dewetting requires ex-situ analysis. Most of the particles created are small in diameter, and therefore demand electron microscopy for observation. Due to that, dewetted samples are observed only after the process has ended, after cooling (although in-situ dewetting can be carried out using a hot stage inside an electron microscope, but temperatures are limited and there are many technical and experimental difficulties). Since facets appear at the particle's surface, measuring the solid contact angle of the particle on the substrate has no meaning. As for sessile drop experiments, the dewetting atmosphere has to be tightly controlled also, since residual gasses and impurity adsorption on the particle and substrate surfaces can influence and change the ECS and by that, the thermodynamic parameters.

Despite these drawbacks of the dewetting process, important information can be extracted from the equilibrated solid particle. First, the extent of surface energy anisotropy can be seen, according to the shape of the ECS [25,45]. Second, substrate effects can be examined through the usage of different substrates and differently oriented substrates [17,46]. Third, preferred orientation of the solid particles on the substrate can be determined using X-ray diffraction of the entire dewetted sample. Fourth, through additional analysis of a cross sectioned particle, surface and interface energies can be determined, using *Winterbottom analysis*.

2.3.2.3 Winterbottom Analysis

Solid and equilibrated particles obtained by the dewetting procedure can be further processed and examined using electron microscopy in order to extract surface energy data.

Winterbottom [47] in his work from 1967 assumed that the shape of an equilibrated particle that lies on a solid substrate has to reflect the substrate's effect as

well as the anisotropy in its surface energy. However, the major difficulty in treating a solid particle, as opposed to treating a liquid droplet, is the anisotropy in the surface energy. One can define the surface energy as the variation in the Helmholtz free energy of a system that is added a unit area of a new surface, at constant T, V and moles of each component:

$$\gamma \equiv \left(\partial F / \partial A\right)_{T,V,n_i} \tag{14}$$

The contact angle cannot serve as a unique character of the particle when γ is anisotropic. From this point, Winterbottom assumed that: a) Vapor, particle and substrate surfaces are all saturated with respect to the species present in the system; b) Particle-substrate interactions are short-ranged and are on the order of several lattice parameters; c) A thermodynamic reservoir envelopes the system and the relevant chemical potentials are maintained; d) The particle is large enough so that edge and corner energies can be neglected and surface tensions are independent of particle size.

Under these assumptions, the variation in the free energy of the system, $\delta\psi$, caused by the shape change is:

$$\delta\psi = \delta \int_{SV} \gamma_{SV} dA + \delta \int_{SP} \gamma_{SP} dA + \delta \int_{PV} \gamma_{PV} dA \tag{15}$$

where *S*, *V* and *P* denote the substrate, vapor phase and single crystal particle, respectively, *A* is the area. At stable equilibrium, $\delta\psi = 0$, and the general condition for a stable shape is:

$$0 = \delta \int_{SV} \gamma_{SV} dA + \delta \int_{SP} \gamma_{SP} dA + \delta \int_{PV} \gamma_{PV} dA \tag{16}$$

In order to solve equation (15), all of the surface energies are needed. However, a simplification is at hand, and by using the fact that the sum of surfaces A_{SP} and A_{PV} equals A_{SV} without the particle on top (assuming substrate and substrate-particle interface are co-planar) and that the first term of equations (15) and (16) does not change with particle shape, equation (16) can be rewritten as:

$$\delta \int_{SV} \gamma_{SV} dA = \delta \int_{S} \gamma_{SV} dA - \gamma_{SV} \delta A_{SP} \tag{17}$$

The substrate *S* is not affected by the shape changes of the system, meaning that $\delta \int_{S} \gamma_{SV} dA$ in equation (17) equals zero. Combining equations (16) and (17) yields:

$$\delta \int_{SP} \gamma_{SP} dA + \delta \int_{PV} \gamma_{PV} dA - \gamma_{SV} \delta A_{SP} = 0 \tag{18}$$

With other rearrangements and with reverting back to the integral form of $\gamma_{SV} \delta A_{SP}$ (that is $\delta \int_{SP} \gamma_{SV} dA$), equation (18) becomes:

$$\delta \int_{SP} \gamma_{SP} dA + \delta \int_{PV} \gamma_{PV} dA - \delta \int_{SP} \gamma_{SV} dA = 0 \quad \Rightarrow \quad \delta \int_{SP} (\gamma_{SP} - \gamma_{SV}) dA + \delta \int_{PV} \gamma_{PV} dA = 0 \tag{19}$$

Since the integrals have to be evaluated over the entire surface of the particle *P*, Winterbottom defined a general surface tension, γ^*, for the particle. This general surface tension is defined as $\gamma^* = \gamma_{PV}$ for all orientations corresponding to the particle-vapor surface and as $\gamma^* = (\gamma_{SP} - \gamma_{SV})$ for the particle interface in touch with the substrate. By using γ^*, equation (19) can be rewritten as:

$$0 = \delta \int_{SP} (\gamma_{SP} - \gamma_{SV}) dA + \delta \int_{PV} \gamma_{PV} dA = \delta \int_{P} \gamma^* dA \tag{20}$$

Now, in order to determine the equilibrium shape of a particle that lies on top of a solid substrate, the equilibrium shape of an equivalent particle that has a surface energy of γ^* has to be determined. This way the problem is reduced. The equilibrium shape of the particles with surface energy γ^* would be achieved when this energy will be minimal, as in the Wulff construction [20] ($\int \gamma(\boldsymbol{n}) dA$=minimum). Equation (20), with the constraint that V(P)=const' was actually solved by Wulff. According to Wulff [20], the equilibrium shape of the particle would be such that $\gamma^*_{(hkl)} = \lambda \cdot \boldsymbol{h}_{(hkl)}$. Meaning

that the distance $h_{(hkl)}$ of the surface with orientation (hkl) from the center of the equilibrium shape (known as the Wulff point) is directly proportional to the surface tension, $\gamma_{(hkl)}$ (by the factor λ). Two possible particle-substrate configurations may exist when wetting is partial, as shown in Figure 16.

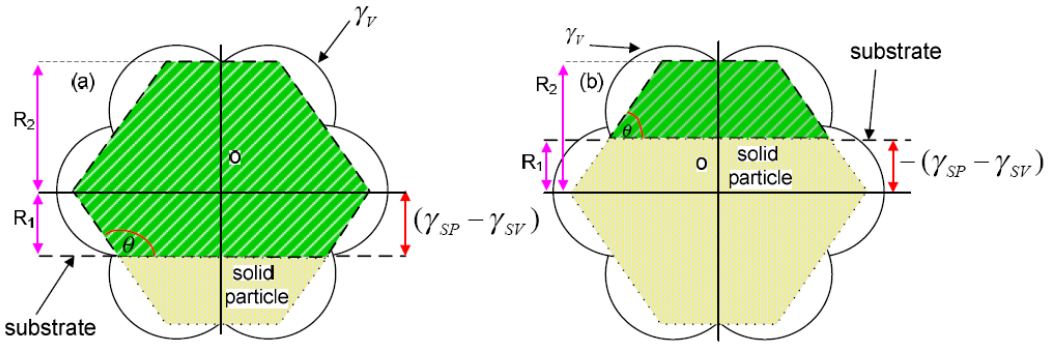

Figure 16: Two particle-substrate configurations describing partial wetting: (a) where $\gamma_{PV} > (\gamma_{SP}-\gamma_{SV}) > 0$, in which $\theta > 90^0$ and (b) where - $\gamma_{PV} < (\gamma_{SP}-\gamma_{SV}) \leq 0$, in which $\theta < 90^\circ$ [47].

Figure 16(a) describes the configuration in which the plane for $g^* = (g_{SP} - g_{SV})$ represents the substrate surface and the base for the equilibrium shape. Figure 16(b) shows a configuration for which $(g_{SP} - g_{SV})$ is negative and the Wulff point is no longer inside the equilibrium shape. By measuring R_1 and R_2 as depicted in Figure 16, the interfacial energy, γ_{SP} can be calculated, according to:

$$\frac{R_1}{R_2} = \frac{g_{SP} - g_{SV}}{g_{PV}} \qquad (21)$$

where γ_{SV} and γ_{PV} are the substrate-vapor and the particle-vapor (at the upper facet) surface energies.

Winterbottom's analysis was used by Heyraud and Metois [18] to examine the equilibrium shape of gold particles on graphite and by Hansen et al. [26] for palladium nano-crystals on Al_2O_3. Sadan and Kaplan [17] used Winterbottom's analysis to determine gold-sapphire interfacial energy. They obtained values of γ=2.15±0.04 J/m^2 and γ=2.18±0.06 J/m^2 for Au(111) || sapphire(0001) and Au(100) || sapphire(0001), respectively.

Although this analysis is simple to implement, it still suffers from some flaws. It demands that the metal-ceramic interface will be flat and co-planar with the surface of

the substrate (which is not that common, as surface roughness and grooves are sometimes present at surfaces and interfaces), and that the particle examined will be a single crystal. Since the particles equilibrated are small in size, the tools that aid their characterization must be accurate enough in order to allow the exact measurements of R_1 and R_2. Segregation effects can also change the ECS (lower surface and interface energies) and the analysis requires prior knowledge of the particle-vapor and substrate-vapor surface energies. In addition, systems that exhibit contact angles smaller than 90^0 will expose only a small portion of their ECS above the substrate, making the determination of the Wulff point harder and inaccurate.

2.3.2.4 Segregation to Surfaces and Interfaces

The segregation of impurities and chemical components to the surfaces, interfaces and grain boundaries is a well known and studied phenomenon. Several models have been suggested for the analysis of this phenomenon [5,6,48,49,50,51,52,53] but will not be elaborated in the scope of this work. The segregation of impurities to the surface decreases the surface energy, according to the Gibbs adsorption isotherm (equation (2)). The most important consequence from the Gibbs isotherm is that *if the segregation (to the surface, interface or grain boundary) causes the reduction of the surface (or interface) free energy, then it will happen (within kinetic limitations), and the impurity or the chemical component will segregate*.

The behavior in the case of metal-ceramic systems is similar, but now segregation will be dependent upon bonding at the interface. This could increase or decrease the segregation beyond the one observed for the isolated ceramic or metal. Reactive elements such as Ti (commonly used in active brazing alloys) segregate to the metal-ceramic interface, where they can react with the components of the ceramic.

Equation (2), while thermodynamically correct, is difficult to implement, since it requires the value of $d\gamma / d\ln C_i$ and this is not always possible. In order to solve that, several alternative approaches were suggested [54,55,56] that relate solute concentration at the surface, C_s, to bulk concentration, C_b, according to the *Langmuir-McLean equation* [54]:

$$C_s / C_b = \exp\left(-\Delta G^{segr} / RT\right) \quad (22)$$

where ΔG^{segr} is the free energy for segregation of mole solute. For values of $\Delta G^{segr}<0$ segregation will increase the solute content in the bulk and decrease with temperature. Most of the approaches consider ΔG^{segr} as comprised of three terms: the first one is based on nearest neighbor bond breaking, and foresee that the component with the lowest heat of sublimation will be the one to segregate to the surface. The second term is based on elastic strain energy and it foresees that segregation will occur when the size difference between comprising elements is large. The third term deals with the enthalpy of mixing of the components. The extent of segregation depends on the relative contribution of each of the terms, which could vary greatly, but has been proved true in foreseeing segregation in a large number of metal-ceramic systems [54,55,56]. Lipkin et al. [57] for example, found that heat treatment of gold-sapphire interfaces in a carbon rich environment causes a reduction of two orders of magnitude in interfacial fracture energy due to carbon segregation to the gold-sapphire interface.

2.3.2.5 Orientation Relationship (OR) at Solid-Solid Interfaces

When a new solid-solid interface is formed, the two crystals brought together orient themselves in such a crystallographic orientation so that the interfacial energy is minimized. The equilibrium shape of the interface will be the one with the lowest possible energy (or lowest energy configuration). Close packed planes and directions in both metals and ceramics tend to align themselves according to this configuration.

When the interface deviates from the ideal OR (i.e. from a perfect low indexed planes at the interface), accommodations will be made to compensate the mismatch created through the creation of interfacial steps and dislocations. Elssner et al. [58] indicated that a slightest deviation from the exact $(110)_{Nb} \| (0001)_{Al_2O_3}$ OR at the Nb-Al_2O_3 system (diffusion bonded at UHV) was accompanied by the creation of steps at the metal-ceramic interface. The (110) planes of Nb were observed to bend around these created steps. Recent studies conducted on single crystals of gold on sapphire by Sadan & Kaplan [17] indicate a higher frequency of the Au(111)||sapphire(0001) morphology, meaning that this orientation has lower energy.

Fecht and Gleiter [59] in their 'lock-in' model suggested that surface metal atoms in close packed planes will fit themselves into the ceramic surface by rotation of the metallic crystal. However, effects of surface energy anisotropy of metal crystals were neglected as well as impurity adsorption. Obviously, these can affect the metal-ceramic interface.

2.4 Metal-Ceramic Joining, Spreading and Reactive Spreading

Metal-ceramic joints have been in the heart of many industrial and research applications and studies from the past century. The vast majority of metal-ceramic joints manufactured in today's industry have to live up to strict demands such as high strength, high reliability, vacuum tightness and more. In order to achieve that, interface engineering is needed.

Different techniques have evolved during the years for creating such joints. Mortimer et al. [60] for example, demonstrated that surfaces that exhibit deviations from stoichiometry become chemically reactive thus improving wetting. In their work, Mortimer et al. changed the ratio of U/O in UO_2 from 2.001 to 2.084, which led to a decrease in contact angle of Sn on UO_2 from 166° to 84°. A similar behavior was observed in the Cu/TiC system, where the contact angle decreased with a decrease in the carbon content [61]. Such surface modifications can be achieved through electron or ion bombardment for example. Other joining techniques exist such as diffusion bonding, joining using different lasers and more, but the two most common routes leading to the creation of such joints are the *Metallization Process* and *Reactive Joining*.

The metallization process, as was first patented by Pulfrich [62,63,64] and Nolte and Spurck [65], is based on creating a metal layer on the ceramic. A suspension of refractory metals (mostly based on Mo, W and Mn) is sprayed or painted on the ceramic surface and then sintered at high temperatures, usually in a wet hydrogen atmosphere. Sintering produces a continuous metallic layer strongly bonded to the ceramic surface that is later on nickel plated and brazed to the metal part. Metallization suspensions contain (besides metal powders) an organic phase composed of different solvents, binders and surfactants that aid in the application and handling of the suspension on the ceramic surface, and during sintering decompose thermally. At the sintering temperatures, the refractory metal is still solid, but the glass phase that forms (from

MnO, SiO_2 and Al_2O_3 that originate from the suspension or from the glass phase of the ceramic) is liquefied and penetrates the inter-granular spacing at the ceramic surface on one side and at the refractory metal on the other side. Upon cooling, the glass phase solidifies and creates a mechanical locking of the refractory metal to the ceramic surface [66,67,68,69]. The most common metallization process is known as the Mo-Mn process, where the metallization paint is comprised of Mo and Mn with a Mo:Mn ratio of ~4:1 [65]. Different compositions are formulated according to the glass phase content of the ceramic member; suspensions designated for metallization of sapphire or high Al_2O_3 content ceramics usually contain glass phase forming additives, such as SiO_2, MnO, CaO, Fe_2O_3 and the like.

The metallization process is very common in today's industry, although it suffers from some disadvantages since it is comprised of many stages and thus time consuming, it is sensitive to the metallization layer thickness and homogeneity, thermal cycle parameters and atmosphere and other factors.

Contrary to the multi-stage metallization process, the *Active Joining* or *Active Metal Brazing* process is a one-shot process. Since most industrial ceramics have an ionic character, they are not readily wet by common brazing filler metals. Brazing filler metals are mostly based on copper, silver, gold and nickel; these are poor wetting metals on widely used ceramics, such as Al_2O_3, as can be seen in Table 1.

Metal	Contact angle	substrate	Temperature [K]	Atmosphere	Reference
Cu	155°	Al_2O_3	1373	-	[1]
Ag	$90^{\circ} \pm 1^{\circ}$	99.5% Al_2O_3	1253	Ar	[70]
Au	$131 \pm 2^{\circ}$	α-Al_2O_3	1381	Ar	[41]
Ni	150°	Al_2O_3	1773	-	[1]

Table 1: Contact angles of common liquid metals used as base metals for brazing alloys on Al_2O_3.

Common braze filler metals readily wet most usable metals and alloys, such as stainless steels, refractory metals and alloys, iron-based alloys and more. In order to achieve good wetting on the ceramic side, the brazing filler metal is alloyed with small amounts of wetting promoters; reactive metals such as Ti (most common), Zr, V, Cr and Hf. These metals induce a change in the structure and properties of the metal-ceramic interface, whose final result is the reduction of the $\gamma_{solid\text{-}liquid}$ interfacial energy. The

wetting or spreading in such systems is usually referred to in the literature as *Reactive Wetting / Spreading*.

Numerous results can be found in the literature about wetting promotion achieved through these active elements addition, with titanium being the most studied, due to its high affinity to oxygen and carbon that comprise many industrial ceramics. Kapoor et al. [71] for example, reported that silver alloyed with 2 at.% Ti has exhibited a final contact angle of 40-45° on polycrystalline Al_2O_3, compared to 135° for pure silver (samples were vacuum brazed). Akselsen [72] reported that improved wetting of Si_3N_4 and SiC is achieved due to Ti additions of 10 at.% to AgCu eutectic brazing alloy, while 30 at% Ti is needed to obtain same results on Al_2O_3 (due to its higher stability). Finite contact angles for these three systems were in the range of 10-15°. Howe reported that additions of 2-9 at.% Ti to copper improved wetting on N-containing ceramics (AlN, BN, Si_3N_4) having finite contact angles of ~10° compared to 135° for pure copper [1]. The improvement in wetting due to the addition of a reactive element such as Ti is also pronounced in the work of adhesion. The reduction in $\gamma_{solid\text{-}liquid}$ is accompanied by an increase in W_{ad} upon these additions, as evidenced by equation (11). Li [73] for example, found a sharp increase in W_{ad} of Cu on vitreous carbon at 1350K, when 12.6 at. % Ti was added (258 mJ/m^2 vs. 2700 mJ/m^2 in the alloyed state). Meier et al. [74], found a value of 500 mJ/m^2 for W_{ad} of pure Cu on Al_2O_3 at 1525K, while Kritsalis et al. [75] found that alloying with 10 at. % Ti increases W_{ad} to 2500 mJ/m^2 (conducted at 1373K). A further increase in W_{ad} was found [76] after addition of 20 at. % Ti at 1475K, giving a value of 2670-2790 mJ/m^2. Gremillard et al. [77] found that additions of 1 wt. % Ti to a Sn-3wt. % Ag alloy decreases the contact angle on sapphire from 150° to 25°.

Since Ti is highly reactive, it can also have a negative effect on the mechanical properties of the metal-ceramic joint created using active brazing filler metals. Vianco et al. [78], reported poor hermeticity of Al_2O_3-Al_2O_3 brazed joints having a Fe-29Ni-17Co alloy spacer and Ag-Cu-Ti active filler metal. In this system, Ti was scavenged away from the liquid alloy-ceramic interface by Ni from the Fe-29Ni-17Co spacer, thus preventing it from enriching the interface and reducing interfacial energy. Similar results were found by Valette et al. [79] for the alumina/CuAgTi braze/CuNi system, where Ti was consumed from the liquid alloy-ceramic interface by Ni from the CuNi substrate. The wetting of TiC for example, was studied by Frage et al. [80] using non-reactive metals (Cu, Ag, Sn, Au) and their Ti-containing alloys. Initial contact angle of

Cu, Au and Ag was ~120-130° and ~105° for Sn. Upon addition of 1 at. % Ti, a drastic decrease in contact angle was observed, to 30-35°.

There is no doubt that a large and well established database exists about the influence of active element additions on wetting and joining of ceramics. Nevertheless, there is still an ongoing argument among researchers about the exact mechanism and related thermodynamic phenomena taking place at the metal-ceramic interface that actually drive spreading and wetting.

Despite these arguments, it is agreeable that the metal-ceramic interface is enriched with titanium during the high temperature process, where it forms some interfacial compound, in the form of an oxide if an oxide ceramic is used, or some other Ti-containing compound in case of other ceramics. The question whether the Ti-containing compound is formed during liquid state or during cooling, when the brazing filler alloy solidifies, remains at the heart of the argument.

Two general approaches exist. The first assumes that the adsorption of Ti at the metal-ceramic interface alone is responsible for the improvement in wetting and the reduction of interface energy, with reaction products forming only later, during cooling and solidification. The second assumes that the formation of a reaction layer at the interface is the only phenomena responsible for the improved wetting, allowing the filler metal to wet a new reaction product surface instead of the ceramic surface (that is not readily wet by common braze metals). A brief description of these two important approaches now follows.

2.4.1 Adsorption/Ridge Controlled Spreading (Adsorption First Approach)

The approach holding the adsorption of Ti at the metal-ceramic interface responsible for the improvement in wetting was formulated by E. Saiz, R. M. Cannon and A. P. Tomsia [81,82].

Most wetting and spreading data achieved experimentally is usually based on sessile drop experiments. In such setups, the Young equation (equation (9)) is used, and the one dimensional equilibrium macroscopic contact angle, θ_{1D}, is measured. Since full, three dimensional equilibrium is rarely achieved, the validity of this equation can be sometimes doubtful and the conclusions deduced from θ_{1D} do not represent the true equilibrium conditions. Young's equation is based on the assumption that the solid

substrate is rigid and insoluble and that triple line movement is possible only in a direction parallel to the substrate. In cases where the substrate is not perfectly rigid and inert, vertical forces deform the solid at the triple junction. At this point equilibrium demands movement in two directions and a dihedral angle forms (Figure 17 and equation (13)). The description of a substrate as rigid and inert is good for low temperature systems (such as organic liquids on metals and ceramics), but when examining molten metals on ceramics, high temperatures are used (typically >0.2-0.5T_m of the substrate) and some dissolution of the substrate will occur due to local diffusion or solution-precipitation. This will eventually lead to the formation of a ridge at the substrate surface in the triple junction, as can be seen in Figure 17.

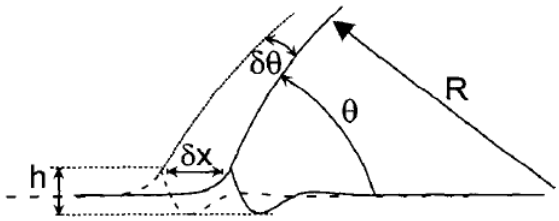

Figure 17: Schematic illustration of the expected shape of a ridge that would form by local diffusion in response to horizontal and vertical forces at the junction [81].

Assuming the ridge that forms at the triple line moves ahead with the advancing (or receding) liquid front, then Young's equation is valid.

According to Saiz et al. [81,82,83,84], the spreading process can be divided into four regimes, depending upon the degree of ridge evolution at the triple point. In *Regime I*, deformation of the substrate at the triple point will be due to elastic strains in response to the forces exerted at the triple junction. Driving forces for spreading include capillary forces that drive the droplet towards a constant curvature shape and the contact angle towards θ_{1D}, hydrostatic pressure and gravitational effects and the force exerted by the contact line tension that drives θ away from θ_{1D}. Here, the main force retarding spreading is the liquid viscosity. Spreading times under this regime are very short (~10^{-5} s for liquid metals) and can be estimated using equation (23):

$$t_{cc} \approx \frac{h \cdot r_0}{g_{lv}} \tag{23}$$

where η is liquid viscosity, r_0 is the initial droplet radius and γ_{lv} is the liquid-vapor surface energy.

When diffusion processes or solution precipitation takes place, spreading enters *Regime II*. Here, substrate deformation occurs at the triple junction and atomic movements will determine the two dimensional equilibrium state. A ridge will evolve at the triple junction, in a way similar to thermal grooving of grain boundaries [85]. Under this regime, capillary forces will drive θ towards θ_{1D}, the value given by Young, if the ridge moves forward together with the triple junction as can be seen from Figure 17. If the ridge height is small compared to droplet radius, h/R<<0.1 (see Figure 17), than the macroscopic contact angle θ, still tends to match the one given by Young. Spreading kinetics will be determined by the velocity of ridge movement. If conditions are not sufficient for ridge movement, the liquid front can be pinned by the ridge and not move forward. Experiments held under this regime are liable to present no hysteresis in contact angle.

When ridge formation and growth is rapid compared with the spreading velocity, spreading enters *Regime III*. Here, capillary forces can no longer drive θ to the θ_{1D} values, since the reduction in free energy that stems from ridge growth is diminished by the growing deviation from θ_{1D}. Young's equation is no longer valid under this regime.

When complete two-dimensional equilibrium is reached, spreading is in *Regime IV*. Equilibrium exists at the triple point and the droplet shape is of constant curvature. The contact angle in this situation, θ_{2D}, can be related to the dihedral angle ϕ_v, according to $\theta_{2D} = \pi - \phi_v$ and to θ_{1D} according to:

$$\cos\theta_{2D} = \cos\theta_{1D} + \frac{\gamma_{sl}}{\gamma_{lv}} \cdot (\cos\phi_s + 1) \qquad (24)$$

During wetting and spreading, the system will go through some or all of the stages, with time constants spent at each stage differing from one system to another.

Wetting experiments of liquid Cu on sapphire conducted by Saiz et al. [81] show a common contact angle for both advancing and receding contact angles of 114±3°. After cooling, the solidified droplet was removed and 10-40 nm ridges were detected at the triple junction, using atomic force microscopy (AFM). Each drop also exhibited a

breakaway event with a formation of a second ridge. The fact that both advancing and receding angles were roughly the same (very small hysteresis) and that the ridge height was small compared to the droplet radius of curvature ($h/r<10^{-4}$) indicate that spreading took place under regime II. Wetting experiments of Al on sapphire at 1150°C [81] show an oscillatory behavior of observed contact angle, between 56° and 80°. Examination of the sapphire surface after droplet removal reveals a series of rings at the surface, each corresponding to a jump in the contact angle, having a ridge of ~1μm between each ring. Evaporation of Al decreases the contact angle to values that exceed the stability range of the ridge and the liquid front jumps and breaks away so new equilibrium can be reached, giving rise to another ridge. Similar evidence of ridge formation in the Ni/sapphire system at 1500°C was also obtained [86].

Spreading in reactive systems is usually attributed to the formation of reaction products at the metal-ceramic interface caused by reduction of the ceramic surface by Ti or by the creation of intermetallic compounds. Many arguments exist whether these products form during liquid state or after solidification, whether adsorption of the reactive element alone is enough to drive spreading. Saiz et al. [82] have divided reactive spreading into four consecutive stages - fluid flow, adsorption of an active element at any of the interfaces, triple point ridging and formation of a new compound at the solid-liquid interface (see Figure 18).

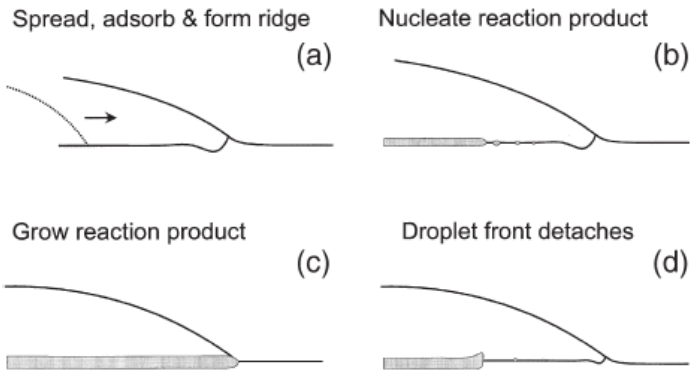

Figure 18: Schematic illustration of reactive spreading introducing the four stages [82].

Analyzed for the case of reactive brazing alloy with small additions of an active element (with an activity of a_R), reactive spreading starts with the liquid first entering in contact with the substrate (Figure 18.a). The molten alloy can spread on the substrate according to regimes I-IV mentioned above, depending on the amount of substrate deformation at the triple junction. At the start of fluid flow stage, capillary forces drive

the homogeneous liquid towards a constant curvature shape and θ to θ_{1D}. The activation free energy accompanying this stage, ΔG_W, is derived from solid-liquid interactions and forms the energy barrier of the process required to replace one molecule of the receding fluid from the attachment site on the solid with one from the advancing fluid. If the liquid-substrate chemical interactions are strong at high temperatures, a larger ΔG_W is expected and spreading will be slower.

The reactive spreading system can be treated as a multi-component one, and as such, requires that the interfaces will develop an equilibrium level of adsorption by diffusion among all phases if the system itself is in equilibrium. The relation of adsorption to equilibrium interfacial energies was formulated in the Gibbs adsorption isotherm, equation (2). Active elements added to braze alloys usually have high surface energies (calculated surface energy of Ti for example, is 1550 mJ/m^2 at its melting point, 1939K [87]), and according to Saiz et al. [82] "*it is hard to see how an alloy containing a low fraction of such an element could bring θ far below 90° without strong adsorption at the metal-oxide interface*". If adsorbing the reactive element is the kinetically limiting step and its interaction with the substrate is stronger than that of the solvent, a decrease in the spreading velocity of receding fronts can be expected. The critical spreading velocity, above which adsorption at the triple line could not accompany spreading and influence the driving force via a reduction in γ_{sl} can be estimated as [84]:

$$v_{cr}^{adsorption} \leq \frac{6 \cdot a \cdot X_R \cdot D_{liq}}{a} \tag{25}$$

where D_{liq} is the diffusivity in the liquid, a is the atom spacing for the solid, X_R the adsorbate fraction in the liquid and α(<1) a sticking coefficient that describes the chance that an atom jumping from the liquid would attach to the surface at the triple line.

The following stage, after adsorption of the reactive element, is ridge formation, caused by the vertical component of surface tension induced at the triple junction. This gives rise to the use of dihedral angles (equation (13)). As in the case of a critical spreading velocity that allows adsorption, a critical velocity beyond which a ridge will not form (since the jump frequency becomes too slow compared to spreading velocity) can be estimated as [82,84]:

$$v_{cr}^{ridge\ formation} = \frac{6 \cdot D_{sl}}{a} \tag{26}$$

where a is the jump distance and D_{sl} the diffusion coefficient at the solid-liquid interface. For liquid Cu on Al_2O_3 at 1100-1500°C, the upper limit for the velocity of a 10 nm ridge is ~10^{-10}-10^{-5} m/s [82].

After adsorption has begun and the substrate surface is enriched with the reactive element, reaction product starts to form and nucleate. Local defects at the surface can serve as nucleation sites for the reaction product. If a finite nucleation barrier exists for the reaction product, then the liquid front can move ahead of the reaction layer on an unreacted substrate surface (termed *Dry Spreading*). If the nucleation of reaction products are extremely fast, spreading kinetics are controlled by the growth of the reaction product, and reduction observed in the macroscopic contact angle is due to the fact that the triple line is pinned by the growing reaction layer. Upon completion of this stage, the contact angle measured is that of the liquid on the reaction product (Figure 18.c).

Kritsalis et al. [75] studied the CuTi/sapphire system under vacuum at 1373K and found that two reaction layers formed at the metal-ceramic interface. The first layer, on the ceramic side of the interface, was identified as TiO. The second layer, between the first layer and the metal alloy, was identified as Cu_2Ti_2O and assumed to form during solidification. Contact angle measurements indicate a sharp decrease in the first few seconds of experiment (after melting of the alloy) from an initial angle of ~106° to ~85-90°, taken for a Ti molar fraction of 0.095. The authors state that the initial stage of wetting involves adsorption of Ti at the Cu/sapphire interface. It is hard to believe that the observed decrease in contact angle during the first few seconds is due to reaction products forming at the interface, since in such short time periods reaction is limited and dependant on the dissolution of substrate surface and the adsorption of Ti at the interface.

Liquid metal-ceramic interfaces are rather difficult to characterize since the interface itself is surrounded by the liquid metal on one hand and by the substrate on the other, making it unsuitable for conventional microscopic observation. One characterization technique that can overcome this is *neutron reflection*. Since neutrons can penetrate centimeters of condensed matter (with the exception of B and Cd who are strong absorbers) they can give insight into the interface while the metal is still liquid

and enable in-situ observation. Xiao et al. [88] and Derby et al. [89] studied interfaces of Sn and Ag-Cu-Ti alloy (Cusil ABA; 70Ag-28Cu-2Ti) with sapphire. The Sn-sapphire interface was also studied after the addition of a ~20 nm Ti interlayer. Xiao et al. and Derby et al. noticed that Ti enriches the metal-ceramic interface in the liquid state (Ti is noticeable by neutron reflection due to its negative scattering length compared to all other components in this system) but were unable to quantify it. Neutron reflection is sensitive to surface roughness, and very thin (few nm) interfacial layers are hard to detect. Nevertheless, the authors concluded that *the assumption of no interfacial layer between Sn and sapphire is probably not correct*. In the Ag-Cu-Ti/sapphire system, a thick interfacial reaction layer was found to be comprised of Cu_3Ti_3O. A second, Ti-rich interfacial layer was found between the sapphire and Cu_3Ti_3O and attributed to Cu_2Ti_4O or Ti_2O.

Froumin et al. [90] studied the interface of CaF_2 with two Ti-containing alloys, In-Ti and Cu-Ti. They suggested that the improved wetting achieved due to Ti additions is related to Ti-enrichment of the interface region rather than to the formation of liquid titanium fluorides. Experimental results backed by DFT analysis indicates that a very thin adsorbate layer is formed at the interface and a thicker intermetallic compound layer nucleates on top of it and grows during cooling and solidification.

2.4.2 Reaction Product Controlled Spreading

As mentioned above, additions of active elements to brazing filler metals can improve wetting in metal-ceramic systems. According to N. Eustathopoulos [91], this improvement in wettability is achieved through the creation of a continuous layer(s) of compound(s) at the interface, by reaction of the active element with the substrate.

The driving force for wetting of a pure liquid on a smooth surface of an inert solid can be defined simply as:

$$F_d(t) = s^0_{SV} - s^0_{SL} - s^0_{LV} \cdot \cos q(t) \tag{27}$$

where σ_{ij} are the characteristic surface energies of the system and $\theta(t)$ is the instantaneous contact angle. At equilibrium, $F_d=0$, and the Young equation is obtained. Spreading kinetics for such systems will be controlled primarily by the viscous flow and

described by a power function of the drop base radius R vs. time t as $R^n \sim t$, with n equal to 10 [91]. While this description is good for non-reactive systems, where spreading times are in the order of 10^{-1} s, when dealing with reactive systems, spreading times increase to 10^1-10^4 s [92] and this definition is no longer valid. Since interfacial reactions are involved, additional factors influence the driving force for wetting, such as reaction kinetics, diffusion of the active element and more.

Some 15 years ago, Landry and Eustathopoulos [93] proposed the Reaction Product Control (RPC) model for wetting in reactive metal-ceramic systems. According to this model, the behavior of a reactive system is given in Figure 19.

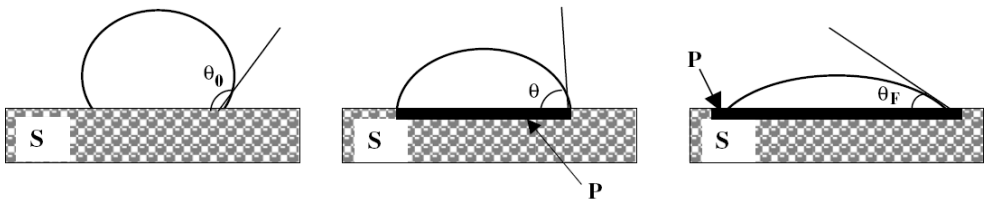

Figure 19: Schematic presentation of the RPC model describing the change in contact angle and interfacial reaction product layer in a reactive metal-ceramic system [93].

The initial contact angle in a reactive system is θ_0, which is the contact angle on the clean and unreacted substrate ($\theta_0 \approx \theta_s$). After a transient stage, a quasi-steady configuration is established at the triple line and the advance of the liquid front is inhibited by the non-wettable substrate. The model now suggests that the only way for the liquid front to move ahead is by lateral growth of the wettable reaction product layer until the macroscopic contact angle equals the equilibrium contact angle on the reaction product ($\theta_F \approx \theta_P$).

According to the RPC model and other works by Landry [94] et al. and Eustathopoulos [91,95], it is claimed that spreading rates in reactive systems are not governed by viscous flow of the liquid metal (as is the case for non-reactive systems), but by the dominant and slower of two processes - local reaction kinetics at and diffusion of the active element to the triple line.

As for *reaction controlled (limited) spreading*, Landry and Eustathopoulos [93] suggest that the kinetics of the chemical reaction that takes place at the triple line is rate limiting when compared to the bulk drop, where diffusion is comparatively rapid. In cases where the reaction does not change the global composition of the drop

significantly and a steady configuration is obtained at the triple line, spreading is constant with time:

$$\boldsymbol{R - R_0 = K \cdot t} \tag{28}$$

where R and R_0 are the instantaneous and initial drop base radius, K is a system constant and t the time. Landry and Eustathopoulos established this on a reactive Al/vitreous carbon system, where the interfacial reaction product is Al_4C_3 [93].

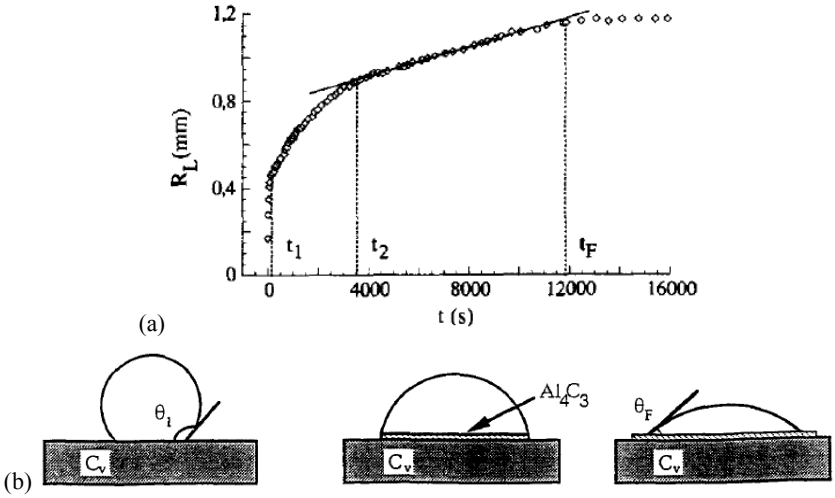

Figure 20: (a) Drop base radius vs. time curve for the reactive Al/C_v system at 1100K in a vacuum of 10^{-3} Pa [93]. (b) Schematic representation of the Al/C_v system in light of the RPC model [91]. Here, $\theta_1 = \theta_s$ and $\gamma_F = \gamma_{Al/Al_4C_3}$.

In this system, wetting is promoted through the creation of an interfacial layer of the wettable Al_4C_3 (Figure 20). During the initial stage of spreading, between t=0 t_1=400 s de-oxidation of the liquid Al drop takes place, followed by a second non-linear stage between t_1 and t_2. The final stage, between t_2 and t_F is linear, as can be seen from the $R(t)$ curve. θ_1 is the contact angle of the de-oxidized liquid Al on the unreacted C_v, and θ_2 is the first contact angle on the reaction product layer. This transition between the two contact angles is actually a transition from a clean substrate to a substrate covered by the reaction product. For $t>t_2$, the triple line has a steady configuration and spreading takes a linear form. Similar behavior was also observed for CuSi alloys on SiC [96] and on C_v [97] and for CuAg-Ti on Al_2O_3 [91].

The spreading rate and contact angle can be modeled and related to time, based on the next two assumptions [92,95]:

1. The instantaneous contact angle θ is greater than but very close to the equilibrium contact angle θ_e at all times. θ_e is given by the Cassie equation [98]:

$$\cos\theta_e = a \cdot \cos\theta_P + (1-a) \cdot \cos\theta_S \tag{29}$$

where α is the surface coverage of the reaction product, θ_P and θ_S are the equilibrium contact angles of liquid on P and S, respectively ($\theta_P \approx \theta_F$ and $\theta_S \approx \theta_0$).

2. The reaction rate is controlled by the dissolution process at the substrate/liquid alloy interface.

Based on these assumptions, the change in contact angle with time t is given by:

$$\cos\theta_F - \cos\theta = (\cos\theta_F - \cos\theta_0) \cdot \exp(-k \cdot t) \tag{30}$$

Now the relation between spreading rate U and θ is given by:

$$\begin{aligned} \frac{U}{F(\theta)} &= k \cdot \left(\frac{3 \cdot V}{\pi}\right)^{1/3} \cdot (\cos\theta_F - \cos\theta) \\ F(\theta) &= -\frac{\cos\theta \cdot (2 - 3 \cdot \cos\theta + \cos^3\theta) - \sin^4\theta}{\sin\theta \cdot (2 - 3 \cdot \cos\theta + \cos^3\theta)^{4/3}} \end{aligned} \tag{31}$$

where V is the droplet volume. The constant k is proportional to the kinetic constant k_d and the driving force $\Delta\mu$ of the dissolution process. According to equations (30) and (31), plots of $(\cos\theta_F - \cos\theta)$ and $U/F(\theta)$ vs. time are expected to be linear and indeed, these were shown linear for Ni-63 at.%Si alloy/C_v [99] and for CuAg-5 at.%Ti on three different substrates [100], respectively.

One of the most commonly studied cases is the CuAgTi/Al_2O_3 system. This eutectic CuAg alloy is widely used in commercial brazing processes for metal to metal joining and with the addition of Ti for metal-ceramic joining also. One of the recent studies of this system was carried out by Voytovych et al. [101]. Wetting experiments were done in the sessile drop setup under vacuum and using He as the atmosphere gas.

Excellent wetting of the sapphire substrate was observed for the CuAg-2.9 at. % Ti alloy, with $\theta_F = \pm 3^{\circ}$. As for the interfacial microstructure formed, two layers were identified. The first, in direct contact with the sapphire surface, was identified using electron probe micro-analysis (EPMA) as $Ti_{1.75}O$ (which could be Ti_2O or Ti_3O_2). The authors state that this layer may have precipitated during cooling, as also suggested by Stephens et al. [102]. The second layer, in contact with the $Ti_{1.75}O$ layer on one side and with the AgCu filler metal on the other side, was identified using x-ray diffraction (XRD) and EPMA as Ti_3Cu_3O. This M_6X-type compound, was studied by Carim [103] and Kelkar et al. [104] who characterized it, and found that it holds a metallic character (having electrical resistivity in the order of magnitude of Ti-containing alloys and 20 orders of magnitude lower than that of alumina). The same compound was also identified by Stephens et al. [102]. By the creation of a metallic character layer, wetting of the AgCu filler metal is promoted, since it no longer wets the ceramic surface but the Ti_3Cu_3O compound.

When the kinetics of the reaction at the interface is high, spreading takes place and the contact angle decreases. This change reduces the actual area for the diffusion of the active element to the triple junction and gradually limits the rate of reaction there leading to a reduction in spreading rates. The spreading now turns into *diffusion controlled (limited) spreading*. Diffusion controlled spreading was modeled by Mortensen et al. [105], who assumed that spreading and triple line reaction rates depend only on the instantaneous contact angle θ:

$$\boldsymbol{U}=\frac{\boldsymbol{dR}}{\boldsymbol{dt}}=\frac{2\cdot\boldsymbol{D}\cdot\boldsymbol{F}(\boldsymbol{t})}{\boldsymbol{e}\cdot\boldsymbol{n}_V}\cdot(\boldsymbol{C}_0-\boldsymbol{C}_e)\cdot\theta \quad \xrightarrow[\theta\approx\frac{4V_d}{\pi R^3}]{\theta\le 60^0} \quad \boldsymbol{R}^4-\boldsymbol{R}_0^4=\boldsymbol{K}'\cdot\boldsymbol{V}_d\cdot\boldsymbol{t} \tag{32}$$

where D is the diffusion coefficient in the liquid, n_V the number of reactive solute moles per unit volume of the reaction product, e the reaction product layer thickness, C_o and C_e are the nominal drop reactive solute concentration and the concentration of reactive solute in equilibrium with the reaction product (C=C_e at the triple line) and $F(t)$ is a function of time but varies so little that it can be taken as constant ($F(t)$= ~0.04).

This formulation was found suitable for the reactive AgCuSn-Ti/C_v system [99], but not for systems that exhibit rather high finite contact angles such as the Cu-Cr/C_v system [91]. One possible reason for this is that Mortensen's formulation was based on a

reaction that mainly takes place at the triple line, not considering the reaction behind it, at the remaining liquid-solid interface.

Durov and Krasovskyy [106] also studied the $AgCuTi/Al_2O_3$ system in situ and concluded that titanium oxides were formed during the liquid stage (and not during solidification) after observing the formation of a Ti-oxide reaction product layer during the experiment (due to its different color), upon the addition of Ti to the AgCu melt. By these results they reject the results of Derby [89], that were also rejected by Voytovich et al. [107] for the same system.

Santella et al. [108] studied the microstructure of Al_2O_3 brazed with a AgCuSnTi alloy containing 4 at. % Ti (900°C for 20 min in vacuum), and found results similar to Voytovich et al. [101]. Here, the interface was comprised of two layers. The first layer, in contact with the Al_2O_3 surface was identified as γ-TiO using electron diffraction and had a thickness of 0.1-0.2 μm. The second layer, ~3 μm thick, was between the first layer and the alloy bulk and identified as the η phase $Ti_3(Cu_{0.76}Al_{0.18}Sn_{0.06})_3O$ (M_6X type compound) using electron diffraction.

In the absence of an M_6X type compound layer, the creation of a Ti oxide alone at the interface can promote wetting assuming it is formed during liquid state. The contact angle of molten gold on sapphire is very high - 131°±3°, whereas on the TiO contact angle reaches a value of 28°±3° [40].

The issue of the exact mechanism that allows the improvement in wetting in reactive systems is still a matter of debate. On one hand, Saiz, Cannon, Tomsia and co-workers hold the *adsorption/ridge controlled spreading* approach that claims wetting is improved by adsorption of the active element at the liquid-solid interface and not by the creation of interfacial reaction products (that are said to form during solidification). On the other hand, Eustathopoulos and co-workers, based on the *reaction product control* (*RPC*) *model*, claim that wetting is improved by interfacial reaction products accumulating at the interface (mainly at the triple line) and that spreading is controlled by the kinetics of the reaction at the triple line.

According to the RPC model, a continuous reaction product layer always form in reactive systems, but this fact is not true for all reactive systems. A non-continuous reaction layer can actually inhibit spreading by altering the macroscopic nature of the interface. In addition, ridges on the ceramic surface form, especially at the temperatures used for experiments. According to the adsorption/ridge controlled spreading, an

adsorbate layer of the active element forms at the liquid-solid interface and by that lowers the surface energy and promote wetting; ridges at the triple line can pin down the advancing liquid front if they are large enough.

Almost all studies carried out by these two groups are based on sessile drop experiments. Microstructure characterization was carried out almost exclusively by electron probe micro analysis and x-ray diffraction. Transmission electron microscopy (TEM) was rarely used, although interfaces were studied and assumptions made at the atomic level. Gremillard et al. [109] for example, from the group of Saiz and Tomsia, claimed that adsorption of Ti at the interface is responsible for improved wetting, but displayed a high resolution TEM micrograph (the only one) showing a bulk TiO_2 phase and not an adsorbate layer at the sapphire surface in the $SnAgTi/Al_2O_3$ system. Clearly, the use of TEM can enlighten some issues regarding reactive wetting.

It seems that the true nature of reactive wetting can sometimes be comprised of two successive processes, starting with adsorption of the active element at the liquid-solid interface, causing the initial and important reduction in interface energy (and as a consequence, the contact angle), followed by a second stage, the formation of the reaction product layer, which can be a by-product of the adsorption process. Similar approaches were also taken by Kritsalis et al. [75].

2.5 Gold - Titanium - Sapphire System

The system chosen for the current work is comprised of three components; sapphire, (single crystalline Al_2O_3), gold and titanium.

Alumina, Al_2O_3, in its poly and single crystalline forms, is one of the most extensively used and studied ceramic materials. Alumina has a very diverse range of applications, forms, structures and properties. These range from the sub-micron and even nanometer scale and include abrasive materials, artificial prostheses, computer substrates, spark plug insulators and many more. The single crystal shape, *sapphire*, has mechanical properties similar to those of alumina, but its transparency (especially in the IR spectra) and uniform crystal structure enables its utilization for different applications such as substrates for thin metal film deposition, hollow fibers for medical uses, electric arc tubes for lighting and more. Its structural stability at high temperatures allows it to

be joined to metals using commercial brazing processes. As a result, it is often the focus of many industrial and scientific studies [13,110,111,112].

The bulk structure of sapphire is a corundum type that is commonly shared by many oxides of transition metals with the general formula of A_2O_3 such as Cr_2O_3, V_2O_3, Fe_2O_3. The crystallographic bulk structure has a rhombohedral symmetry [113,114], but is generally treated with a hexagonal unit cell. The hexagonal unit cell contains a total of 30 atoms, 6 Al_2O_3 molecules in each unit cell. The lattice parameters are a_0=4.7570 $\overset{0}{A}$, c_o=12.9877 $\overset{0}{A}$, the unit cell volume is V_c=254.52 $\overset{0^3}{A}$ and the space group is $R\bar{3}c$, as determined by Kirfel et al. [115] using synchrotron radiation. The crystal structure is given in Figure 21.

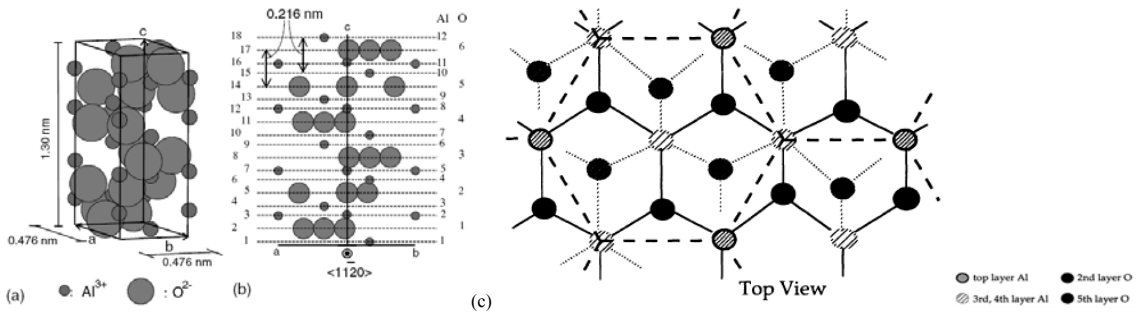

Figure 21: Schematic representation of the bulk sapphire structure: (a) three dimensional view of a rhombohedral unit cell, (b) two dimensional view of the unit cell projected in the <11$\bar{2}$0> direction showing atomic arrangement and Al and O layers [116] and (c) top view illustration of the (0001) sapphire surface [113].

Each unit cell contains 18 atomic planes normal to the c-axis. Six planes contain three oxygen atoms per plane, forming an equilateral triangle, and twelve planes contain one aluminum atom per plane. Oxygen and aluminum layers are 0.216 nm apart. Six atomic layers of this sort fit into the unit cell height (c-axis). Aluminum and oxygen atoms have six and four nearest neighbors, respectively. Bond lengths of Al-O are 1.86 $\overset{0}{A}$ (half of the bonds) and 1.96 $\overset{0}{A}$.

The surface of (0001) sapphire can be either Al or O-terminated, and the nature of the terminating plane will determine the surface properties, especially with respect to an interface with metals. Theoretical calculations [13] and experimental results [13,113] show that the most favorable and stable terminating plane is the single Al plane, favored due to the lack of dipole moments across the surface [13,110,111,113,116]. This is mostly true for (0001) surfaces, while O-termination is favored for (1$\bar{1}$02) surfaces [13]. According to the Al-terminated surface of sapphire, using the lattice parameters

reported in [115], the cation density is 10 cation/nm^2 [117]. In the current study, c(0001) sapphire substrates were used and it was assumed that they are Al-terminated.

For similar reasons, *gold* is very abundant in today's industry, and it is vastly used in the microelectronics industry. Its apathy for oxygen also makes it a good candidate for research, when the harmful effect of oxygen is neutralized. No oxides are formed, and wetting/dewetting experiments can be conducted in air. In addition to its oxidation resistance, the use of gold as a base filler metal in brazing application is also beneficial due to a fairly good match in thermal expansion coefficients of commonly used steels and ceramics. Gold has an FCC structure with lattice parameter of a_0=4.0786 $\overset{\circ}{A}$ [118].

Titanium, together with other active elements (Zr, V, Cr etc.) is commonly used as an alloying element in commercial alloys used for direct joining of metals to ceramics. Titanium acts as wetting agent, promoting wetting and spreading at the metal-ceramic interface. Titanium has a hexagonal structure, with lattice parameters of a_0=2.9505 $\overset{\circ}{A}$ and c_0=4.6826 $\overset{\circ}{A}$ [119].

The gold-sapphire system was thoroughly studied in terms of contact angles and interface energies. Some of the data found in the literature is summarized in Table 2.

System	Contact angle	Interfacial energy [J/m^2]	Temp' [K]	Atmosphere	Ref.
Au-sapphire	132 $\pm 2^\circ$	-	1363	He-H_2 (5%)	[40]
Au-sapphire	133 $\pm 2^\circ$	-	1363	He-O_2 (50%)	
Au-sapphire	140 $\pm 2^\circ$	-	1381	Ar-H_2 (5%)	[41]
Au-sapphire	135°	-	1423	Vacuum	[120]
Au-sapphire	-	1.725	1273	Air, 75 hr	[121]
Au(111)-sapphire(0001)	-	2.15±0.04 (*)	1273	Air	[17]
Au(100)-sapphire(0001)	-	2.18±0.06 (*)	1273	Air	
Au($\bar{1}\bar{1}\bar{1}$)-sapphire(0001)	-	0.889±0.034	1273	Air	[45]

Table 2: Contact angles and interface energies of the gold-sapphire system. (*) These values were determined using surface energy values of 1.4 [J/m^2] for Au(111) and 1.24 [J/m^2] for sapphire (0001).

Lee et al. [46] studied the anisotropy of wetting of molten gold on differently oriented sapphire substrates (R($00\bar{1}2$), A($11\bar{2}0$) and c(0001)) at 1373K and found that contact angle differences were less than 4°, corresponding to changes in the work of adhesion of less than 55 mJ/m^2.

Wang and Wynblatt [122] found through dewetting experiments in UHV, that the addition of 4 at. % Sn and 0.5 at. % Si to gold crystallites reduces interfacial energy with α-SiC by 514 and 546 mJ/m^2. The addition of 2.3 at. % Ge was found to reduce interfacial energy for the same system by 476 mJ/m^2 [123]. Lipkin et al. [57] showed that carbon at the Au-sapphire interface can deteriorate mechanical properties and found a reduction of ~30% in W_{ad} after carbon treatment (related to the adsorption of carbon at the Au-sapphire interface).

As for the gold-titanium-sapphire system, Naidich et al. [124] reported that gold alloys with 5 to 10 at.% Ti form a violet intermediate reaction layer on sapphire, at 1050-1150°C. This layer corresponds to Ti_2O_3. The microstructure of a commercial gold-based active brazing alloy, gold-ABA®, was studied by Singh et al. [125] who joined YSZ to stainless steel using gold-ABA (96.4Au-3Ni-0.6Ti) and gold-ABA-V (97.5Au-0.8Ni-1.75V) at 1030°C and 1090°C in vacuum, respectively. The surface of the ceramic side (YSZ) was found discolored, after reduction by the Ti, forming TiO at the interface.

2.5.1 Equilibrium Shapes

2.5.1.1 Equilibrium Shape of Gold

Reports on gold's equilibrium shape indicate that it consists of {111} and {100} facets that are connected by sharp edges to curved surfaces [17,126]. Sadan and Kaplan [17] performed dewetting experiments of gold on c(0001) sapphire in air, and found that equilibrium shape contained two preferred orientations - Au(111) and Au(200). An example of the equilibrium shape of gold obtained by Sadan et al. [17] can be seen in Figure 3, after dewetting and equilibration for 100 hr in air. The equilibrium shape of gold crystallites on graphite was studied by Heyraud et al. [45] and found to consist of {111} and {100} facets. To the best knowledge of the writer, the equilibrium shape of gold alloyed with titanium was not yet studied.

2.5.1.2 Equilibrium Shape of Sapphire

Equilibrium shapes of ceramic materials have been studied by examining the equilibrium shapes of cavities and pores etched at the surface. In general, ceramic surfaces change from flat and vicinal ones to a faceted structure, where unstable planes tend to break to lower energy facets [127]. Choi et al. [128] reported that five stable surfaces were identified on well annealed samples (up to 50 hr at 1600°C) - **c**(0001) (lowest energy), **r**$\{\bar{1}\,012\}$, **s**$\{1\bar{1}\,01\}$, **a**$\{11\,\bar{2}\,0\}$ and **p**$\{11\,\bar{2}\,0\}$ (basal, rhombohedral, structural rhombohedral, prismatic, pyramidal and prismatic planes, respectively). Similar results were achieved by Kitayama et al. [19] on pure sapphire. An example can be seen in Figure 5.

3. Research Goals

The goal of this work is to study the influence of an active element on the thermodynamics and morphology of surfaces and interfaces in a metal-ceramic system. These goals were achieved through the characterization of the equilibrium crystal shape of metal particles that contain an active element on a ceramic substrate, and comparison with pure metal particles on the same substrates. Characterization was conducted using electron and ion microscopy.

The selected material system includes gold particles, doped with titanium, and equilibrated on selected sapphire surfaces. The results are compared with a titanium doped commercial alloy used for metal-ceramic brazing, gold ABA®.

4. Experimental Methods and Procedures

Experiments conducted in this work were divided into two sections, with the first being the isolated gold-titanium-sapphire system and the second, a commercial gold-based brazing alloy-polycrystalline Al_2O_3 system.

The gold-titanium-sapphire system was used in order to examine the influence of titanium on the nature (structure and properties) of the metal-ceramic interface.

4.1 Dewetting and Equilibration Experiments (Au-Ti-Sapphire System)

Sapphire substrates of 99.99% purity (supplied by 'Gavish Industrial Technologies and Materials LTD') with a basal c-plane (0001) orientation were used for the dewetting experiments. Polished substrates were ultrasonically cleaned in acetone and ethanol, followed by annealing in air at 1200°C for 2 hr. A layered coating was sputtered on the sapphire substrates, as depicted in Figure 22.

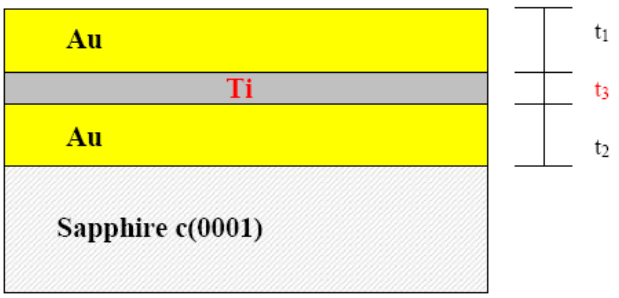

Figure 22: Layered coating sputtered on c(0001) sapphire substrate for dewetting experiments.

The thickness of layers 1 and 2 corresponding to the gold was 204 nm each and the thickness of the titanium layer (layer 3) was 8 nm. The layer thickness was confirmed using a cross section sample in TEM. This layer thickness gives a total Ti concentration of 1.86 at. % (0.46 wt. %). The titanium layer was entrapped between the two gold layers in order to avoid exposing it to oxygen in ambient air, thus preventing it from oxidizing.

Samples were then annealed in a quartz tube furnace under a constant flow of Ar+7%H_2 atmosphere gas. This atmosphere was chosen in order to minimize oxygen content during experiment. Samples were placed on an Al_2O_3 plate and put inside a

sapphire tube through which the process gas entered. This setup was meant to minimize sample contamination by Si and/or SiO_2 originating from the furnace quartz tube. Constant gas flow throughout the process ensures no outside contamination enters the sample area.

A general illustration of the experimental setup is shown in Figure 23.

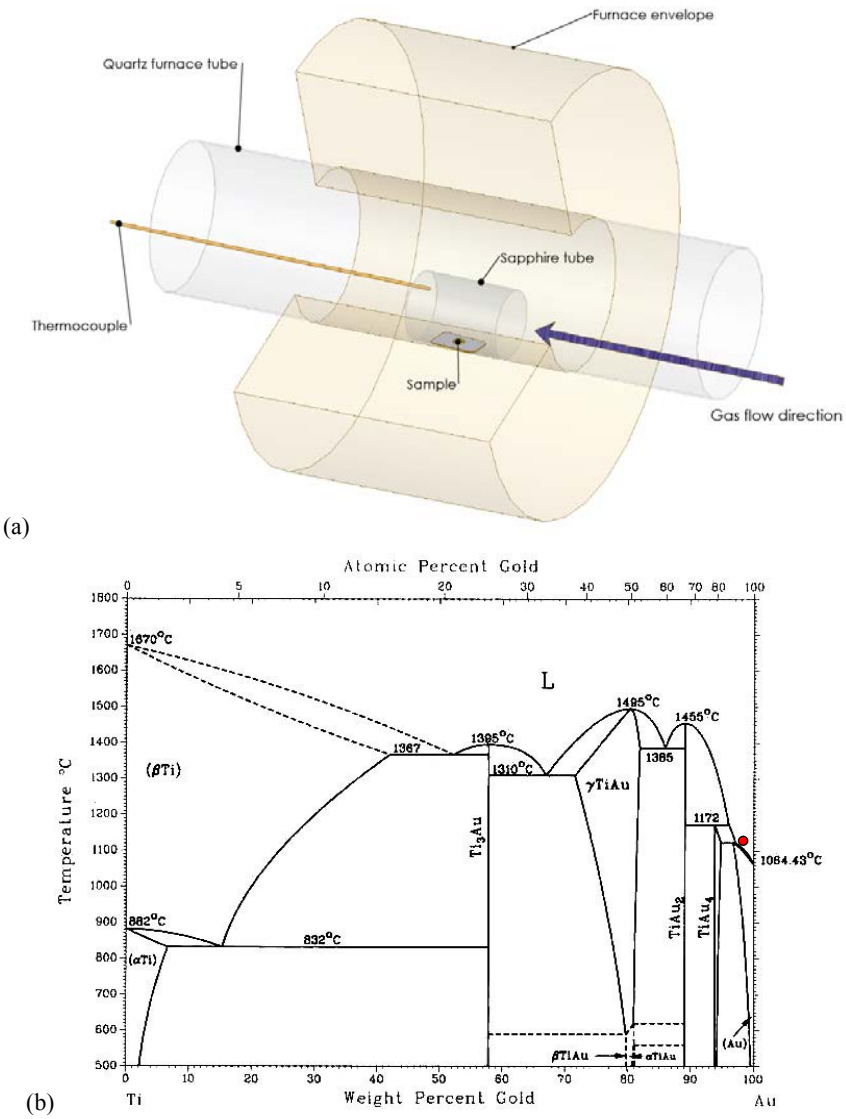

Figure 23: (a) Schematic illustration of furnace setup used for dewetting experiments. (b) Au-Ti phase diagram [129]. Working point chosen (titanium concentration and dewetting temperature) is marked in red.

The dewetting thermal profile that was chosen was as follows: heating up to 1100°C (at 10°C/min), aimed at melting of the sputtered layers. As evidenced by the Au-Ti phase diagram [129] (see Figure 23(b)), the working point chosen (film composition and dewetting temperature) ensured that the layered coating (Au+Ti) is in the liquid state during dewetting. Due to a high and finite contact angle of gold on sapphire (see

Table 2) and since molten gold is the first to be in contact with the sapphire substrate, dewetting will occur. After holding for 6 min at 1100°C, the samples were cooled down to 700°C (at 15°C/min) in order to ensure solidification of the dewetted droplets. Cooling to 700°C was followed by heating to 900°C (at 10°C/min) where the sample was annealed for 24 hr, under constant gas flow, and then cooled to R.T. According to Nichols and Mullins [27] and using equation (7), particles with radius of 500 nm will equilibrate within 20 sec at 900°C [1].

This dewetting experiment resulted in the creation of a very large number of faceted particles with diameters ranging from few hundreds of nanometers to several microns (see Figure 24).

(a) 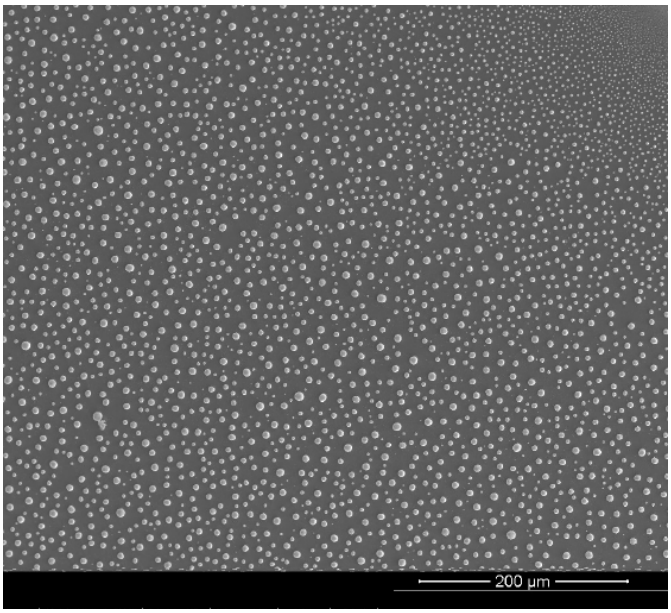

1. Surface energy of molten gold of 1400 mJ/m^2 and surface diffusivity of gold, D_s, of 5x10^{-10} m^2/sec [27] was used in equation (7).

(b) 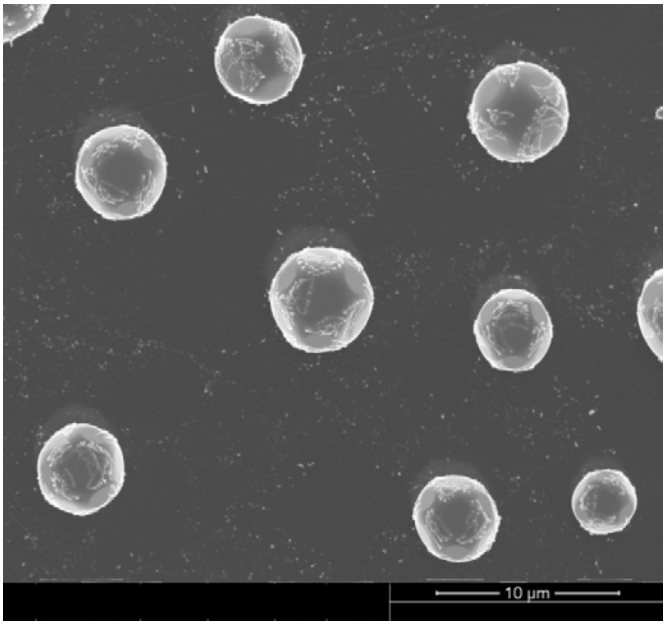

Figure 24: Secondary electron SEM micrographs of dewetted particles equilibrated on c(0001) sapphire substrate after 24 hr at 900°C, in an Ar+7% H_2 atmosphere.

4.2 Microstructural Characterization of a Commercial Active Gold Brazing Alloy

Polycrystalline 99.5% Al_2O_3 discs (supplied by 'Morgan Advanced Ceramics'), were ultrasonically cleaned with alkaline soap, boiled in hot acids (1:1 HCl:HNO_3), rinsed with de-ionized water and annealed in air at 1400°C for 1 hr.

A commercial Ti containing gold-based brazing alloy (gold ABA®, 'Wesgo Metals'), 0.25 mm in diameter and with a nominal composition of 96.4Au-3Ni-0.6Ti was ultrasonically cleaned with acetone and ethanol. The alloy was placed in between two polycrystalline Al_2O_3 discs and put through a commercial brazing thermal cycle in a vacuum furnace (vacuum level of ~$3x10^{-5}$ torr), according to the following profile:

a. Heating at 20°C/min to 40°C, holding for 10 min.
b. Heating at 15°C/min to 500°C, holding for 5 min.
c. Heating at 15°C/min to 850°C, holding for 5 min.
d. Heating at 12°C/min to 1080°C, holding for 30 min, followed by cooling to R.T.

The brazing temperature used, 1080°C, is 50°C above the liquidus temperature of the alloy, 1030°C, as declared by the manufacturer. This temperature was chosen in order to ensure melting of the alloy. After the brazing cycle, alumina specimens were cross sectioned in order to reveal the Al_2O_3-gold alloy interface.

The same procedure was repeated using sapphire substrates of 99.99% purity (supplied by 'Gavish Industrial Technologies and Materials LTD'), with basal c-plane (0001) orientation.

4.3 Characterization Methods

Characterization of the dewetted particles was carried out using different microscopic and spectroscopic methods. The morphology and shape of the dewetted particles were examined by scanning electron microscopy (SEM) and high resolution SEM (HRSEM). SEM examination was conducted using an FEI E-SEM Quanta 200 microscope, using varying accelerating voltages (5-20 kV) and a working distance of 10 mm. HRSEM was conducted on a FEI Strata 400S Dual Beam FIB equipped with a field emission gun (FEG-SEM). An accelerating voltage of 5 kV and a working distance of 5 mm were used. Particle orientation on the sapphire substrate was examined by x-ray diffraction (XRD), using a conventional x-ray diffractometer (Philips X'pert goniometer) with CuKα radiation operated at 40 kV (40mA). A θ-2θ scan was conducted from 35° to 145°, with a step size of 0.04° and an exposure time of 8 sec for each step.

Microscopic examination of the metal-ceramic interface at high magnifications was carried out using transmission electron microscopy (TEM). Confirmation of the sputtered layer thickness was carried out in a FEI Tecnai G^2 T20 S-Twin TEM equipped with a LaB_6 electron source, an FEI Supertwin objective lens and energy dispersive spectroscopy (EDS) detector, operated at 200 kV. High resolution images of the metal-ceramic interface were acquired in a FEI Titan 80-300 kV S/TEM aberration corrected TEM with a resolution of 0.07 nm, operated at 300 kV.

Electron diffraction (ED) was conducted both on the FEI Tecnai G^2 T20 S-Twin TEM and the FEI Titan 80-300 KeV S/TEM aberration corrected TEM. ED was used to determine the gold-sapphire orientation relationship and for phase identification.

Elemental characterization was carried out using electron and wavelength dispersive spectroscopy (EDS and WDS, respectively).

4.3.1 TEM Sample Preparation

Cross section TEM samples for the examination of the gold-sapphire interface were prepared in the FEI Strata 400S Dual Beam Focused Ion Beam (FIB), equipped with a FEG electron source for high resolution imaging, a high angle annular dark field (HAADF) scanning transmission electron microscope (STEM) detector and a nano manipulator (Omniprobe, AutoProbe 2000). The microscope is equipped with a conventional FEG-SEM column and a Ga^+ ion column. The two columns converge at a tilt angle of 52°, and the microscope stage can be tilted accordingly. Using the ion column for patterning, milling and polishing, the sample can be viewed simultaneously using the electron column.

Dedicated TEM samples for interface observation were prepared in the FIB using the 'lift-out' technique [17,130,131].

Specific metal-ceramic interface located under equilibrated particles can not be observed using conventional TEM sample preparation techniques. The 'lift-out' technique used in the FIB allows for the preparation of site-specific TEM specimens, although special care has to be taken in the final preparation and polishing stages if one wishes to obtain high resolution and lattice images in the TEM.

The 'lift-out' technique was used in this work in order to prepare TEM sample of the gold-sapphire interface from both the dewetted sample and the gold ABA®-sapphire brazed sample. Initial lamella thickness was ~0.2-0.3 μm. Further low voltage polishing (2-5 kV) was used to thin the lamella to less than 100 nm.

5. Results

5.1 Dewetting and Equilibration Experiments (Au-Ti-Sapphire System)

5.1.1 Particle Shape and Morphology

The first dewetting experiment resulted in the formation of a large number of particles with diameters ranging from hundreds of nanometers to a few microns (Figure 24). Facets can be clearly seen on all particles. According to Nichols and Mullins [27] (equation (7)), the equilibration time used at the first dewetting experiment (24 hr at 900°C) was sufficient for equilibrating particles having diameters of up to 8 μm (using T=1173K and $\gamma_{Au}^{(111)}$=1.4 J/m^2 [17]), implying that this is the upper size limit for particles chosen for cross sectioning for TEM observation. The largest particles observed were not bigger than 10 μm in diameter.

Further examination of the dewetted sample reveals that the larger particles exhibit some unexpected structures on the free surface (Figure 25).

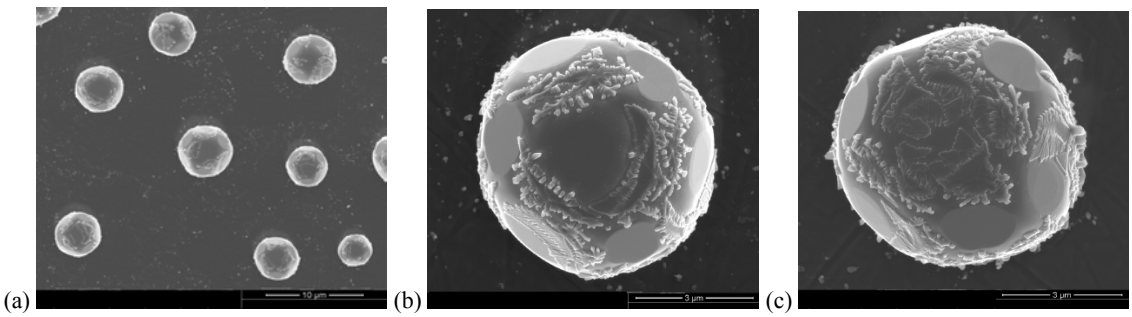

Figure 25: (a) Secondary electron (SE) SEM micrographs of dewetted particles on c(0001) sapphire, exhibiting unexpected structure growth on top of the surface. Particles were equilibrated for 24 hr at 900°C. (b), (c) High resolution SE-SEM micrograph showing structure growth on curved surfaces and on clearly visible facets.

The unexpected structures seen on the particles' surface were mostly on the curved surfaces connecting vicinal facets (Figure 25.b), although there was a small number of particles on which it has grown across facets (Figure 25.c).

In order to detect the preferred orientation formed between the gold and the sapphire, and different/new phases, x-ray diffraction (XRD) was taken from the

dewetted sample, using conventional x-ray diffractometer (Philips X'pert goniometer). CuKα radiation was used at 40 mA and 40 kV. 2θ scans were obtained from 35° to 145°, with a step size of 0.04° and an exposure time of 8 sec for each step.

The XRD results reveal a number of reflections besides the ones for gold and sapphire (see Figure 26).

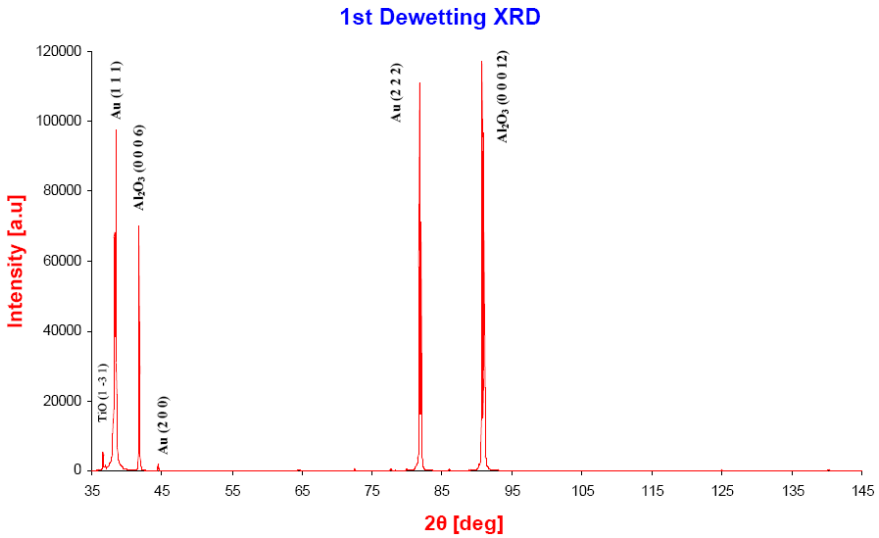

Figure 26: X-ray diffraction 2θ scan (intensity Vs. 2θ) using CuKα radiation (35°<2θ<145°) taken from the dewetted sample (24 hr at 900°C).

Gold reflections observed according to their intensity, from the highest to the lowest are (111), (200), (311), (220), (331), (422) and (420). The (111) reflection has an intensity three orders of magnitude higher than the next reflection. According to these results, Au(111) seems to be the most preferred orientation of the gold particles on sapphire. Besides gold and sapphire reflections, reflections from different titanium oxides, such as TiO, TiO_2 (brookite and rutile structures) and Ti_3O_5 and Ti_2O_3 were also observed.

5.1.2 SEM and EDS Characterization

SEM characterization of the structures grown on the particles' surface, resembling a eutectic microstructure, combined with EDS scans revealed the presence of Si on the surface. As can be seen from backscattered electron SEM micrographs, no new phase could be detected on the surface (Figure 27). One should keep in mind that these results do not imply that there is no new phase below the surface.

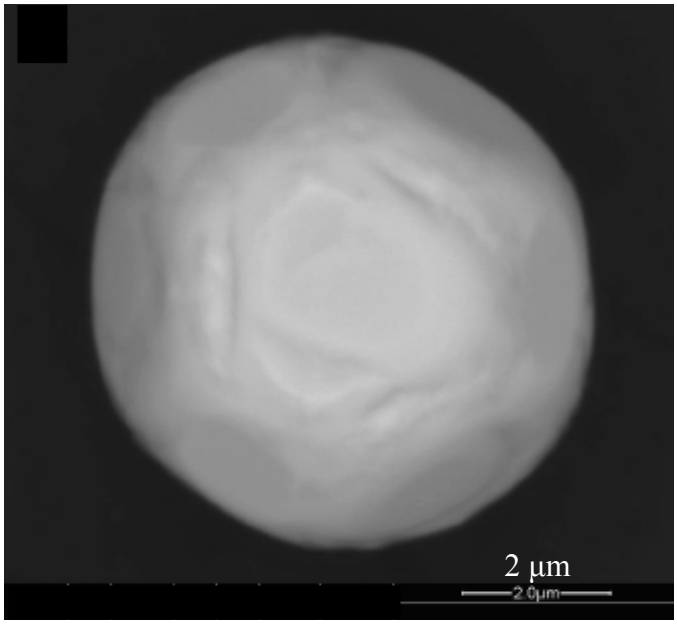

Figure 27: Backscattered electron SEM micrograph of particle equilibrated on c(0001) sapphire for 24 hr at 900°C. No phase contrast is visible across the surface of the particle.

EDS scans indicate that Si is present in these structures at the surface, but not on the Au free surface (see Figure 28).

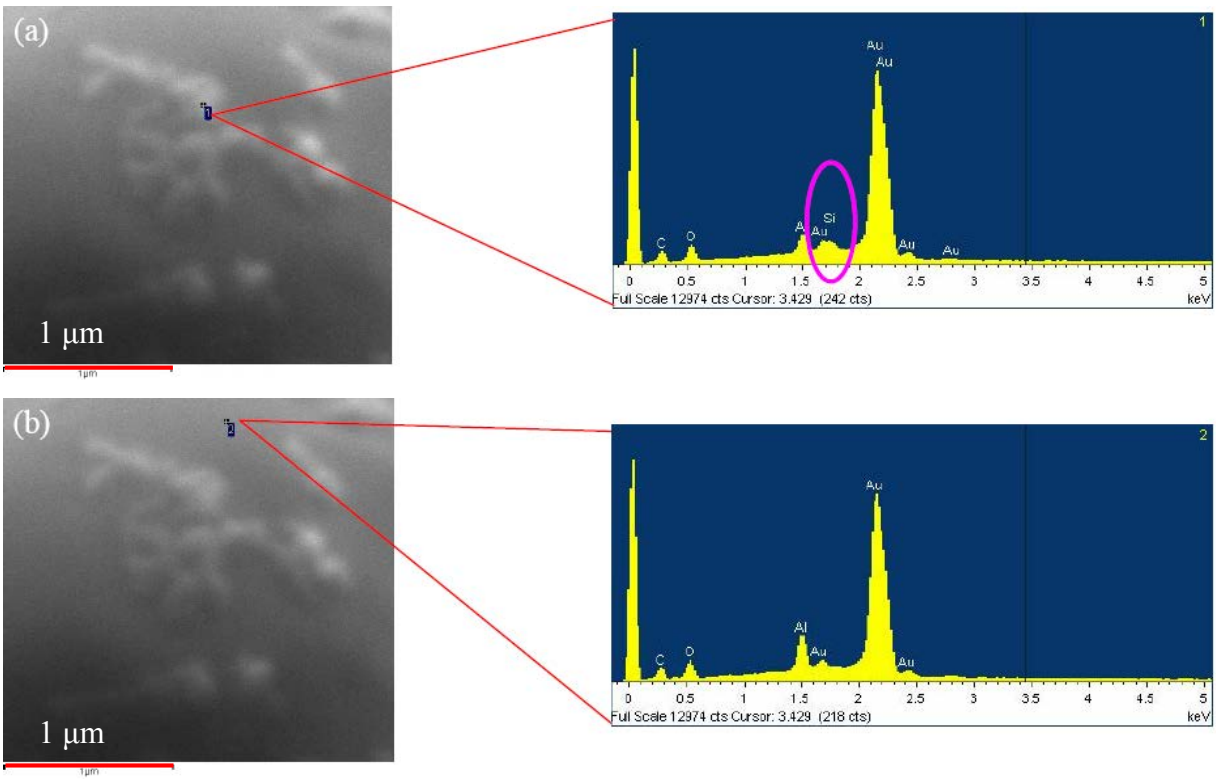

Figure 28: (a) Secondary electron SEM micrographs of the eutectic microstructure that formed on the equilibrated particle surface (900°C for 24 hr on c(0001) sapphire), combined with EDS scans showing the presence of Si. (b) No Si is detected on the Au free particle surface.

The EDS scans were acquired at an accelerating voltage of 20 kV. A qualitative estimation of the penetration depth would yield a value of few hundreds of nanometers. At these working conditions, the Si concentration detected was ~10 at.%. Si was found on other particles, again with no Si detected on the free surface near these structures. Lowering the accelerating voltage down to 10 kV and 5 kV (again, estimating a qualitative value of ~100 nanometers and a few tens of nanometers respectively for the penetration depths), reveals increasing Si concentrations of up to ~25 at.% and even 50 at.% (detected at 5kV). These results indicate that the surface is enriched with Si.

5.1.3 TEM Characterization

Among the particles detected and mentioned above, smaller particles, roughly 1 μm in diameter were also detected. These particles exhibited rather clean surfaces, not resembling the bigger ones and were completely faceted (see Figure 29).

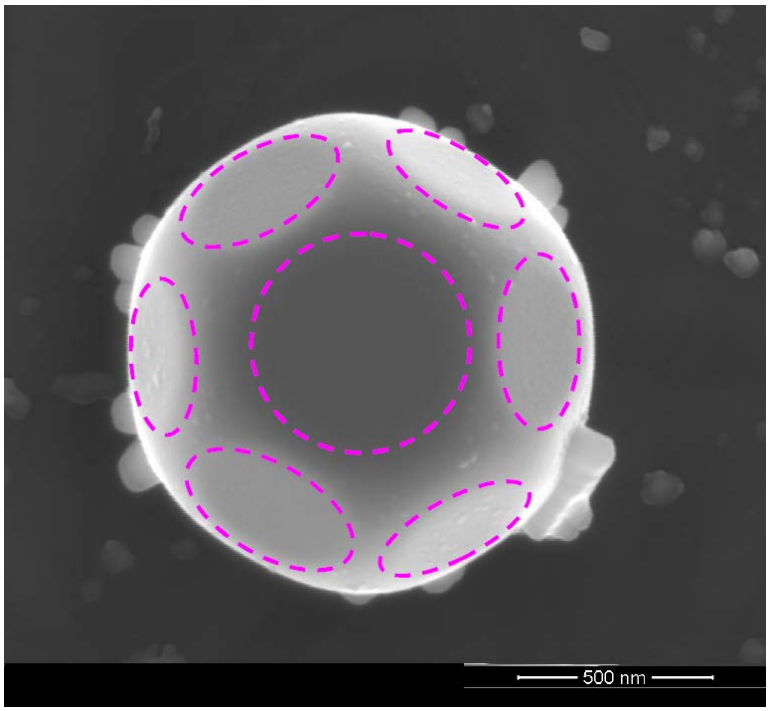

Figure 29: Secondary electrons high resolution SEM micrograph (FEI Strata 400-S FIB) of gold particle equilibrated on c(0001) sapphire at 900°C for 24 hr, exhibiting a clean surface and clearly visible faceting.

The particle shown above (1.18 μm in diameter) was chosen for cross sectioning using the 'lift-out' technique in the Dual-Beam FIB (FEI Strata 400-S FIB) in order to

examine the gold-sapphire interface. A TEM cross section sample with a thickness of ~120 nm was attained.

TEM characterization of the cross sectioned particle revealed that facets formed at the surface, but not completely. Five facets (including the interface with sapphire) were visible, but the sixth facet was not complete and straight, therefore not allowing the use of the Winterbottom analysis [47], since the equilibrium shape is not complete. Hence, thermodynamic calculations cannot be done using this particle (see Figure 30).

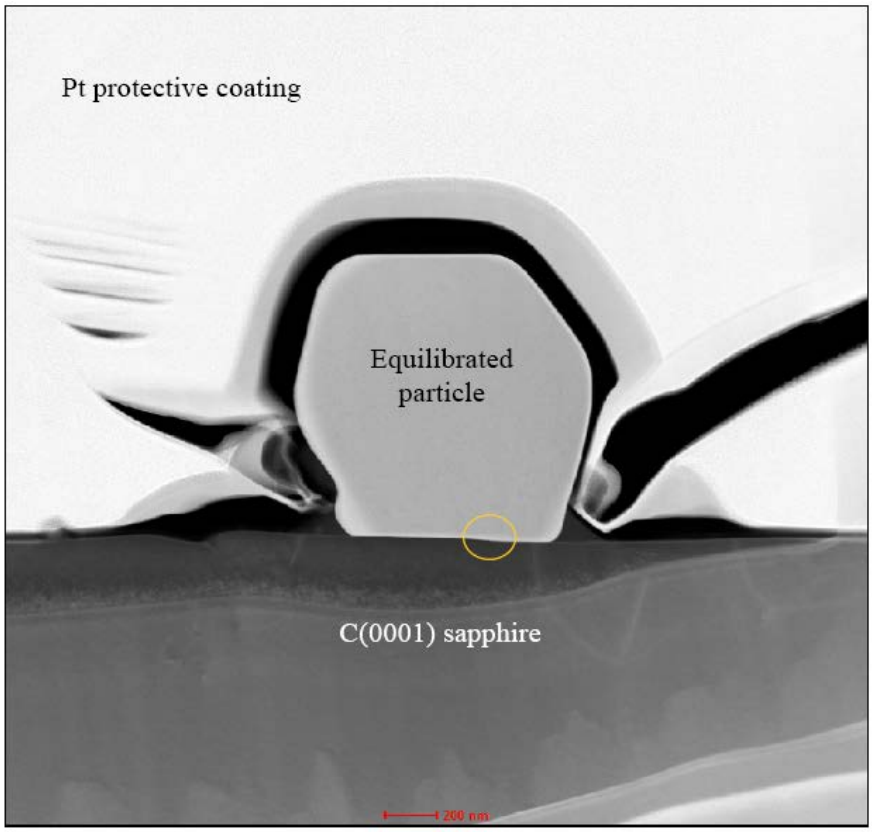

Figure 30: High Angle Annular Dark Field (HAADF) STEM micrograph (FEI Titan 80-300 kV S/TE) of the cross sectioned and equilibrated particle (24 hr at 900°C) revealing the facets that formed at the surface. A step is noticeable at the gold particle-sapphire interface (circled).

STEM characterization of the particle (Figure 30) shows that a step has formed at the gold-sapphire interface (circled). No titanium was detected in EDS scans (conducted at STEM mode) across the bulk of the particle and the different facets and the gold-sapphire interface at the working conditions chosen (accelerating voltage of 300 kV, sample thickness of ~120 nm, stage tilt of 1.59° and collection time of 400 sec).

Further EDS scans revealed high concentrations of Ti located at two nanometer sized particles residing close to the gold particle (see Figure 31).

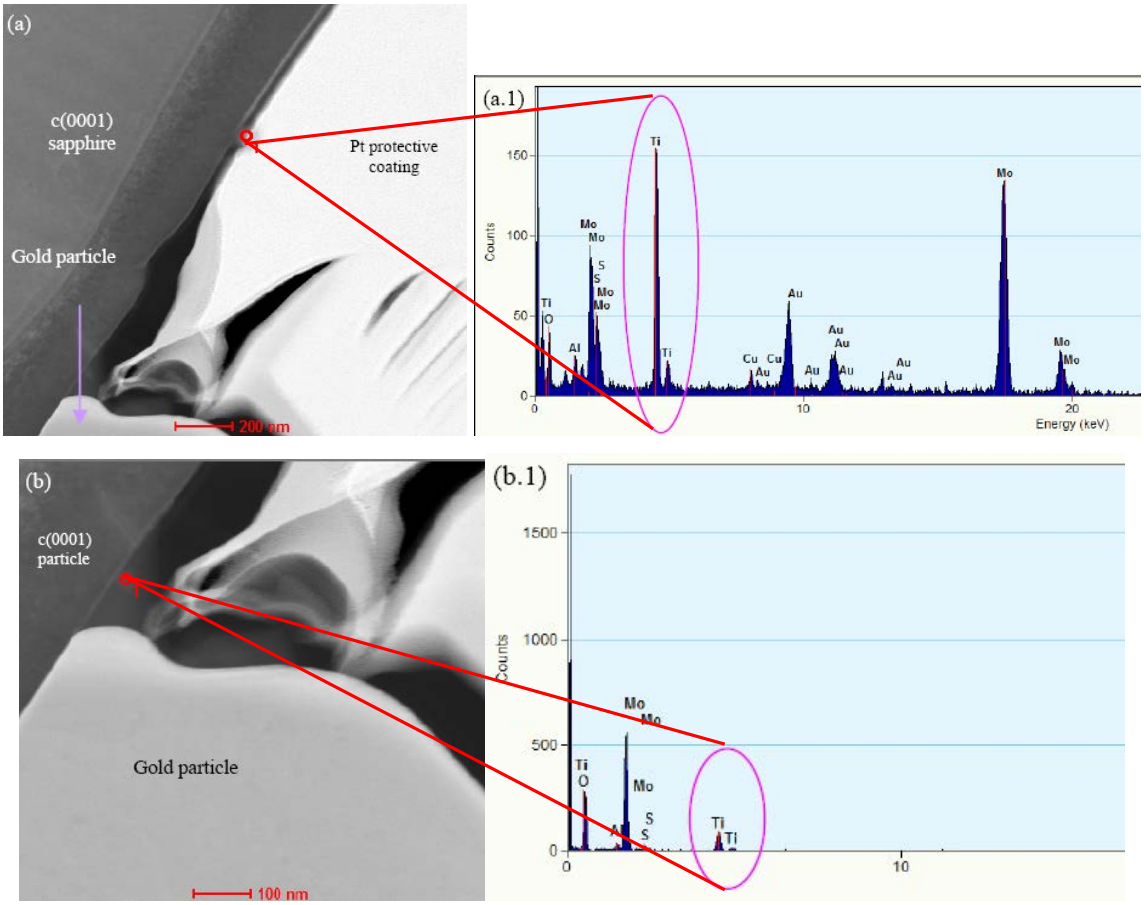

Figure 31: (a), (b) High Angle Annular Dark Field (HAADF) STEM micrographs (FEI Titan 80-300 kV S/TE) showing two nanometer sized particles rich in titanium residing next to the cross sectioned gold particle. Micrographs are shown together with the left side of the EDS spectra taken from the marked red circles, (a.1) and (b.1), respectively. Titanium concentrations are 15.2 and 5.3 at.% in (a) and (b), respectively.

The first dewetting experiment resulted in unexpected results that did not allow the analysis of the particles' surface energies, according to the Winterbottom analysis. The presence of Si on the surface of the particles and the fact that no titanium was observed at either of the interfaces of the cross sectioned particle (in the working conditions chosen) raised the possibility that the experimental system was not clean enough, especially with respect to oxygen and silicon. It was assumed that the process atmosphere contained oxygen in an amount sufficient to oxidize Ti (present in the sample) during dewetting, starting as early as during the solid state stage (disruption of the solid film), and therefore the influence of titanium on the sample could not be distinguished. In order to verify this assumption, a clean plate of commercially pure Ti was put through the same dewetting experiment. Following dewetting, the plate was examined using XRD (2θ scan in the range $20^{\circ}<2\theta<120^{\circ}$, with a step of 0.02°, Using

CuKα radiation) and compared to a second clean Ti plate that did not go through the dewetting experiment. The results are displayed in Figure 32.

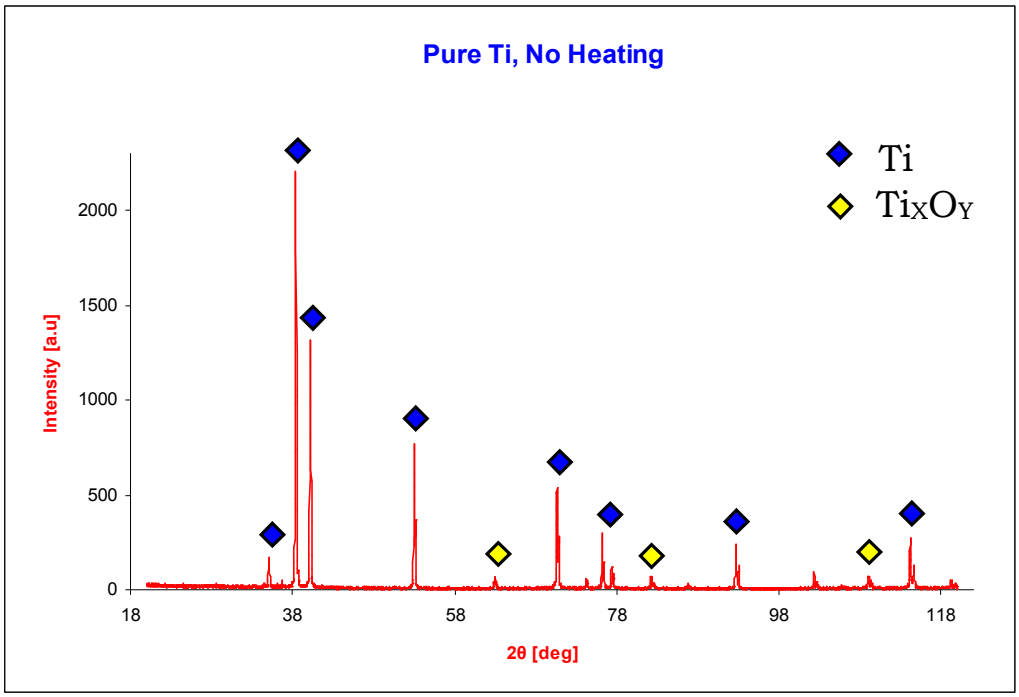

(a)

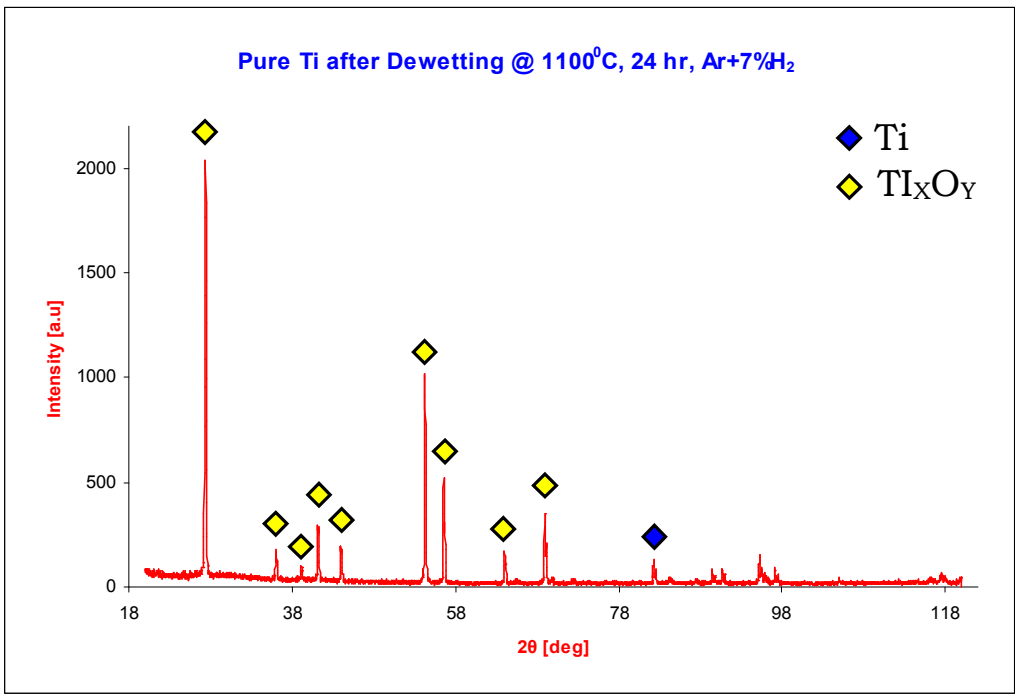

(b)

Figure 32: XRD results of: (a) pure Ti plate and (b) Ti plate that was put through the same dewetting experiment (900°C for 24 hr under constant flow of Ar+7%H_2).

The XRD results clearly indicate that the Ti plate that was put through the dewetting experiment was oxidized, whereas the clean plate (did not go through the

dewetting experiment) only displayed native Ti oxides. These results mean that there was enough oxygen present in the furnace atmosphere with a partial pressure high enough to oxidize the Ti present in the sample, thus preventing it from reaching the gold-sapphire interface.

In its initial state, titanium was entrapped between the two gold layers on the sputtered sapphire substrate. This configuration was used in order to minimize titanium exposure to the ambient atmosphere, mainly to oxygen. This way, if Ti reaches the ceramic surface, it will be through diffusion, driven by segregation. During the dewetting experiment, before reaching the film's melting temperature, the still solid film starts to break up and forms solid islands comprised mainly of gold, as can be seen in the work of Heyraud and Metois [132], who recorded the evolution of a similar system during the break up of the solid film (they actually conducted dewetting in the solid state). They observed a 3000 $\overset{0}{A}$ thick gold film coated on a graphite substrate and annealed at 1000°C.

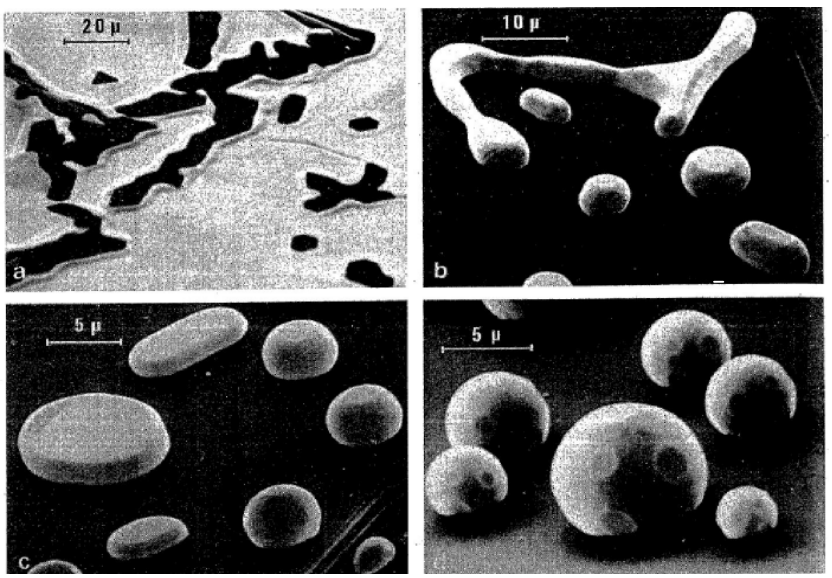

Figure 33: Evolution of a 3000 $\overset{0}{A}$ thick gold film on a graphite substrate annealed under UHV at 1000°C for: (a) 15 min, (b) 10 hr, (c) 50 hr and (d) 70 hr. Images taken from [132].

Going back to the dewetting experiment, during the stages depicted in Figure 33(a)-(b), titanium was exposed to the furnace atmosphere. At this stage, titanium would prefer to be oxidized by the residual free oxygen in the furnace atmosphere (more abundant) and only then by the oxygen originating from the sapphire surface (where it would have to segregate first and then react). This could have happened only if there

was enough oxygen in the furnace atmosphere to oxidize titanium, which is known for its strong chemical attraction to oxygen. This is corroborated by XRD (Figure 32).

Based on this, a second dewetting experiment was carried out, this time with some changes to improve the cleanliness of the process atmosphere and sample. The first change introduced was the reduction of equilibration time at 900°C, from 24 hr to 1 hr. According to Nichols and Mullins [27] (equation (7)), 1 hr is sufficient for equilibrating particles having diameters of up to ~2 μm (again, using T=1173K and $\gamma_{Au}^{(111)}$=1.4 J/m^2 [17]).

The second change introduced was the change in process gas from Ar+7% H_2 to pure Ar (99.999%). The gas was passed through an oxygen getter containing Ti and Cu flakes heated to 900°C prior to entering the furnace. This setup enabled the dewetting experiment to be carried out with a process gas having $P(O_2)$ of ~10^{-21} atm.

5.1.4 Particle Shape and Morphology - 2nd Dewetting Experiment

The second dewetting experiment carried out (after changes to the experimental system) resulted in the formation of a large number of round particles, with very small facets observed. The small facets were connected by large curved areas (see Figure 34).

(a) 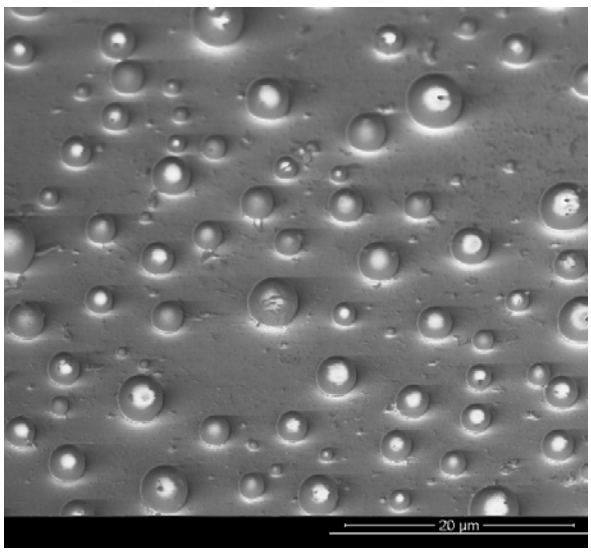

(b)

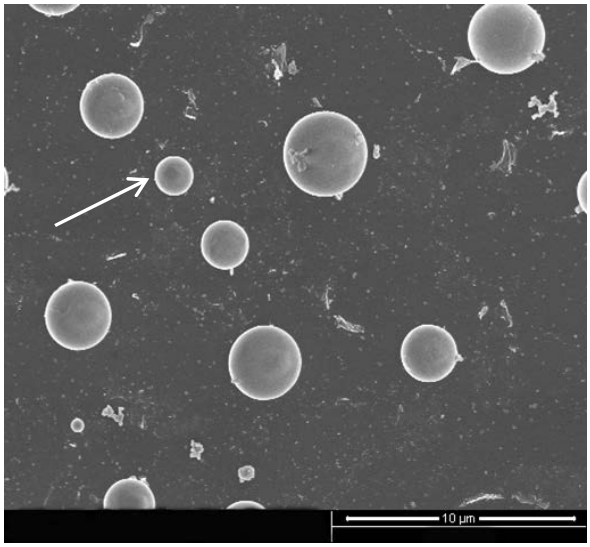

(c)

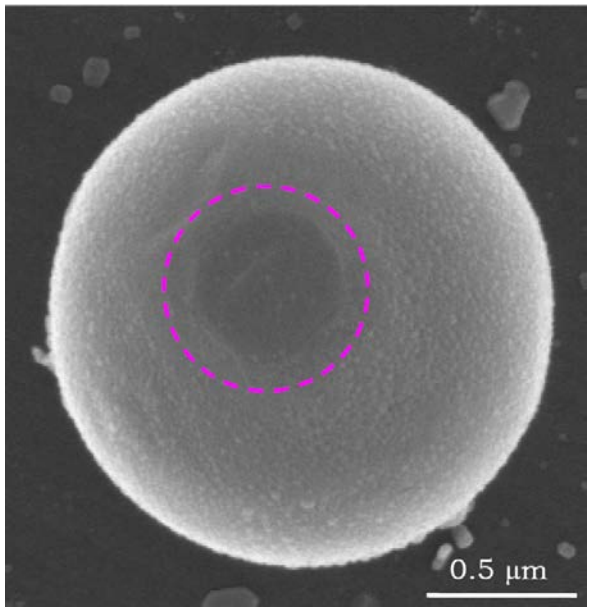

Figure 34: Secondary electron SEM micrographs of dewetted particles (2nd dewetting experiment) equilibrated on c(0001) sapphire substrate after 1 hr at 900°C, in atmosphere of pure argon (99.9995%) passed through an oxygen trap: (a) tilted at 52°, (b) and (c) taken at 0°. Slight discoloration is visible due to sample charging effects in (a) and surface texture in (c) is due to Cr deposition. Small facets are visible on the surface in (b) and (c).

In order to detect the preferred orientation of the gold particles on the sapphire, XRD was acquired from the dewetted sample, using conventional x-ray diffractometer (Philips X'pert goniometer). CuKα radiation was used at 40 mA and 40 kV. 2θ scans were obtained from 20° to 135°, with a step size of 0.04° and an exposure time of 8 sec for each step (Figure 35).

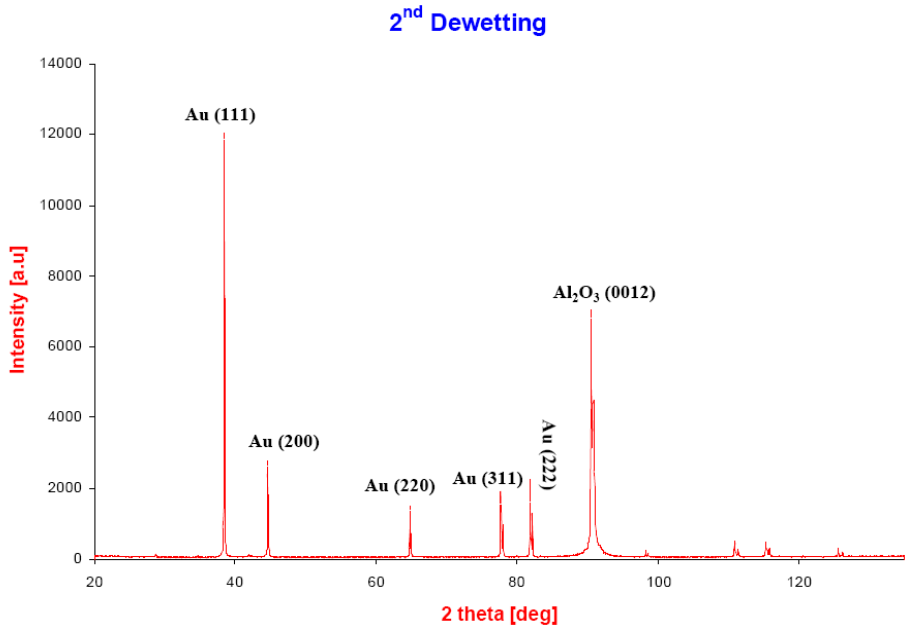

Figure 35: XRD results of the sample from 2nd dewetting experiment. Dewetting was carried out at 1100°C and equilibration at 900°C for 1 hr. Entire process was carried out under a constant flow of gettered 99.9995% Ar (yielding a $P(O_2)$ of 10^{-21} atm).

A preferred orientation of the gold particles on the c(0001) sapphire was detected. Preferred orientation is responsible for the changes that occur in the diffraction pattern. The meaning of this is that gold particles orient themselves on the sapphire surface in such a way that their interfacial energy is minimized and the (111) planes of gold are parallel to the c(0001) basal planes of sapphire. Qualitative determination of the preferred orientation is made possible by calculating the value of *P*, using the Harris method [133]:

$$P = \frac{I_{(hkl)}}{\sum I_{(hkl)}} \cdot \frac{\sum I'_{(hkl)}}{I'_{(hkl)}} \qquad (33)$$

where $I_{(hkl)}$ is the measured integrated intensity of the *(hkl)* reflection (the area under the peak), $I'_{(hkl)}$ is the measured or calculated integrated intensity from the same *(hkl)* reflection (from JCPDS card, for example). According to this, a value of $P=1$ means that this is a random polycrystal. Values of $P>1$ for some *(hkl)* reflection indicates that the reflection has a higher probability of being parallel to the substrate surface. Using this method, the values of *P* were calculated for the sample from the second dewetting experiment (Table 3).

Reflection (hkl)	2θ [deg]	Measured intensity $I_{(hkl)}$	Simulated intensity $I'_{(hkl)}$	$P = \frac{I_{(hkl)}}{\sum I_{(hkl)}} \cdot \frac{\sum I'_{(hkl)}}{I'_{(hkl)}}$
Au(111)	38.36	100.0	100	**1.41**
Au(200)	44.56	24.1	52	0.65
Au(220)	64.76	13.8	32	0.61
Au(311)	77.76	18.2	36	0.71

Table 3: Measured and integrated intensities, together with simulated intensities of gold reflections from XRD of the 2nd dewetting experiment. Simulated intensities were taken from gold's JCPDS card (#04-0784). A preferred orientation of Au(111) on c(0001) sapphire is noticeable.

Other results of the preferred orientation of pure gold particles on c(0001) sapphire substrates were reported in the literature indicate that two such orientations exist: Au(111) and Au(200) [17,59].

5.1.5 TEM Characterization - 2nd Dewetting Experiment

A representative particle (~750 nm in diameter) was chosen for cross-sectioning in order to examine the gold-sapphire interface. A TEM cross section sample was attained using the 'lift-out' technique performed at the FIB, having a thickness of ~100 nm (Figure 36).

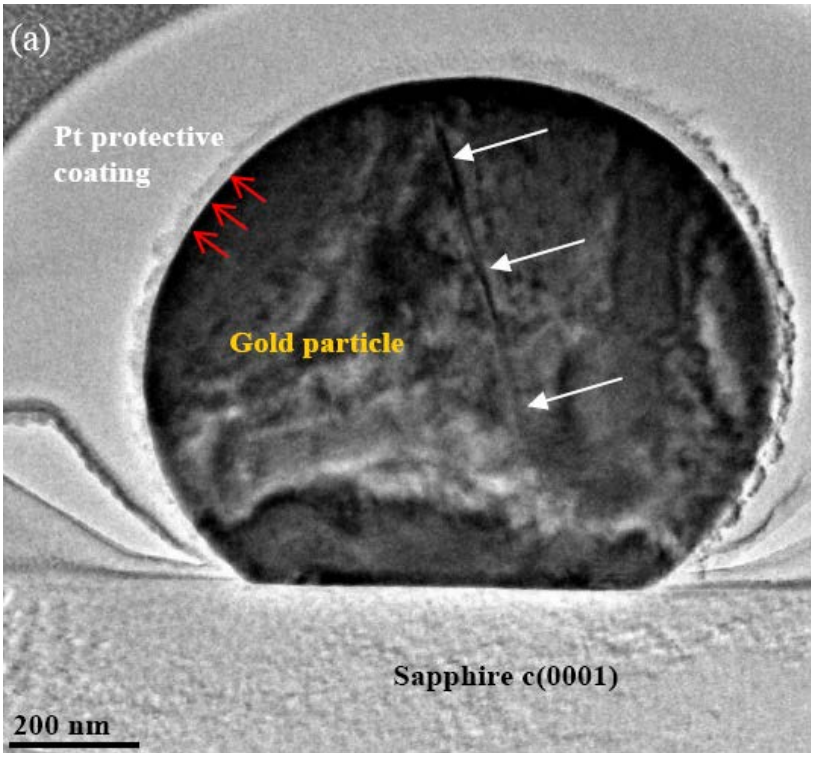

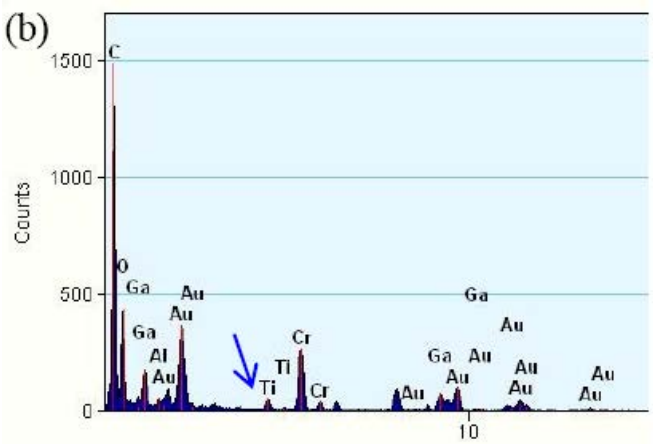

Figure 36: (a) High Angle Annular Dark Field (HAADF) TEM micrograph of a cross sectioned gold particle dewetted at 1100°C and equilibrated at 900°C for 1 hr under gettered 99.999% Ar. (b) EDS spectrum from the area marked by three red arrows in (a), indicating the local enrichment of Ti near the particle's free surface. Titanium concentration detected there was ~0.4 at.%.

According to Nichols and Mullins [27] (equation (7)), taking into account the equilibration time used and the temperature range (900-1100°C), the largest particles that can be equilibrated under these conditions are roughly 1.9 μm in diameter. Using this information it can be assumed that the particle chosen, 750 nm in diameter, is in its equilibrium form.

However, as indicated by the three white arrows in Figure 36.a, this equilibrated particle has a grain boundary, meaning it is not a single crystal. This fact does not allow the use of the Winterbottom method [47], although it is also applicable for spherical particles as well as faceted ones.

EDS scans conducted on this particle and on two other similar cross-sectioned particles revealed no presence of Ti at the metal-ceramic interface in the working conditions used (an accelerating voltage of 300 kV, sample thickness of 100-120 nm, collection time of 400 sec and stage tilt of 15.52° and 24.82° for the first particle, and 0°, 6.68° and 20.96° for the second one). In contrast to the gold-sapphire interface, Ti was detected (~0.4 at.%) near the free surface of one of the particles, as indicated by red arrows and EDS scans across this area in Figure 36, respectively. This could be a local enrichment of titanium near the surface of the particle, since segregation of titanium to the surface is not expected due to the higher surface energy of titanium (1938 mJ/m^2 [134]) compared to that of gold (1410 mJ/m^2 [134]). This local enrichment of titanium near the surface could further be encouraged by evaporation of gold, since gold has a

higher vapor pressure than titanium (~10^{-4} torr and ~$5x10^{-7}$ torr at 1100°C for gold and titanium, respectively [135]).

In light of these results, it was decided to conduct EDS scans across the free surface of the particles and the free sapphire surface, in order to identify areas with detectable amounts of Ti. EDS scans revealed the presence of Ti on the surface of some particles, as can be seen in Figure 37.

(a)

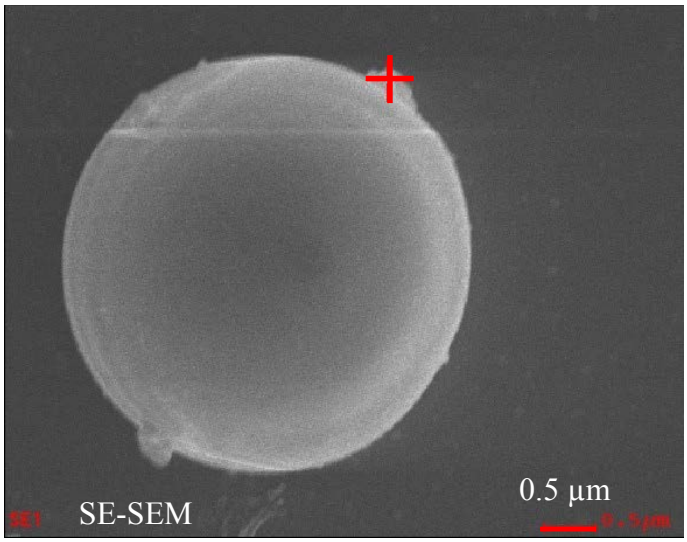

(b)

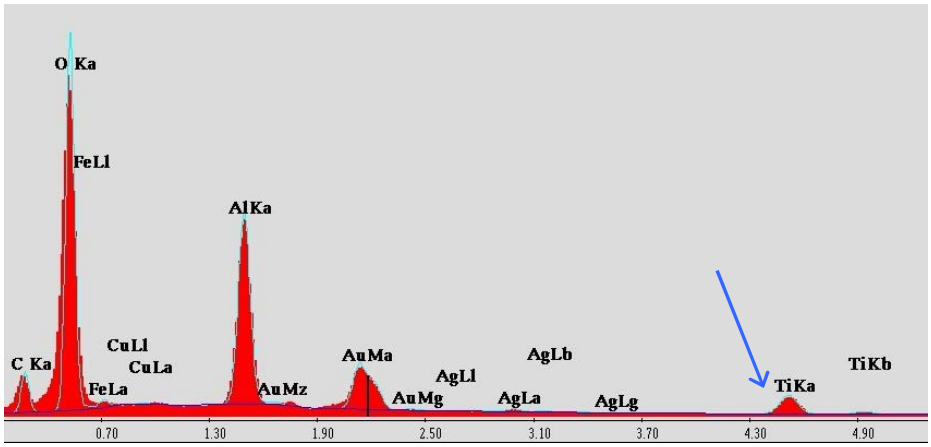

Figure 37: (a) Secondary electron SEM micrograph taken at the FIB of a particle where Ti was detected at the surface. (b) Left side of EDS spectra taken from the point marked with a red cross in (a) indicating the presence of Ti.

During dewetting, a very large number of particles form on the sapphire surface (see Figure 34). Some percentage of the particles, perhaps due to anisotropic evaporation of gold, became so enriched with titanium that it has passed its solubility limit in gold and precipitated near the surface of the particles (see Figure 37).

Since the initial amount of titanium in the sample (1.86 at. %) was very small, it may not have been sufficient to alloy each and every gold particle created during dewetting (at an amount detectable by EDS in SEM).

After Ti was detected as a precipitate at the particle's surface it was decided to extract a TEM sample from the center of it, using the 'lift-out' technique. A lamella having a thickness of ~80 nm was prepared from the center of the particle (Figure 38).

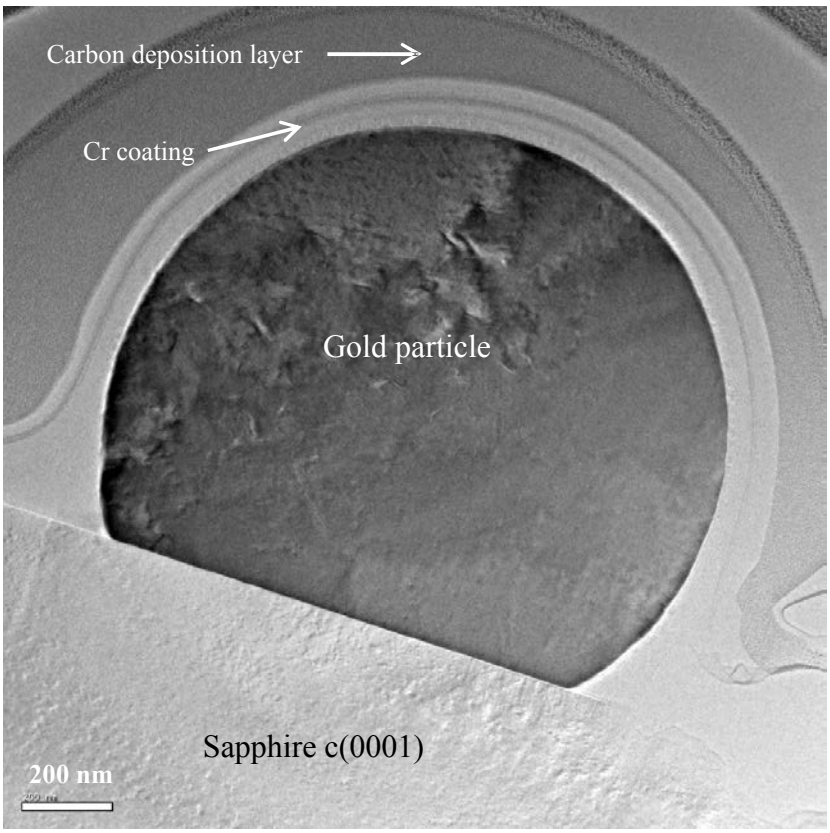

Figure 38: Aberration corrected TEM micrograph (C_S=-4.6 µm) of a cross sectioned particle. Particle and substrate are coated with a thin layer of Cr followed by a carbon deposition layer for particle protection.

The contour of the particle indicates that it is rather round. It cannot be determined whether this particle contained some facets, since it may have been ruined during the preparation of the sample and the extraction of the lamella in the FIB. The solid contact angle measured is $125^{\circ}\pm2^{\circ}$. Further EDS scans conducted across the gold-sapphire interface reveal the presence of Ti (Figure 39).

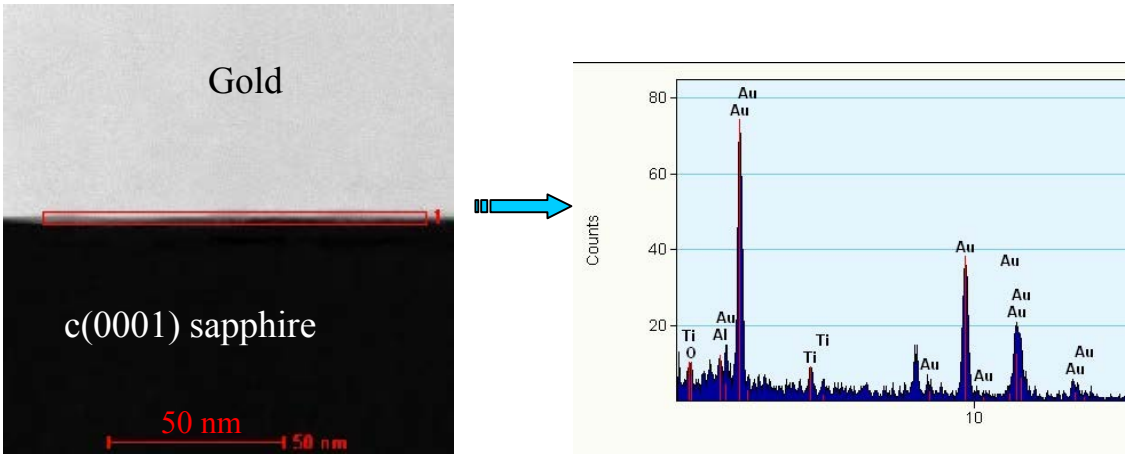

Figure 39: High Angle Annular Dark Field (HAADF) TEM micrograph of the gold-sapphire interface together with EDS spectrum, showing the presence of Ti at the interface.

The $K\alpha_1$ peak of Ti (4.51 Kev) is clearly seen above the background level. Titanium concentration was ~5 at. % (an excess of 2.2 Ti atoms/nm^2, as calculated using eq.(47), see *Appendix 1 - Detection Limit - Theory and Calculations*). Assuming that titanium acts as a substitution atom, it can replace an atom on the gold or on the sapphire interface planes. In the case where titanium replaces a gold atom on the last Au(111) plane at the interface, and based on the atomic density of the Au(111) plane (12 atoms/nm^2), then there is a 0.18 monolayer of titanium at the interface. In the case where titanium replaces an aluminum surface atom of the Al-terminated sapphire, and based on the cation density of the c(0001) sapphire surface (10 cations/nm^2), then there is a 0.22 monolayer of titanium at the interface.

Further examination of the gold-sapphire interface using high resolution aberration corrected TEM reveals a partially ordered adsorbate layer that formed at the interface (see Figure 40).

(a)

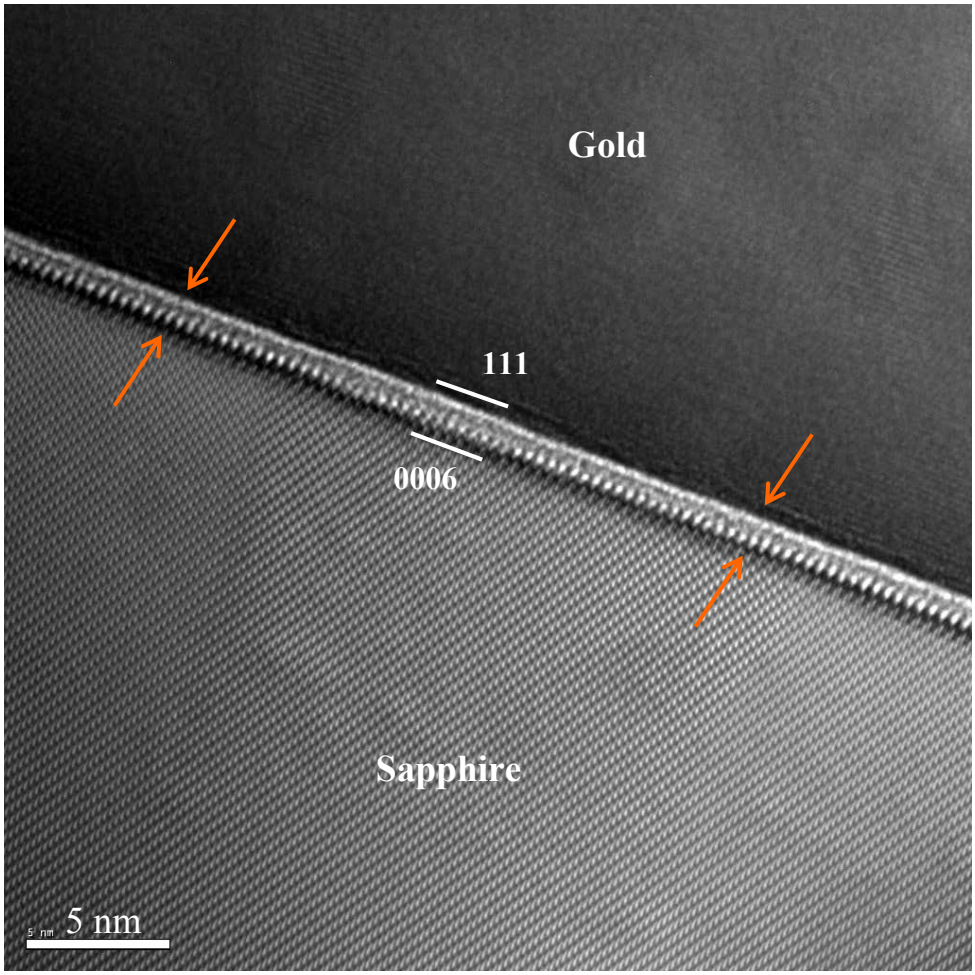

(b)

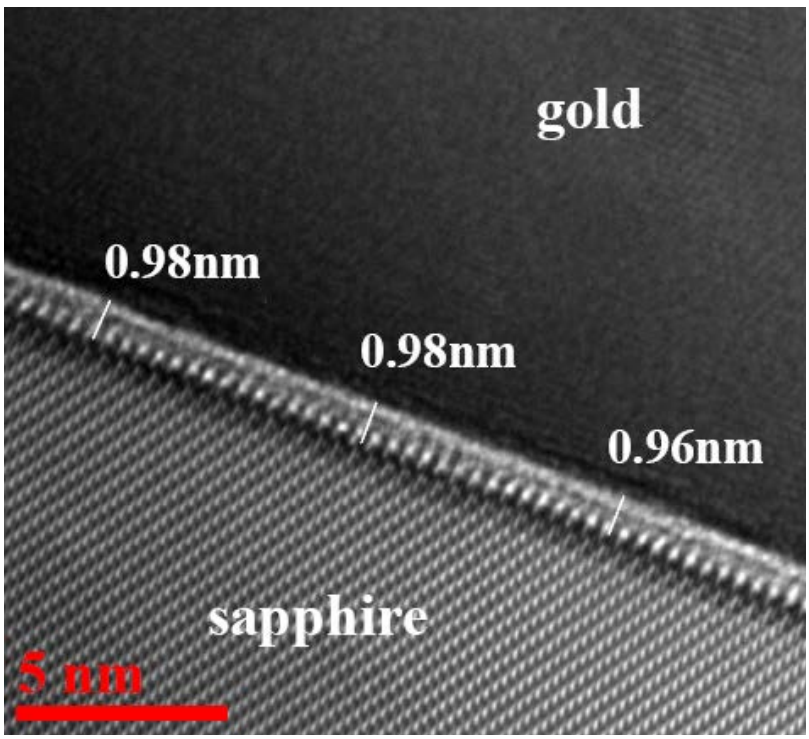

Figure 40: (a) High Resolution aberration corrected TEM (HRTEM) micrograph (C_S=-4.6 µm) of the gold-sapphire interface (2nd dewetting experiment), (b) digital magnification of (a) together with the dimensions of the partially ordered adsorbate layer.

From Figure 40 it is seen that a partially ordered structure formed at the interface, different from both sapphire and gold, having thickness of ~1 nm. A preliminary analysis aimed at determining the atomistic structure of the interface was conducted using a defocus series of 21 HRTEM micrographs from which the exit wave reconstructed image can be seen in Figure 41.

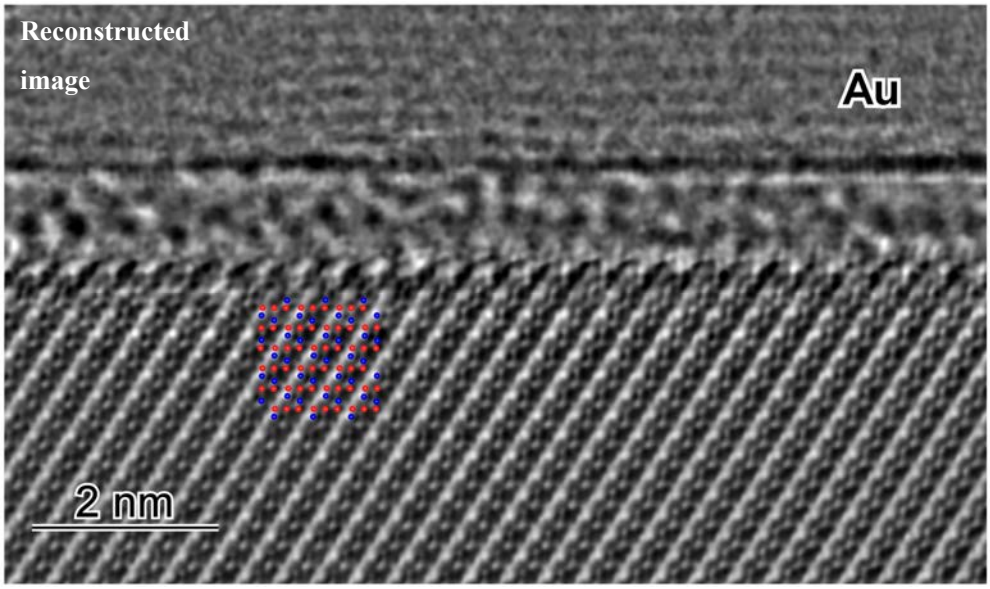

(a)

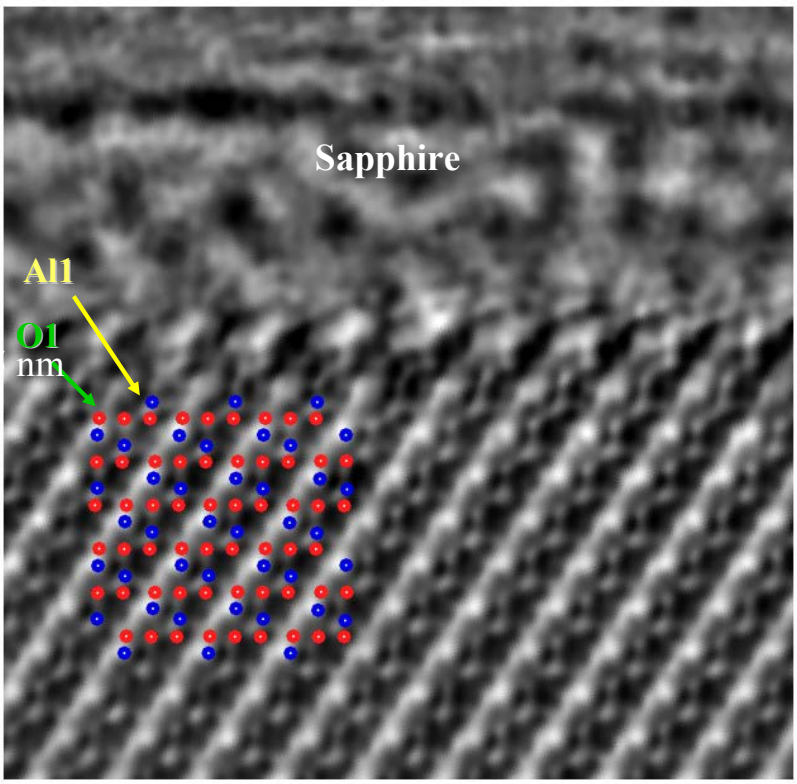

(b)

Figure 41: (a) Exit wave (phase) reconstructed from 21 aberration corrected (C_S=-4.6 µm) HRTEM micrographs of the gold-sapphire interface (2nd dewetting experiment), (b) digital magnification of (a).

As seen in Figure 41, the periodicity of the sapphire substrate changes when approaching the interface. Different contrast of atomic positions can be seen in the interfacial adsorbate layer.

Further examination of the triple junction (gold-sapphire-vapor) and the free surface of the sapphire substrate show that Ti has adsorbed there also, as shown in Figure 42.

(a)

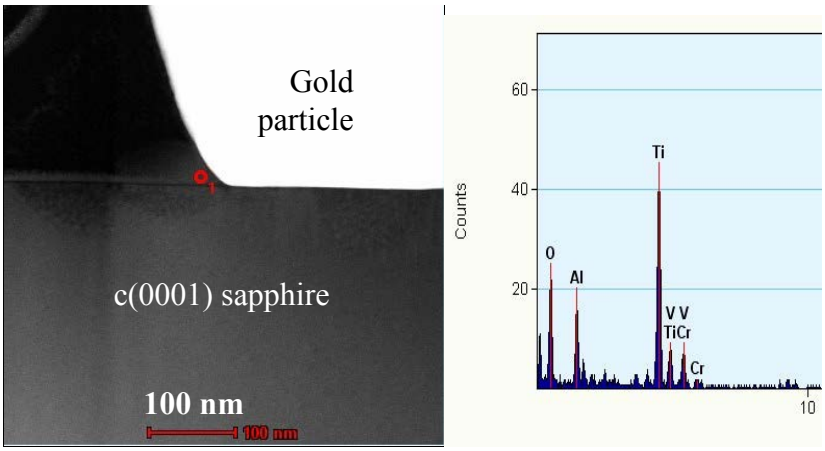

(b)

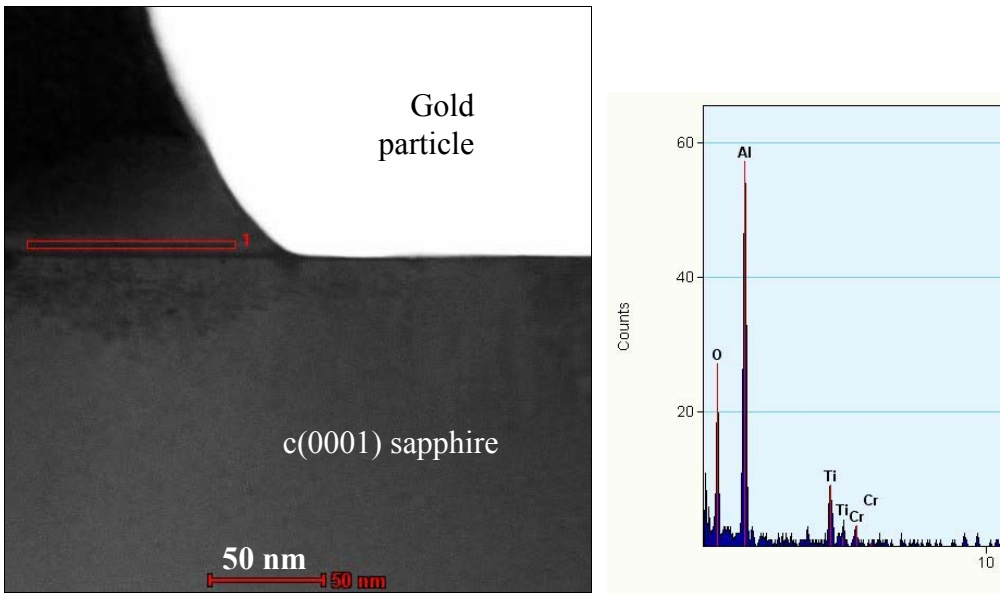

(c) 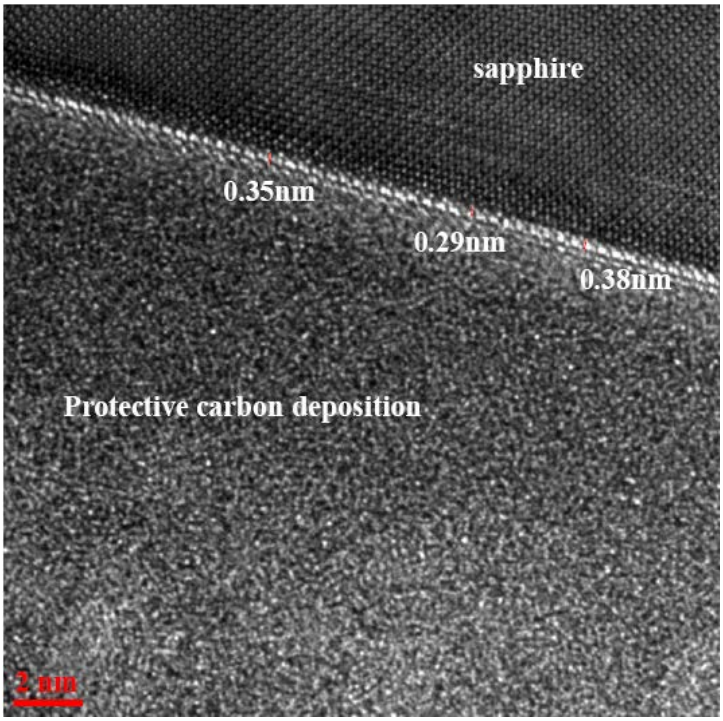

Figure 42: High Angle Annular Dark Field (HAADF) micrographs together with EDS spectrums of (a) triple point and (b) free sapphire surface indicating the presence of Ti in both places. (c) High resolution aberration corrected TEM micrograph (C_S=-3.4 µm) of the sapphire surface where Ti was detected.

Ti was detected at the triple junction and on the free sapphire surface, as indicated by the EDS spectrums in Figure 42. The titanium concentration detected was 32.7 at. % and 3.71 at.% (~4.6 Ti atoms/nm^2) in the triple junction and on the sapphire surface, respectively. This concentration of titanium at the free surface of the sapphire surface corresponds to a 0.5 monolayer, based on the cation density of an Al-terminated sapphire surface. Further examination of the triple point shows a surface layer, distinguishable from the sapphire surface (Figure 43).

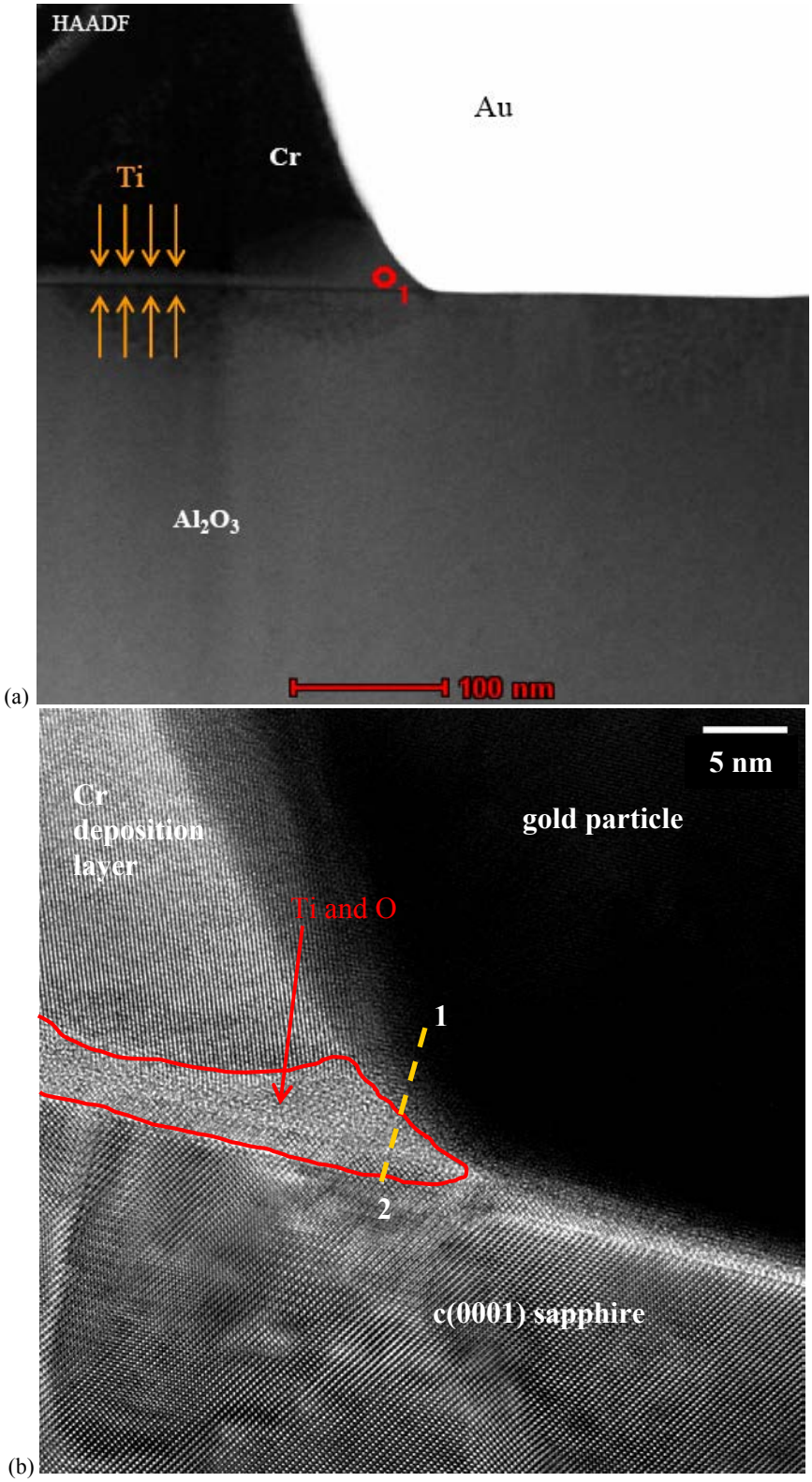

Figure 43: (a) High Angle Annular Dark Field (HAADF) TEM micrograph of the triple point of the gold particle. An adsorption layer of a Ti-containing compound on the sapphire substrate is indicated by orange arrows. (b) High Resolution aberration corrected TEM (HRTEM) micrograph (C_S=-3.4 µm) of the triple point. Cr protective layer is also visible. An area containing Ti and O peaks alone is confined by a red line.

As can be seen in Figure 43.a, an adsorption layer of Ti or a Ti-containing adsorbate is seen on the sapphire surface marked by orange arrows. High magnification images combined with EDS scans across the dashed yellow line in Figure 43.b show gold peaks in the beginning of the line (point 1), at the gold particle area. When advancing towards the sapphire substrate (point 2), the gold peaks diminishes, giving rise to Ti and O peaks alone in the area confined with the red line (see Figure 43.b). At point 2, peaks of Al and O (sapphire surface) alone are detected.

Electron diffraction patterns were taken from the gold particle and the sapphire substrate in order to determine gold-sapphire orientation relationships (Figure 44).

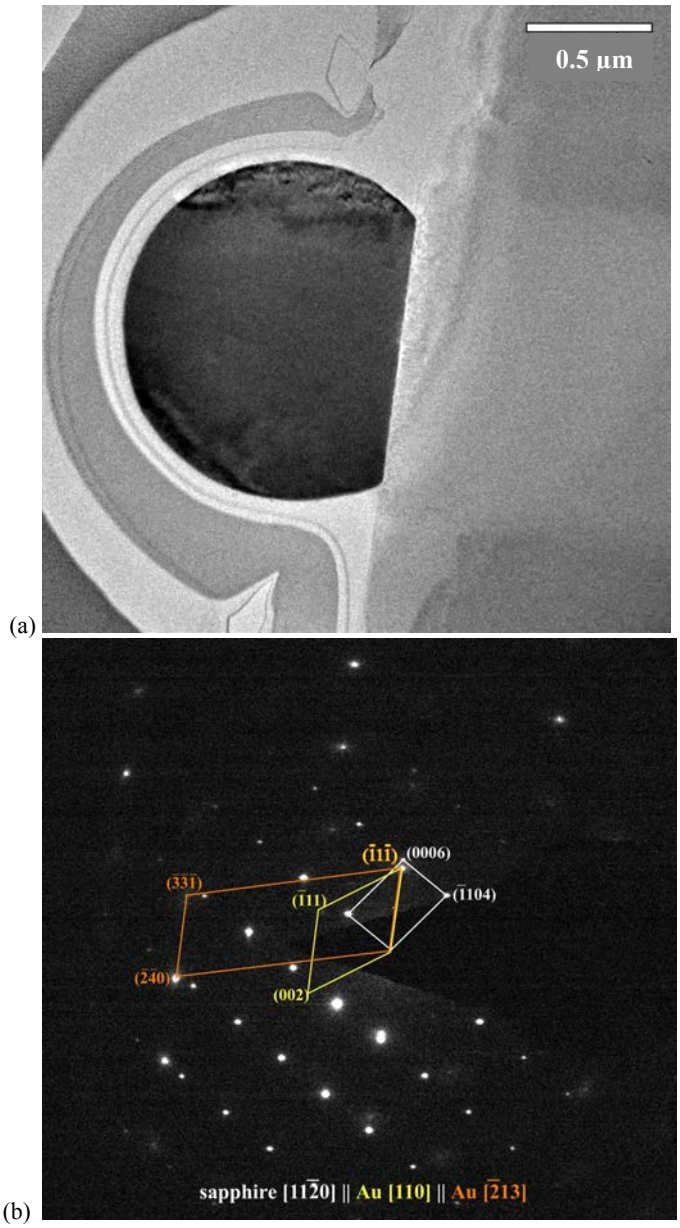

Figure 44: (a) Bright Field TEM micrograph and (b) selected area diffraction pattern for the equilibrated gold particle and the sapphire substrate. The diffraction pattern is oriented the same as the BF micrograph.

As was shown earlier for the entire sample, Au(111) is the preferred orientation of the gold particles on the c(0001) sapphire substrate, and now, the same is shown for a specific particle, where a low index orientation relationship can be seen, Au($\bar{1}1\bar{1}$) || sapphire (0006).

5.2 Commercial Active Brazing Alloy - Gold ABA®

Cross sectioned samples were prepared and examined using SEM, EDS and TEM. The following results relate to the sample where c-plane sapphire was used as a substrate.

5.2.1 SEM and EDS Characterization of the Gold-Sapphire Interface

A cross sectioned sample of gold-ABA® alloy, sandwiched between two c(0001) sapphire discs and vacuum brazed at 1080°C for 30 min, was examined using conventional SEM combined with EDS scans (Figure 45).

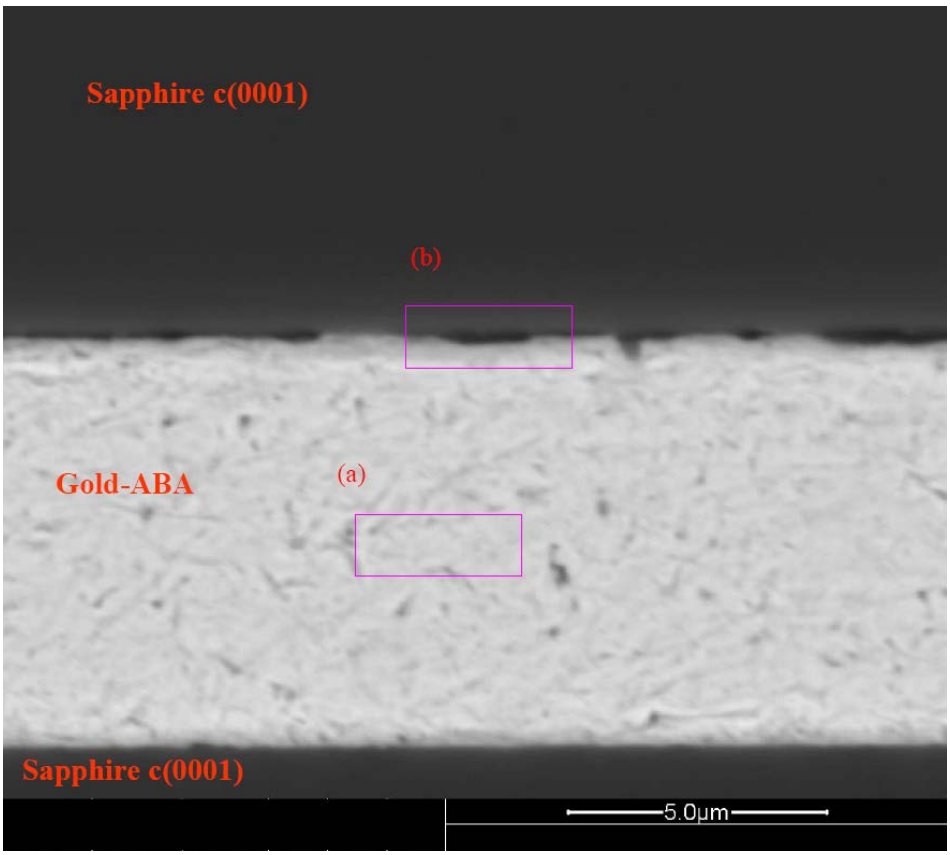

(a)

(b)

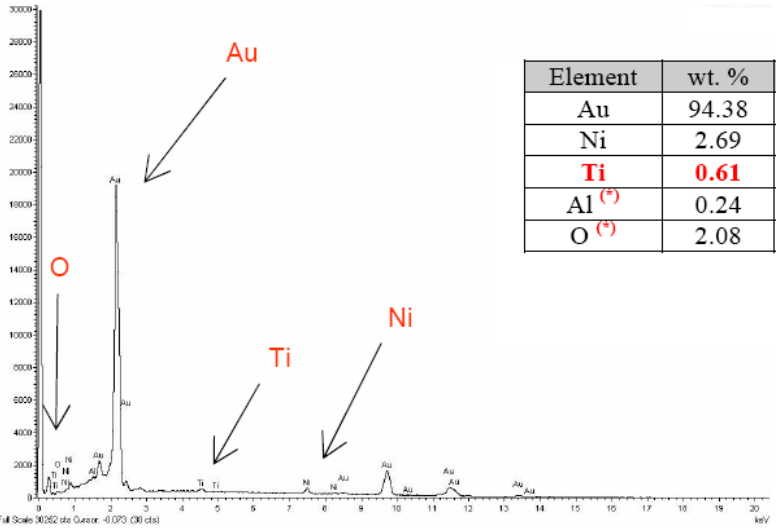

Element	wt. %	at. %
Au	94.38	70.84
Ni	2.69	6.78
Ti	**0.61**	**1.88**
Al (*)	0.24	1.31
O (*)	2.08	19.19

(c)

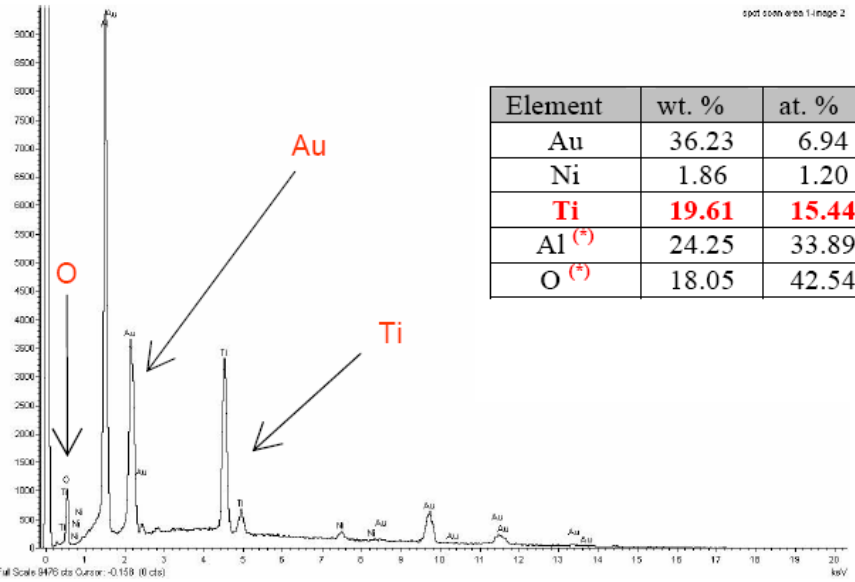

Element	wt. %	at. %
Au	36.23	6.94
Ni	1.86	1.20
Ti	**19.61**	**15.44**
Al (*)	24.25	33.89
O (*)	18.05	42.54

(d)

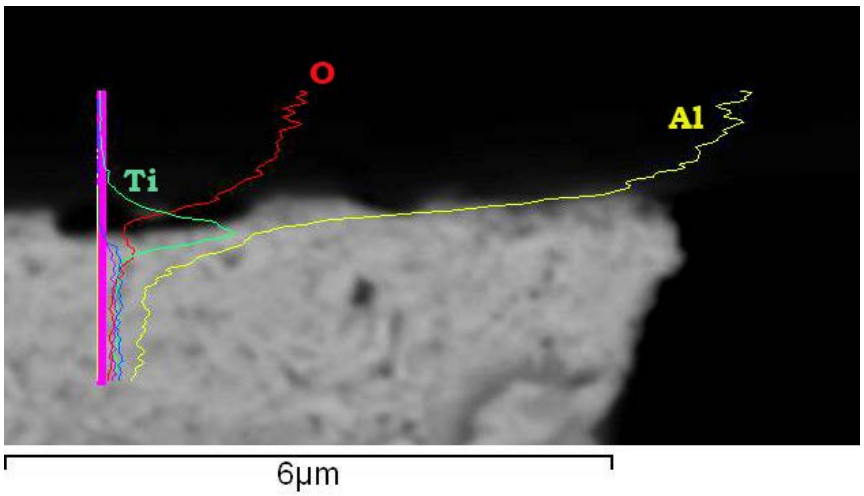

Figure 45: (a) Backscattered Electrons SEM micrograph (FEI E-SEM QUANTA 200) of a cross sectioned sample of gold-ABA® alloy, vacuum brazed between two c(0001) sapphire discs at 1080°C for 30 min, showing general structure of the interface. (b), (c) EDS spectra of the boxes marked as (a) and (b), respectively. (d) BSE SEM and EDS line scan across the interface showing Ti enrichment in black contrast areas.

The initial distance between the two sapphire discs, as put through the brazing experiment, was the brazing alloy wire diameter (0.25 mm). After the brazing experiment, as can be seen in Figure 45.a, the average thickness of the interface between the two sapphire discs has decreased down to ~7 μm, indicating that the alloy spread across the sapphire surface. The reaction phase seen in Figure 45 as the dark areas at the gold-sapphire interface is clearly not continuous.

EDS scans across the bulk of the gold-based filler metal in Figure 45.b gives the typical bulk composition of the alloy. When conducting the same EDS scans across the darker areas shown in the BSE micrograph in Figure 45.a and the line scan depicted in **Figure 45**.c, a sharp increase in the concentration of Ti is observed, indicating that the interface is enriched with Ti or Ti-containing compounds. In both EDS spectrums shown in Figure 45, Al and O peaks are also present, since substrate atoms are present in the interaction volume of the electron beam with the sample.

5.2.2 TEM Characterization of the Gold-Sapphire Interface

In order to investigate the nature of the metal-ceramic interface that has formed, TEM was required. This was achieved by producing a TEM sample using the "lift-out" technique. The thin electron transparent lamella was cut from a cross sectioned SEM sample of the gold-ABA® alloy, sandwiched between two c(0001) sapphire discs.

Using this technique, the observation of the unique metal-ceramic interface created is made possible using TEM. Indeed, as indicated earlier, a non-continuous reaction interface layer is visible. It is made of isolated grains of a Ti-containing reaction product. Measurements indicate that these grains are not larger than a few hundreds of nanometers. The thickness of the reaction layer itself is in some cases as small as 35 nanometers (Figure 46).

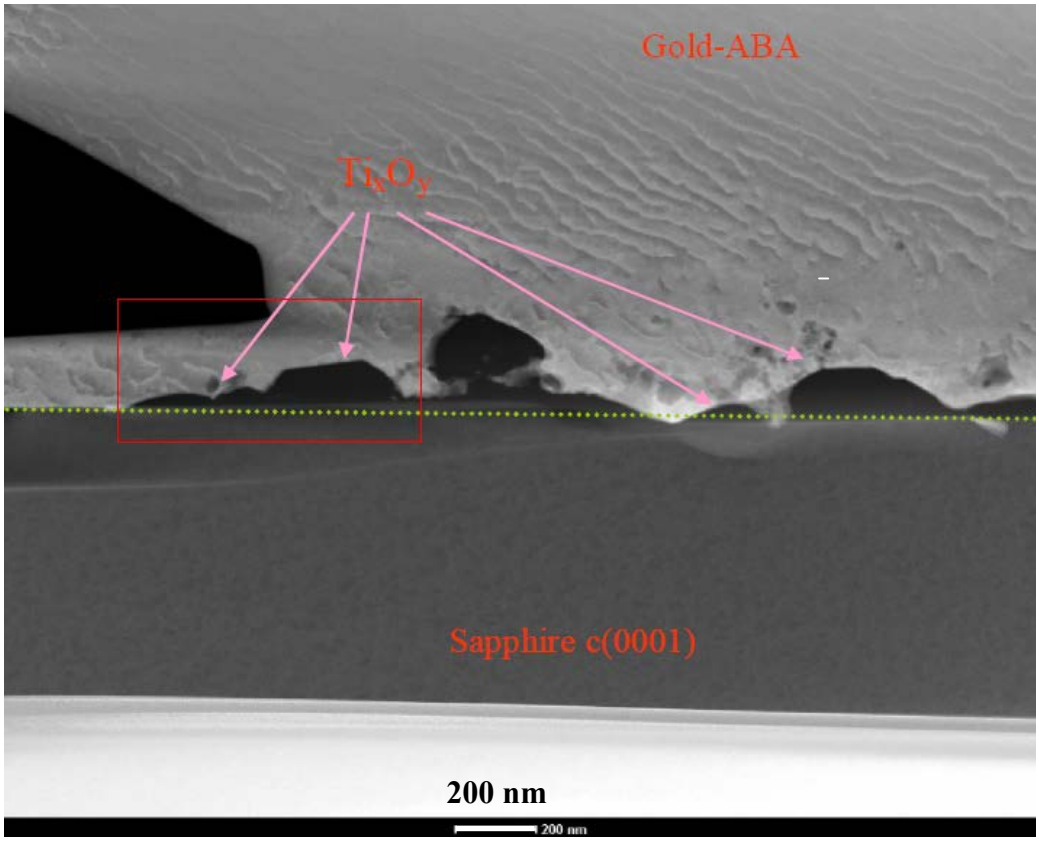

Figure 46: High angle annular dark filed (HAADF) STEM micrograph of the metal-ceramic interface between gold-ABA® and c(0001) sapphire. Non-continuous and isolated 'islands' of reaction products (black) are visible. Interface is indicated by broken green line.

The interface seen in Figure 46 is representative of the interfaces formed in this system, as was observed in other areas in this TEM sample. Higher magnifications, achieved using high resolution STEM, show the general contour of the largest grain in the red frame in Figure 46. When combined with EDS scans, it is seen that this grain is a form of titanium oxide, containing only titanium and oxygen (Figure 47).

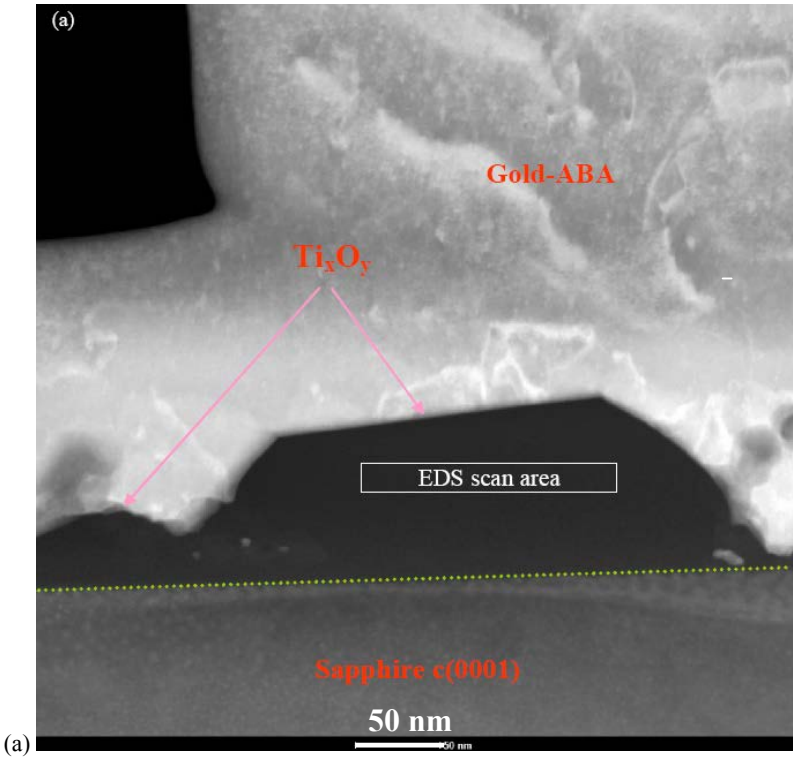

(a)

(b)

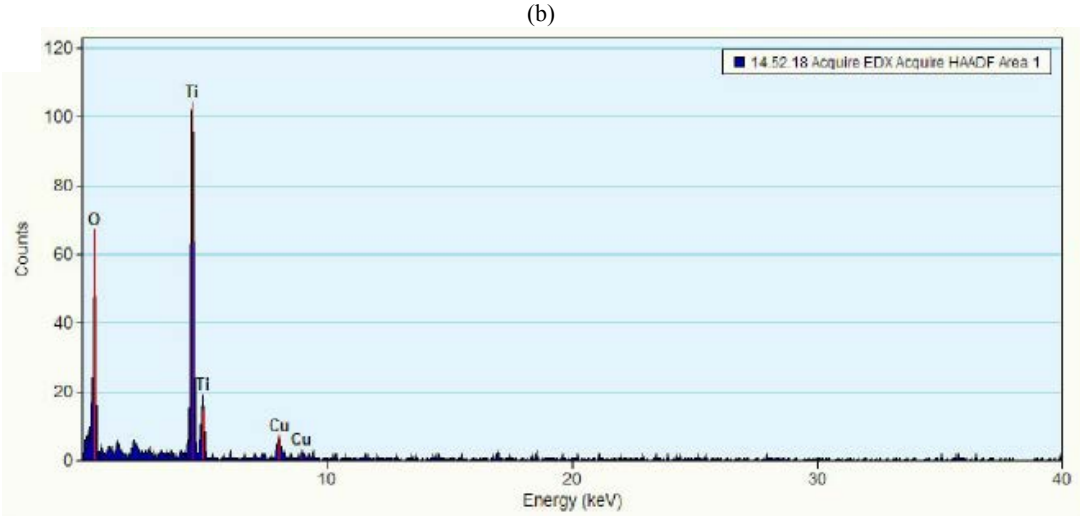

Figure 47: (a) High Resolution STEM micrograph of the reaction product grain shown in the red box in Figure 46 and (b) EDS spectra of a scan across that grain marked in (a) showing the presence of Ti and O alone, indicating that this is a grain of titanium oxide (Ti_xO_y), probably TiO_2 or Ti_3O_5.

(*) Cu peak originates from TEM specimen holder.

In order to determine the nature of the titanium oxide grains that have formed at the interface, higher resolution TEM images were acquired. High resolution TEM micrographs show that indeed grains of Ti-containing compounds are visible (Figure 48).

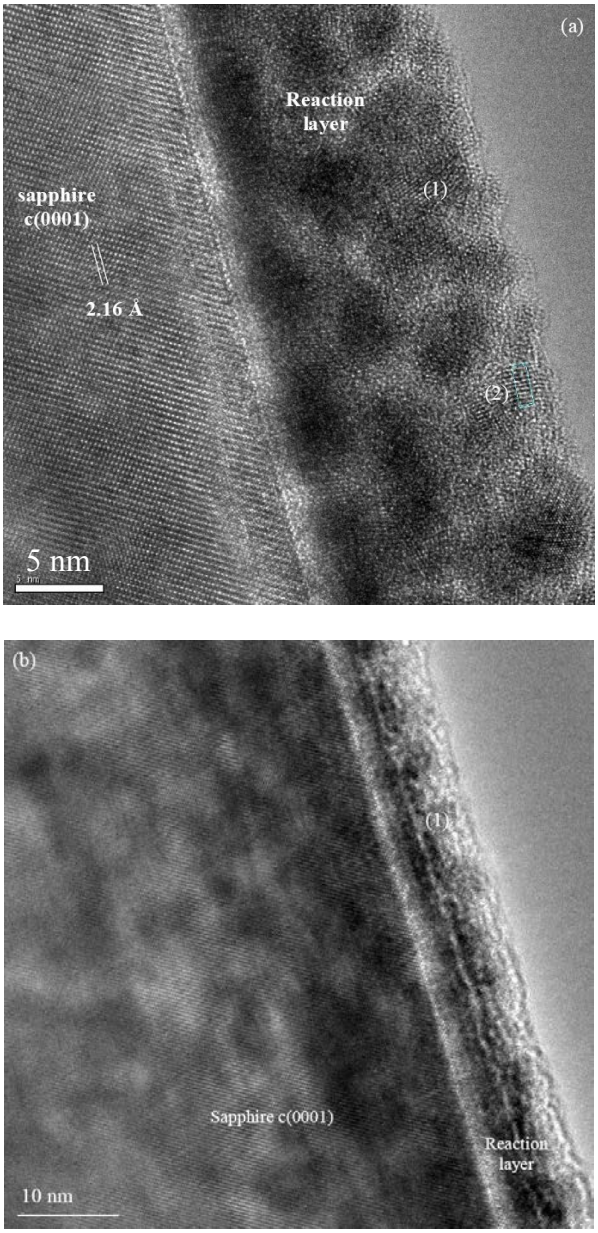

Figure 48: (a), (b): High resolution transmission electron microscopy (HRTEM) images of different titanium oxides that formed at the gold ABA®-sapphire c(0001) interface. Ordered grains are visible.

As shown in the high resolution TEM images above, various titanium oxides have formed at the metal-ceramic interface. In the same way, other titanium oxide grains along the interface were examined and characterized. Since it was not at the scope of this work, the exact nature of these oxides was not determined.

6. Discussion

6.1 Dewetting and Equilibration Experiments

6.1.1 Equilibrated Particle Shape and Morphology

The first dewetting experiment resulted in the creation of a very large number of faceted particles. The facets were relatively large, where micron sized particles had nearly micron sized facets (see Figure 24 and Figure 25). The relatively large facet size may indicate that impurities were present, and possibly have adsorbed on the free surface or segregated to interfaces or grain boundaries (that could possibly be found in the larger particles). Si contamination of the sample found in analysis (**Figure 28**) explains why large facets were observed. Surface energies of gold were reduced due to Si adsorption from the atmosphere, according to the Gibbs adsorption isotherm (eq.(2)), causing the observed increase in facet area (since they are now favored energetically). Other evidence for a decrease in the surface energy of gold due to segregation/adsorption were found in the work of Wang and Wynblatt [122], where segregation of 0.9 monolayer of Sn to gold surface (in a Au-4.0 at.% Sn dewetted sample) has decreased the surface energy of gold by 429 mJ/m^2 (at 1123K and based on the atomic density of the Au(111) surface).

WDS examination of the sputtered samples that were not dewetted showed a Si content of only a few tens of ppm's. Obviously, this is not the source of silicon in the dewetted sample since it was observed that almost all particles developed the structures mentioned above, so the source for silicon adsorption was probably the quartz tube of the furnace. Long equilibration times and hydrogen in the atmosphere (Ar+7% H_2) probably reduced SiO_2 from the furnace tube into elemental Si that was carried away by the flowing gas and adsorbed on the free surface of the gold particles.

XRD and backscattered electron SEM characterization of the surface of the particles indicate that no new phase was formed at the surface, although such phase can exist few microns deep, depending on the distance Si (or other contaminants) has diffused inside the particle.

Although gold and silicon do not have intermetallic phases (see gold-silicon phase diagram [136], Figure 49), the eutectic microstructure observed at the surface of the particles can be a mixed structure containing gold, silicon and other contaminants from the atmosphere.

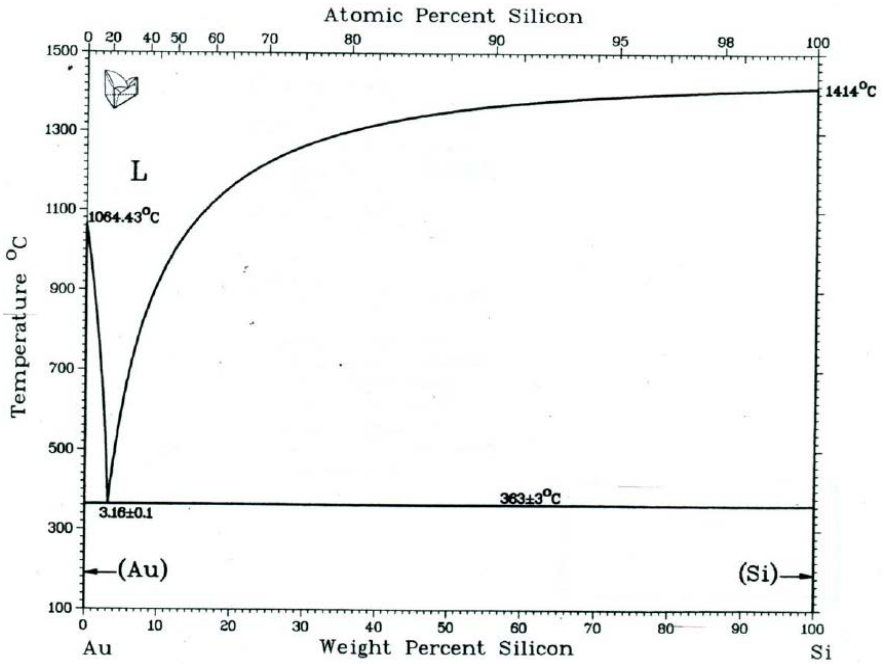

Figure 49: Gold-silicon phase diagram [136].

Together with the sample contamination by Si, it was shown that the atmosphere contained relatively large amounts of oxygen, enough to oxidize titanium in the sample, preventing it from alloying the gold particles. Assuming that there was no titanium inside the dewetted gold particles, what was achieved at the first dewetting experiment was dewetting of gold (unalloyed) in an atmosphere of Ar+7% H_2 contaminated with Si and O. The shape of the particles resembles that of pure gold dewetted on c(0001) sapphire in air [17] (Figure 50).

(a) 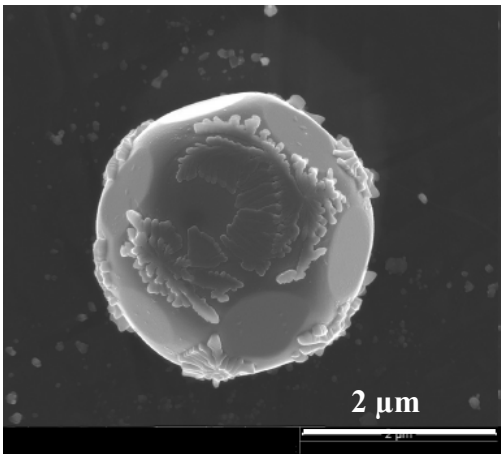

(b) 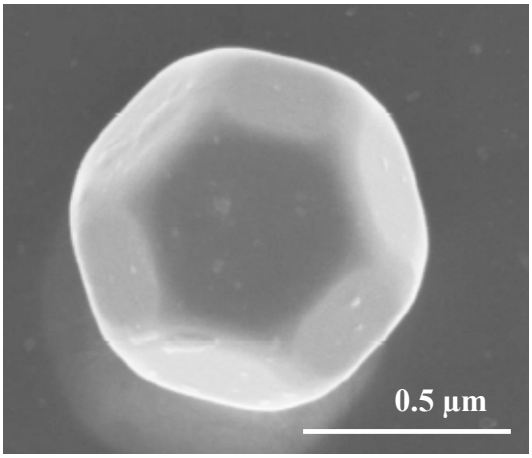

Figure 50: Comparison of gold dewetted on sapphire: (a) this work, gold+1.86 at.%Ti dewetted on c(0001) sapphire under constant flow of Ar+7%H_2, equilibrated at 900°C for 24 hr, and (b) Sadan and Kaplan [17], pure gold dewetted on c(0001) sapphire and equilibrated at 1000°C for 100 hr in air.

According to the results obtained from the first dewetting experiment, the direct influence or effect of titanium addition on the gold-sapphire system cannot be determined.

The particles that were formed during the second dewetting experiment exhibited relatively small facets, connected by large curved surfaces (see Figure 34). This shape may imply that the experimental system used was cleaner than the one used in the first dewetting experiment and even from the one used in [17]. At this stage it cannot be determined whether the shape of the gold crystallites is indeed their ECS. A relatively short time was used for equilibration (1 hr at 900°C), and further experiments with longer equilibration times are required in order to determine that, since facets can grow in size with increasing time. An example of a similar system and the effect of alloying can be seen in the work of Wang and Wynblatt [123], where the equilibrium shapes of pure gold and gold alloyed with Ge on α-SiC were studied. The equilibrium shape of pure gold was faceted, but observed facets were small and connected by large curved surfaces, in contrast to what was found by Sadan and Kaplan [17] for pure gold on c(0001) sapphire where large facets were observed (connected by small curved surfaces). Gold crystallites alloyed with 1.0 at.% Ge that were annealed for 72 hr at the solid-state (1123K) also exhibited some faceting. Facets observed in this system were small and also connected by curved surfaces. Auger analysis conducted in both cases did not show any detectable amounts of impurities at the surface (see Figure 51).

(a) 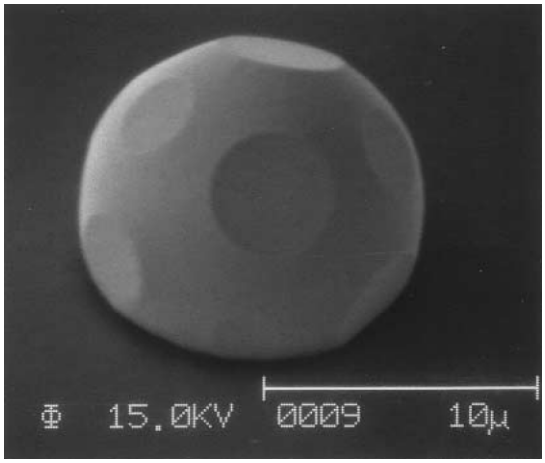

(b) 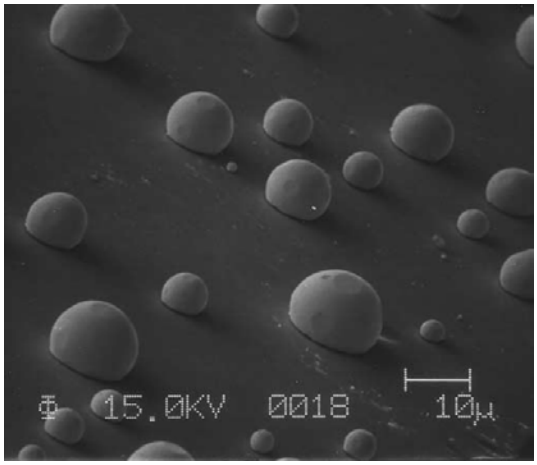

Figure 51: SEM micrograph of (a) pure gold crystallites and (b) gold crystallites alloyed with 1.0 at.% Ge on α-SiC, both after solid state annealing at 1123K for 72 hr [123].

The XRD pattern of the sample from the second dewetting experiment indicates that the Au(111) reflection is the preferred orientation (P>1) of the gold particles on the sapphire c(0001) substrate (see Figure 35). No other preferred orientation of gold was detected on sapphire. This result is different from the one reported by Sadan and Kaplan [17], and Fecht and Gleiter [59], who found two preferred orientations of pure gold dewetted on a c(0001) sapphire substrate - Au(111) and Au(200). Since the atmosphere used in these two experiments (gettered 99.9995% Ar and air, respectively) would not influence gold, they can be compared.

The meaning of Au(111) being the only preferred orientation on c(0001) sapphire is that there was an increase of interface energy anisotropy at the gold-sapphire interface in this experimental system.

If one examines a schematic γ-plot (interface energy vs. angle) for pure gold, there would be two cusps, as found by Fecht and Gleiter [59] and Sadan and Kaplan, (111) and (200) reflections (P=1.54 and 1.55, respectively) [17]. When titanium is added to the system, only Au(111) remains as the preferred orientation on sapphire.

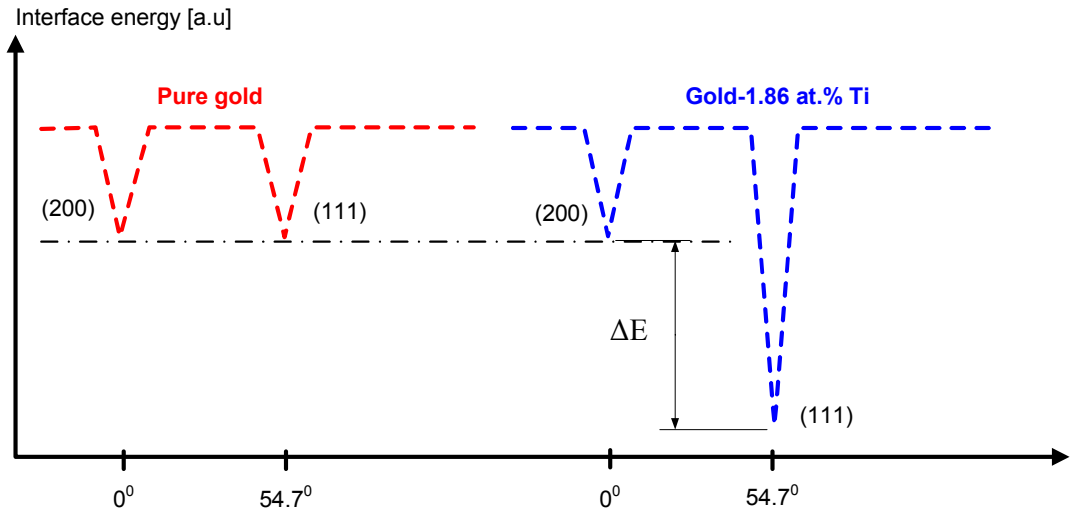

Figure 52: Schematic γ-plot of gold-sapphire interface energies, displaying two cusps relating to Au(200) and Au(111) (red) that were detected as preferred orientations on sapphire by Sadan and Kaplan [17] and Fecht and Gleiter [59], compared to Au-1.86 at.% Ti, where only Au(111) was detected as a preferred orientation (current work, blue).

The difference in composition between the two systems is the addition of titanium (in the current work). Titanium is a strong adsorbing/segregating element, but since the surface energy of titanium (γ_{Ti}=1938 mJ/m^2 [134]) is higher than that of gold (γ_{Au}=1410 mJ/m^2 [134]), it will not segregate to the surface of the gold particles. Therefore, the observed increase in interface energy anisotropy must stem from adsorption/segregation of titanium to the gold-sapphire interface, which was confirmed by examining the interface itself.

Since Au(200) was not observed as a preferred orientation in the current work, it remains more or less in the same value of interface energy, whereas the interface energy of Au(111) is further decreased by titanium segregation. As shown schematically in Figure 52, the energetic difference is now larger. Wang and Wynblatt [123] obtained similar results for Au-Ge alloys on SiC where a preferred orientation of Au(111) was detected on (0001) SiC.

Wynblatt and Chatain [9] have calculated the γ-plot for Ni and Ni-0.1 at. % Au and found an increase in surface energy anisotropy of Ni and a sharp decrease of the Ni(111) cusp due to gold segregation to the Ni surface (Figure 53).

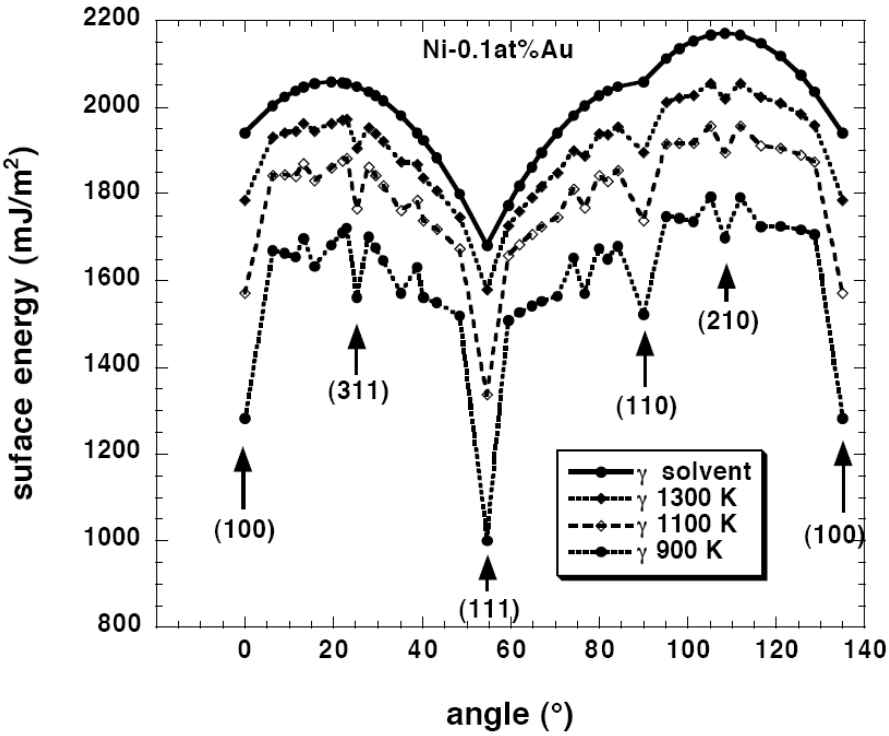

Figure 53: Calculated γ-plot showing surface energy variation with orientation for a Ni-0.1 at. % Au alloy at three different temperatures and for the pure solvent (Ni).

Although not observed in the current work, in the Ni-0.1 at. % Au system depicted in Figure 53, the segregation of gold to the nickel alloy surface (γ_{Au}=1410 and γ_{Ni}=1940 mJ/m^2 [134]) and the related changes in the anisotropy of the surface energies ((111) cusp deepens) have invoked the appearance of two new cusps at the γ-plot, at (311) and (210). If a γ-plot of gold surface energies from the first dewetting experiment is to be drawn, the presence of Si contamination (as a surface adsorbate) will probably deepen the cusps of pure gold and perhaps invoke the creation of new cusps that are not generally observed for gold (e.g. (311), (210)).

The anisotropy of surface energies can be related to the equilibrium crystal shape (ECS) by the Wulff construction. If a facet is present in the ECS, it necessarily means that a cusp is present in the surface energy (as in the γ-plot) and that the cusp also penetrates the inner envelopes of the Wulff planes from which the ECS is constructed of (see Figure 6). Measurements of ECS of pure gold on different substrates have shown that it is comprised of {111} and {100} family planes [17,45,126,132].

Another way of observing the change in the preferred orientation is by examining the corresponding convoluted ECS. If such a plot is to be drawn, then the cusps of the {111} interface planes will deepen while that of the {100} interface planes

will remain the same or even become smaller (Figure 54). Again, the anisotropy of the interface energy is increased.

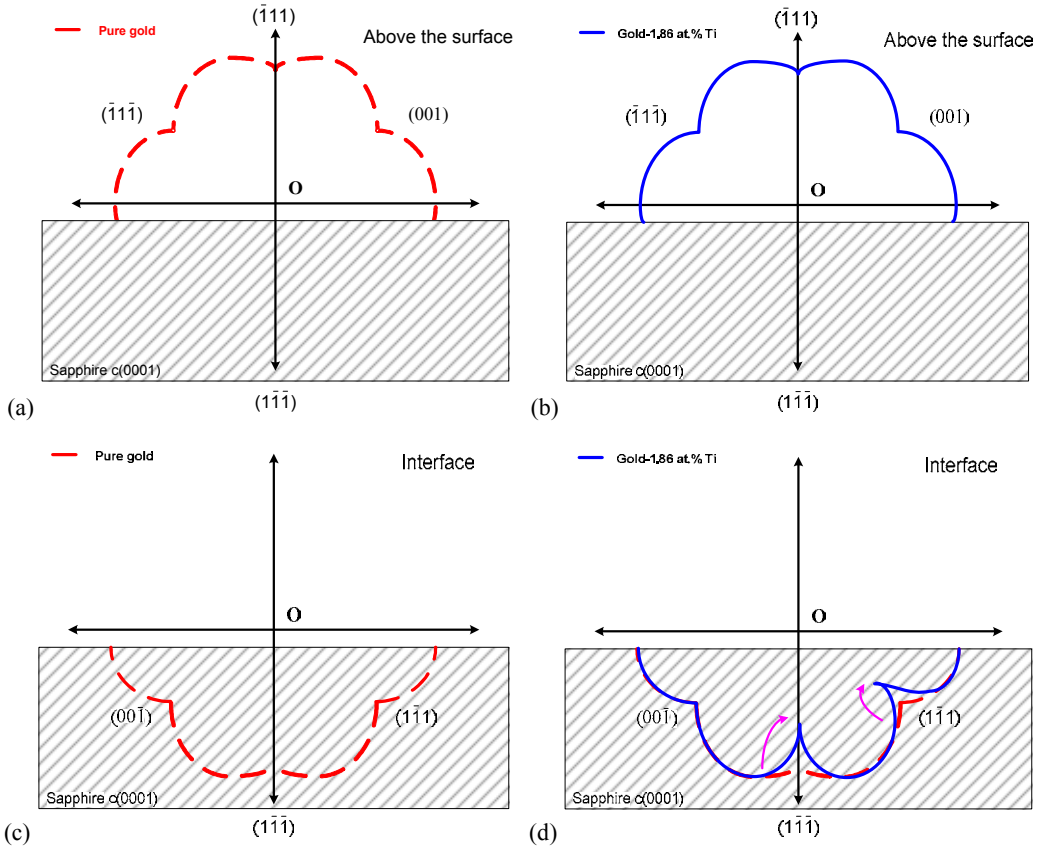

Figure 54: Schematic γ-plot of the convoluted ECS in two dimensions for an fcc single crystal: (a), (b) above the surface and (c), (d) interface energy. Dashed red line and blue line represent pure Au and Au-1.86 at.% Ti on c(0001) sapphire, respectively. The change caused by the addition of titanium is seen in (d) where cusps of {111} interface planes become deeper while cusps of {100} interface planes remain unchanged.

The major difference between the two dewetting experiments is now obvious - the first experiment did not provide Ti the suitable conditions to stay dissolved in the equilibrating gold particles, so it found its way out of the particles through diffusion to the sapphire surface, where it later oxidized. The atmosphere in the second experiment did not contain enough oxygen to "seduce" Ti out of the gold, this way it stayed dissolved and gradually adsorbed at the newly formed gold-sapphire interface. The difference in particle morphology strengthens this. The first dewetting resulted in faceted particles and gold particles had a noticeable degree of surface energy anisotropy (where large facet size can be attributed to the presence of the contaminants found, e.g. silicon). The second dewetting resulted in the formation of round particles containing

small facets. The presence of a partially ordered adsorption layer of titanium or a titanium-containing compound at the gold-sapphire interface is alone sufficient for the reduction of interfacial energy.

6.1.2 Gold-Sapphire Interface

After observing the change in the shape of the particles, from a faceted shape (with large facets) to a round shape containing small facets, and the change in the preferred orientation of gold on sapphire, examination of the interface formed (**Figure 40**) provides the ultimate proof about the presence of titanium. The partially ordered adsorbate layer formed at the interface is definitely not a bulk phase, as suggested by other authors who addressed reactive wetting [91,92,93,94,95,96,97]. Titanium has diffused to the gold-sapphire interface, where it has adsorbed. Although interface structure was not determined in detail, it is assumed that titanium adsorbed (in a way similar to multi-layer adsorption) with the first layer interacting with the first cation layer of the sapphire surface (first aluminum layer). These findings support the theory of Saiz, Tomsia and Cannon [81,82] according to which adsorption of the active element alone at the metal-ceramic interface is responsible for the improvement in wetting.

Such interface formation is known and reported in the literature. Verdozzi et al. [31] have studied this interface using *ab initio* density functional calculations and concluded that a substitutional Ti will replace a surface Al atom (assuming sapphire is Al-terminated) rather than a subsurface Al and that the Al-terminated surface is unstable under Ti adsorption. An adsorbed Ti displaces the surface Al, resulting in a mixed Ti/Al interfacial layer instead of a sharp Ti:Al_2O_3 interface. Bernath et al. [137] studied the interface between ultrathin Ti films (≤2 monolayers) and (0001) sapphire at room temperature using in-situ Auger spectroscopy and showed that Ti/sapphire interface was composed of a sub-oxide of Ti and partially reduced Al_2O_3. According to Bernath et al., interface formation started with the appearance of a Ti_2O_3-type phase, which led to pure Ti with increasing film thickness. Ti oxidation was found to take place at the interface, probably by reaction with the substrate, as evidenced in other works [138].

Although the titanium (or titanium-containing) adsorbate layer at the metal-ceramic interface was detected, it cannot be determined when that layer formed. It is possible that adsorption took place as early as in the liquid state, or later on, upon

equilibration in the solid state (at 900ºC). The titanium concentration at the interface might have been different during the liquid state, since the titanium solubility limit in gold changes (compared to the solid state). Quenching the sample after a few minutes in the liquid state (thus forcing a much higher cooling rate than the one actually used) and observing the interface could answer this.

Titanium was also found to adsorb on the free sapphire surface (see Figure 42 and Figure 43). This adsorption is likely to decrease the surface energy of sapphire, although it was not quantitatively determined in the current work. Other reports in the literature about the change in the surface energies of different planes of sapphire as a result of titanium presence/adsorption are only given in relative values [31,139].

6.1.3 Au(Ti)-Sapphire Interface Energy

Calculation of the gold-sapphire interface energy can generally be done either by using the Young equation or the Winterbottom analysis. But before applying these formulations, a careful examination of the triple junction (particle-substrate-vapor meeting point) is needed (see Figure 55).

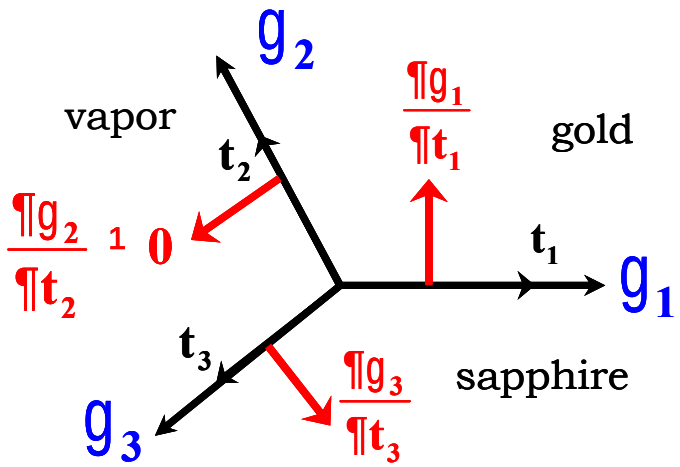

Figure 55: Schematic illustration of the triple junction between the gold particle, sapphire substrate and vapor phase [140]. Different surface and interface energies are presented, together with torque terms.

A careful analysis of the triple junction requires that torque terms be addressed, as given in the formulation of Herring [23] in eq.(6). The torque terms of the three interfaces, as shown in Figure 55, act perpendicular to each surface and express their resistance to rotate from the initial orientation. The particles that have formed in the

second dewetting experiment contained small facets, and some of them can possibly be found intercepting the triple line. The method that was used to prepare the TEM samples in this work cannot ensure that triple junction facets were not 'destroyed' during the preparation. Due to that, it cannot be determined that facets did not exist at the triple junction, and the existence of such a facet in the gold particle surface in the triple junction means that the torque term there does not equal zero ($\partial\gamma_2/\partial\theta_2 \neq 0$), and therefore cannot be neglected. In such a case, the use of Young's equation (eq.(9) is incorrect and can lead to errors in the calculation of interface energy. In addition, if Young's equation was used at the triple junction, the accurate term for γ_{PV} has to be used (and not that of Au(111)) and therefore the atomic plane of gold at the triple junction has to be determined also.

On the other hand, Winterbottom's analysis can be used for determining the gold-sapphire interface energy. But, in order to do that, the knowledge of the surface energies of the particle and the sapphire surface, γ_{PV} and γ_{SV}, respectively, are required to calculate the gold-sapphire interface energy. This type of data can be found in the literature, but it only corresponds to clean and unalloyed gold and sapphire. In the current study, it was shown that titanium has segregated to the sapphire surface, reducing its surface energy (see Figure 42 and Figure 43). Segregation of titanium to the gold particle surface is not possible, as mentioned above. Since no data was found in the literature for the change in the surface energy of sapphire due to titanium adsorption, a careful estimation of this value is required.

Using Winterbottom's analysis, eq.(21), measured values of R_1=402 nm and R_2=722 nm (see Figure 56), and reported values of $\gamma_{Au(111)}$=1.4 J/m^2 [141,142] and $\gamma_{c(0001)}$=1.24 J/m^2 [4], the obtained values for γ_{SP} and W_{ad} are γ_{SP} = 2.02 ± 0.05 [J/m^2] and W_{ad} = 0.62 ± 0.05 [J/m^2].

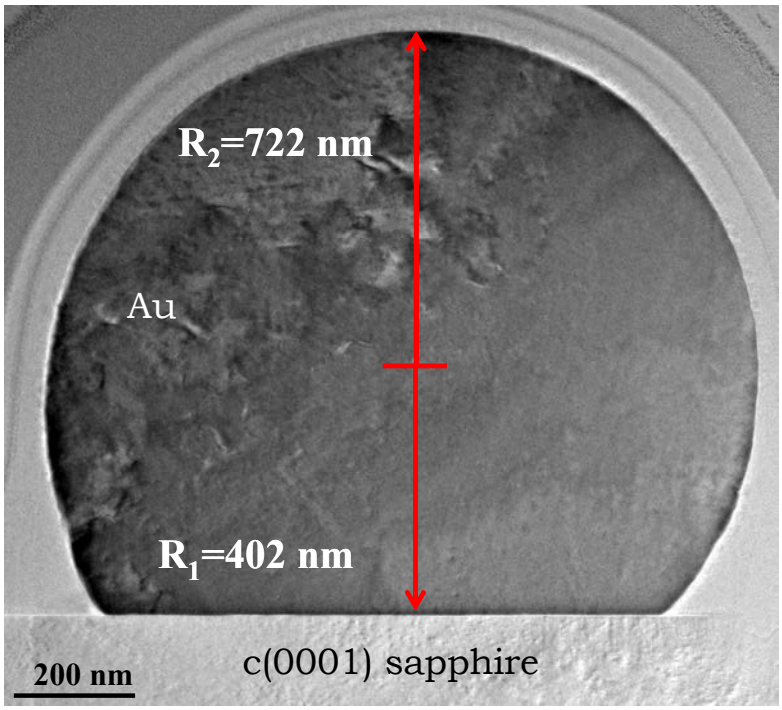

Figure 56: Aberration corrected TEM micrograph (C_S=-4.6 µm) of the cross sectioned gold particle from the 2nd dewetting experiment where Ti was detected at the gold-sapphire interface, together with R_1 and R_2 measurements relating to Winterbottom's analysis [47]. R_1 and R_2 were measured from the lamella that was extracted from the center of the particle.

The value of the interface energy obtained in this work is slightly lower than the one reported by Sadan and Kaplan [17], who conducted dewetting of pure gold on sapphire in air.

The small decrease in the interface energy observed in the current system (compared to [17]) can also be attributed to experimental errors (the difference is merely ~8%) besides the effect of titanium. But, one must keep in mind that this value (γ_{SP} = 2.02 ± 0.05 [J/m^2]) does not take into account a change in the surface energy of sapphire. Since titanium adsorbed to the sapphire surface, it must have lowered the c(0001) surface energy. Thus, a value lower than 1.24 [J/m^2] should be used for the surface energy of c(0001) sapphire in the Winterbottom equation (eq.(21)). Just as an estimation, if one takes into account a decrease of 10 to 20% in the sapphire surface energy due to titanium adsorption, than values of 1.116 and 0.992 J/m^2 can be used, respectively for γ_{SV}. When substituting these values in the Winterbottom formulation, the calculated gold-sapphire interface is in the range of $1.77<\gamma_{SP}<1.90$ J/m^2. These values represent a larger decrease in interface energy (compared to [17]), and since

there is no doubt that the surface energy of sapphire was reduced by titanium adsorption there, represent the real situation more correctly.

Wang and Wynblatt [123], who studied the Au(Ge)-SiC system have also reported that a decrease of 13-17% in γ_{SP} was observed after additions of 1.0 and 2.3 at.% Ge to Au-SiC system. Reduction was attributed to Ge segregation to the Au-SiC interface.

The observed effect of titanium on the gold particles and on the gold-sapphire interface is actually 2-fold. Titanium segregates to the surface of the sapphire substrate as well as to the gold-sapphire interface, thereby causing a reduction of the corresponding surface and interface energies. Since both terms, for γ_{SV} and γ_{SP} are reduced, the net change in the thermodynamic work of adhesion, W_{ad} (eq.(11)), can sometimes be positive but very small (depending on the specific values of surface and interface energies), as evidenced in the current work, when compared to pure gold on sapphire [17]. Systems that exhibit contact angles larger than 90°, can even experience a decrease in W_{ad} as a result of solute segregation to the surface. The maximum increase that can be achieved in W_{ad} would be if solute segregation is limited to the metal-ceramic interface and not to the surface. Similar evidence can be found in the Au(4.0 at.% Sn)-SiC system, where Sn segregation was observed at the surface and at the metal-ceramic interface. As a result, W_{ad} was increased by merely 19% [122]. On the other hand, in the Au(2.3 at.% Ge)-SiC system, where Ge segregates only to the metal-ceramic interface, W_{ad} was increased by 107 % [123].

6.2 Gold-ABA®-Sapphire Interface Structure

Alloys that contain active element additions (such as Ti, V, Zr, Hf) are commonly used in the industry for direct metal-ceramic and ceramic-ceramic joining, without the need to form a metallization layer on the ceramic surface prior to joining. The direct joining is made possible via the adsorption of the active element at the metal-ceramic interface and the creation of a reaction layer on the ceramic surface in contact with the brazing alloy. The adsorption alone is enough to cause an initial reduction in interfacial energy. Upon reaching the brazing temperature, the active element in the alloy diffuses from the liquid alloy to the ceramic surface where it adsorbs, and later (during liquid state or upon cooling) forms a generally non-continuous reaction layer.

The remaining filler metal can now wet the reaction products instead of the ceramic surface and wetting is promoted. Good adhesion between the reaction product(s) and the ceramic surface is needed at this stage.

According to the interface observed in Figure 45, it is evident that spreading of the gold alloy on the sapphire surface indeed took place and that the alloy partially wets the sapphire surface. The reaction products observed at the interface (Figure 45 - Figure 48) are clearly not continuous, as assumed and reported by other studies of reactive wetting/spreading [91,92,93,94,95,96,97].

The relatively large grains of reaction products seen in Figure 46 and Figure 47 are few hundreds of nanometers wide and ~80 nm high and the remaining gold based filler metal partially wets it. The reaction product seen in Figure 47, as evidenced by EDS, can probably be Ti_2O_3 or TiO. There is other evidence in the literature for the formation of TiO as a reaction product in metal-ceramic joints prepared using Ti-containing brazing alloys [75,108,125]. TiO is better wetted by metals than Ti_2O_3 which is highly ionic (final contact angle of molten gold on TiO reaches 28±3°, as reported by Chatain et al. [40]).

In its 'as-received' state, titanium is scattered equally in the gold alloy. When reaching the brazing temperature, the alloy liquefies and diffusion rates are higher for all comprising elements. Titanium diffusion can start at the solid state, and faster diffusion rates are expected in the liquid state of the brazing alloy. Titanium then diffuses to the newly created interface with sapphire where it adsorbs. At the interface, driven by the reduction in interfacial energy, two reactions can take place. Sapphire dissociates and oxygen combines with adsorbed titanium to form the oxides:

$$y \cdot Al_2O_3 \rightarrow 2y \cdot Al + 3y \cdot [O]_{Au} \tag{34}$$

$$X \cdot [Ti]^{ads.}_{Al_2O_3} + Y \cdot [O]_{Au} \rightarrow Ti_XO_Y \quad (Y \equiv 3y) \tag{35}$$

$$y \cdot Al_2O_3 + X \cdot [Ti]^{ads.}_{Al_2O_3} \rightarrow Ti_XO_Y + 2y \cdot [Al]_{Au} \tag{36}$$

where $[Ti]^{ads.}_{Al_2O_3}$ denotes the adsorbed Ti at the sapphire surface.

Combining the first two reactions yields the third one, which is basically the reduction of sapphire by the adsorbed titanium. This stage probably takes place upon cooling, as supported by Saiz et al. [81-84,86], Derby et al. [88,89] and Frage et al. [90],

and since the period of time spent in the liquid state in conventional brazing processes is not long enough compared to reaction kinetics.

Titanium starts its path to the interface during the heating cycle, when it partially dissolves from the bulk alloy (or from precipitates inside the alloy, e.g. Sn_5Ti_6 in Sn3Ag1Ti alloy in the case of tin-silver alloys containing titanium on Al_2O_3 [109]). Together with this dissolution and with the rising temperature, substrate dissolution occurs, (according to eq.(34)), enriching the liquefying braze alloy in the close vicinity of the ceramic surface with aluminum and oxygen, but leaving local defects at the surface, thus changing its structure. Titanium, now free to diffuse across the molten braze alloy, reaches the sapphire-gold alloy interface and adsorbs there, most likely around these defect areas.

Wetting of the ceramic surface is made possible here, although a reaction layer does not form continuously across it (as opposed to what is claimed by Eustathopoulos [91]). Although not seen here clearly, there is some evidence [109] of substrate dissolution at the interface in similar systems, as written in the above reaction. Ridging of the substrate, as reported in previous works on reactive systems [81-83], was not observed in the current work.

The experimental setup used in this study for the gold-ABA®-sapphire system is very different than the one used for classic sessile drop experiments, from which most of the data found in the literature is extracted. The current setup was chosen because it best simulates the situation in real brazing processes. In contrast to sessile drop experiments, where the liquid surface is exposed to the furnace atmosphere (vapor phase), in the current setup only the edges of the brazing alloy foil were exposed to the furnace atmosphere. Since commercial vacuum brazing processes are usually carried out in vacuum levels of $\sim 10^{-5}$ torr (and not under UHV conditions), there is a fairly high partial pressure of contaminants, such as oxygen, nitrogen and hydrocarbons (from oil-based pumping systems). These can react with titanium present in the brazing alloy (mainly oxygen) during the process and can produce some local chemical gradients of titanium or of titanium-containing compounds. This in turn can change the microstructure formed at the alloy-sapphire interface especially in the triple junction area, which is different than the one in sessile drop experiments.

As can be seen above (according to eq.(34)-(36)), different titanium oxides can form at the gold-sapphire interface, depending on the amount of titanium adsorbing at this interface, and since it is basically a chemical reaction, on time and temperature also.

Since the concentration of titanium was probably not the same all across alloy area (furnace temperature and alloy in-homogeneities, impurities etc), and oxygen availability was different across the sapphire surface, different oxides can form. Increasing the temperature and/or time would allow more titanium to adsorb at the interface and more substrate will dissolute. The structure of the interface depicted in the HRTEM images will probably change if it was held in a higher temperature and/or for longer durations, titanium oxide grains will probably grow and become more uniform and the most energetically favorable oxide will form, leading to an improvement in wetting (and a decrease in contact angle in sessile drop measurements conducted on the same system [143]). Different intermetallics of gold and titanium and aluminum and titanium can form locally if higher temperatures and/or longer durations at the brazing temperature are used and if favored thermodynamically. These can have a deleterious impact on the mechanical properties of the joint, through creation of brittle intermetallics that can cause interfacial failure due to cracking under applied typical mechanical stresses.

After a sufficient amount of Ti has adsorbed at the ceramic surface (few monolayers) and an initial reduction of interfacial energy was achieved, spreading can move into the second stage, when reaction product phase starts to form. Whether or not this product forms at the liquid state or precipitates during cooling, the final result of total interface energy reduction and promotion of wetting/spreading is achieved.

7. Summary and Conclusions

The purpose of this work was to examine the influence of titanium addition on metal-ceramic interfaces. The specific influence of titanium was determined through the use of the Winterbottom analysis, utilized successfully in the past in the pure gold-sapphire system by Sadan and Kaplan [17], and through examination of the interface that formed between Ti-alloyed gold and c(0001) sapphire. Samples were prepared by liquid-state dewetting of multi-layered thin films of gold and titanium (with 1.86 at. % titanium) on basal plane sapphire substrates. Dewetting resulted in the formation of a large number of particles with sizes ranging from submicron to few microns. Particles were then annealed in the solid-state at 900°C, with the entire process carried out under a constant flow of Ar+7%H_2 (1st dewetting experiment) and under a constant flow of gettered 99.999% Ar (2nd dewetting experiment).

Equilibrated particles from the 1st dewetting experiment were completely faceted. However, due to imperfect experimental conditions, titanium was not detected in cross sectioned particles and silicon contaminated the surface of the gold particles, therefore not allowing to determine the effect of titanium. Changes in the experimental setup were implemented successfully in the 2nd dewetting experiment, resulting in round particles that exhibited small facets. A preferred orientation of Au(111) || c(0001) sapphire was observed using XRD for the entire dewetted sample, and the same low-index orientation relationship between gold and sapphire was confirmed for a single particle that was examined using electron diffraction. Titanium was found to adsorb at the gold-sapphire interface.

Cross sectioned Ti-alloyed gold particles were examined using TEM, and titanium was detected at the gold-sapphire interface as a partially ordered adsorbate layer and not as a bulk phase, having a thickness of ~1 nanometer. Titanium excess at the interface was determined as 2.2 $^{\text{Ti atoms}}/_{\text{nm}^2}$ (corresponding to ~0.2 monolayer). Titanium was also observed wetting the triple junction of the equilibrated particle and adsorbing on the free sapphire surface beyond the borders of the gold particle as an adsorbate layer. Titanium excess at the free surface of the sapphire substrate was determined as 4.6 $^{\text{Ti atoms}}/_{\text{nm}^2}$ (corresponding to ~0.5 monolayer).

The Winterbottom analysis was applied in order to determine the interface energy for $Au^{(Ti)}_{(111)}$-sapphire c(0001). The calculated values of the interface energy and

the work of adhesion were determined as $\gamma_{SP} = 2.02 \pm 0.05$ [J/m^2] and $W_{ad} = 0.62 \pm 0.05$ [J/m^2], respectively.

Since the actual surface energy of sapphire was reduced (due to observed titanium adsorption there), this value of the interface energy is the highest value possible in this case, with the actual one being lower. Since the sapphire surface energy was not determined (at its reduced state), this value was not obtained. The same applies for the work of adhesion, where the calculated value is the absolute low value possible for this system.

Together with the dewetting experiments, a sapphire-sapphire ceramic joint was prepared using a Ti-containing commercial brazing alloy and characterized, where main focus was put on the metal-ceramic interface formed during the brazing process. The interface microstructure observed contained discrete and isolated reaction products 'islands' that resided on the sapphire surface. Reaction products were qualitatively identified as various grains of titanium oxides. A continuous reaction product phase/layer was not observed at the ceramic surface.

Based on these results, the following conclusions can be drawn:

1. Dewetting of a metal alloyed with a reactive element such as titanium is possible, with special care given to the experimental conditions and possible contaminants.
2. Particle morphology and shape achieved in the 2nd dewetting is the lowest energy configuration for this system. In order to determine whether this is the equilibrium crystal shape, more experiments with longer annealing times are required.
3. During the creation of a new metal-ceramic interface containing an active element, adsorption of that element is the initial step that takes place. This adsorption reduces interfacial energy and allows spreading/wetting to proceed successfully.
4. The creation of the reaction product occurs only as a bi-product of titanium adsorption at the ceramic surface. This reaction takes place only after active element adsorption and can occur during liquid state or during cooling, depends on specific experimental conditions and material selection. In very fast spreading systems, this stage does not take place and adsorption alone is responsible for the observed improvement in wetting.

5. The results obtained in this work support the "adsorption/ridge controlled spreading" approach proposed by Saiz et al. [81-84,86] and strengthen the theory that active element adsorption is the most important step that improves wetting/spreading in reactive metal-ceramic systems.
6. This work involved dedicated aberration corrected TEM, STEM and high resolution TEM imaging which is crucial for the understanding of metal-ceramic interfaces. From all literature data reviewed in this work, only a few used TEM for interface examination [e.g. 108,109]. It is rather hard to conclude about interface structure and related properties without the use of transmission electron microscopy, since one of the objects in doing so is the determination of atomistic structure there. Therefore, the use of TEM should be an integral part of every examination of metal-ceramic interfaces.

8. Recommendations for Future Work

Experiments conducted in this work were limited to a single gold-titanium film composition (1.86 at. % Ti), sapphire substrate orientation (basal plane) and two set points of experimental conditions (atmosphere gas and equilibration times and temperatures). In addition, samples were examined only after cooling spontaneously to room temperature.

In light of the findings from this work, it would be of interest to examine particles created in the same profile of the 2nd dewetting experiment, after extracting them from the furnace at different stages of dewetting. This includes quenching directly after melting of the film, quenching upon reaching the equilibration temperature (900°C) and quenching after first solidification of the dewetted particles (during cooling stage that follows melting). Examining particle-substrate interfaces at each of these stages should provide an answer, or at least an insight, for the role titanium plays during dewetting and subsequent equilibration and perhaps to the stage of the dewetting process in which the adsorbate layer forms.

As means of comparison to existing experimental data on reactive metal-ceramic systems, the same experiments suggested above should be repeated in the sessile drop configuration, hand in hand with TEM interface examination.

In order to correlate titanium presence and influence on the metal-ceramic interface with mechanical properties of the joint, experiments suggested above (both in dewetting and sessile drop configurations) can be conducted in two configurations, with titanium and without. This way, thermodynamic terms such as interfacial energies and work of adhesion can be calculated and compared to the mechanical properties of the joint. By controlling the thermal process and titanium content a reliable and mechanically strong joint can be engineered.

Preliminary work aimed at determining the atomistic structure of the interface was done (see Figure 41). In order to complete the picture of interfaces in reactive metal-ceramic systems such analysis is needed. This could clarify the structure of the observed adsorbate layer, and determine its structure (metallic titanium, oxidized titanium or an intermetallic compound of titanium and gold or titanium and aluminum).

Appendix 1 - Detection Limit - Theory and Calculations

A.1.1 Theoretical Background

When conducting quantitative analysis of thin specimens using EDS or similar methods, one must know the instrumental limitations and detection limits and be able to calculate it.

Over the years, analytical microscopy technologies have improved a great deal, enabling the user to achieve lattice images and conduct quantitative analysis. Along with this technological evolution, came the understanding that in many cases, material properties can be influenced greatly by elemental segregation to grain boundaries and interfaces and that these were critical to identify and quantify. Impurity segregation to grain boundaries, as in the case of Bi segregation to Cu grain boundaries, is known to cause embrittlement [144]. Modern electron microscopes and EDS and EELS spectrometers enable identification of segregation, which can sometimes be at the monolayer level.

The electrons originating from the incident beam interact with the specimen and some interaction volume is created across it. Thick specimens are very different from thin ones on this aspect (Figure 57).

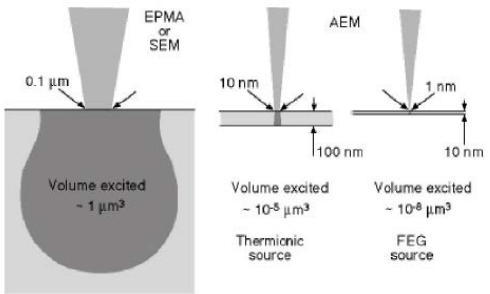

Figure 57: Illustration of interaction/excited volume created in thick and thin samples, showing the basic differences in probe size, the volume that is excited and sample thickness. Image taken from [145].

The size of the excited volume decreases with decreasing sample thickness and decreasing accelerating voltage, and it is mainly influenced by the probe size (beam sample created on the sample surface) and the broadening of the beam inside the specimen. When using EELS for quantitative analysis in thin specimens, beam

broadening inside the specimen is less influential, since largely scattered electrons are excluded from the detector [146]. The large, onion shaped, interaction volume in thick specimens is greatly reduced when working with thin specimens and can be generally equal to the volume of a cylinder whose height and diameter are the sample thickness and the incident electron beam diameter, respectively. Moving from a thick bulk specimen to a thin specimen improves spatial resolution by orders of magnitude. One common definition of spatial resolution is the one given by Williams (1992) [147]. According to this definition, spatial resolution is the diameter of the volume that contains 90% of the generated signal. When dealing with objects smaller then the spatial resolution, different assumptions have to be made that describe the interaction volume. The size and shape of the interaction volume, together with instrument parameters will influence detection limits. Although modern microscopes offer extremely small probe sizes, the spatial resolution does not follow the same values and will be a bit larger. The desire to further decrease probe size clashes with the desire to improve detection limits. Smaller probe size leads to smaller probe currents and the signal generated from the specimen is lower, thus further lowering the detection limit. EDS spatial resolutions of the nanometer scale are achieved with probe sizes in the angstrom scale [144].

Beam broadening inside the specimen is mainly a function of the specimen and one character of the microscope, the accelerating voltage, as illustrated in Figure 58.

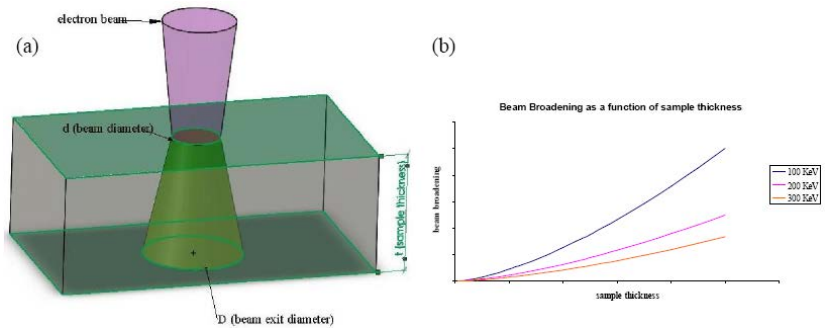

Figure 58: (a) Illustration of beam broadening inside a thin specimen. (b) Beam broadening as a function of specimen thickness at three different accelerating voltages, for the same material.

The most common expression for beam broadening inside a thin specimen was given by Goldstein et al. [148], under the assumption of single scattering (single scattering approximation):

$$b\,[cm] = 6.25\times 10^{5}\cdot\frac{Z}{E_0}\cdot\left(\frac{\rho}{A}\right)^{1/2}\cdot t^{3/2} \qquad (37)$$

where Z is the atomic number, E_0 is the incident beam energy [eV], ρ is the density [gr/cm^3], A is the atomic mass [gr] and t is the sample thickness [cm]. When dealing with more than one element, average values can be used for Z, ρ and A.

Using eq.(37), the interaction volume illustrated in Figure 60.a can be calculated as the volume of a cut cone whose upper diameter is the probe size, d, and the lower diameter is the next square root - $\boldsymbol{D} = \sqrt{\boldsymbol{b}^2 + \boldsymbol{d}^2}$. The effect of accelerating voltage on the amount of beam broadening is also apparent, as illustrated in Figure 58.b.

The incident electrons originating from the beam reach the specimen surface and penetrate. Inside the specimen the electrons interact with the constituent atoms, some pass and some are backscattered, with energy transfer accompanying each encounter. Two more important processes that take place are adsorption and fluorescence. Considering these processes leads to the known ZAF correction.

The rate of energy loss is dependent upon electron energy and mean atomic number of the specimen. Stemming from this is the fact that electrons will behave differently in the specimen and standard. The correction needed in this case is the atomic number correction, Z_i. This correction considers the stopping power factor, termed S, when it is assumed that electrons loss their energy completely upon encountering the specimen. But in reality, this is not 100% true, and some electrons are backscattered, having some finite energy. The amount of backscattered electrons depends on the specimen's atomic number as well, and this gives rise to the backscatter factor, termed R. Backscattering and stopping power tend to cancel each other and atomic number corrections are usually smaller than 15% [149]. Expressions for the stopping power factor, S, are given by Duncumb & Reed [150], but will not be specified here.

A.1.2 Thin Specimens

When dealing with thin specimens, the observed or measured x-ray intensity will be a function of specimen thickness and composition as well. Now, instead of measuring absolute x-ray intensities, the ratio of x-ray intensities is measured and later

converted into weight fractions. Since the sample is thin, electron energy decreases by only a small fraction and the probability for an ionization event (known as the ionization cross section, Q) is rather constant. Based on this and by assuming that in thin specimens (suitable for TEM analysis) x-ray absorption and x-ray fluorescence can be ignored, Cliff & Lorimer [151] have formulated the ratio technique:

$$\frac{C_A}{C_B} = k_{AB} \cdot \frac{I_A}{I_B} \tag{38}$$

where C_A and C_B are the weight fractions of the two elements of interest, I_A and I_B are the measured characteristic x-ray intensities for elements A and B, respectively and k_{AB} is a factor which can be determined using suitable standard or calculated. For normalization, $\sum C_n = 1$, so following conversion from weight fractions to weight percentages is made possible.

This way, the x-ray intensity ratio is measured and not absolute x-ray intensities, leading to an expression that is independent of specimen thickness. Since the intensities, I_A and I_B, are measured simultaneously, they are independent of fluctuations in probe current.

When absorption effects cannot be neglected, it must be taken into account in the ratio technique. X-ray absorption in the specimen behaves according to Beer's law:

$$I_A = I_{0A} \cdot e^{-(\mu/\rho)^A_{Spec} \cdot \rho \cdot x} \tag{39}$$

where I_A is the transmitted x-ray intensity, I_{oA} is the initial x-ray intensity (incident beam), $(\mu/\rho)^A_{Spec}$ is the mass absorption coefficient of A, x is the absorption path (illustrated below) and ρ is the density:

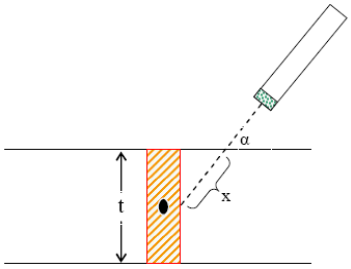

Figure 59: Adsorption path length, *x*, and detector angle, *α*.

When the x-ray measurement is done by a detector mounted by an angle α to the specimen, and the absorption path length is x, the measured intensity ratio I_A/I_B will be different from the one measured with an infinitely thin specimen ("ideal thin specimen"), I_{oA}/I_{oB}. When adsorption effects are taken into account, the ratio I_A/I_B will take form [152]:

$$\frac{I_A}{I_B} = \frac{I_{oA}}{I_{oB}} \cdot \left[\frac{\left[\mu/\rho \right]^B_{Spec}}{\left[\mu/\rho \right]^A_{Spec}} \right] \cdot \left[\frac{1 - exp - \left\{ \left[\mu/\rho \right]^A_{Spec} \cdot \rho \cdot t \cdot \sec\alpha \right\}}{1 - exp - \left\{ \left[\mu/\rho \right]^B_{Spec} \cdot \rho \cdot t \cdot \sec\alpha \right\}} \right] \tag{40}$$

where, again, I_A/I_B is the intensity ratio measured from the real specimen including absorption effects and I_{oA}/I_{oB} is the ratio measured from an ideal, thin specimen. Now, after these effects are introduced, k_{AB} from eq.(40) can be corrected:

$$k^*_{AB} = k_{AB} \cdot \underbrace{\left[\frac{\left[\mu/\rho \right]^A_{Spec}}{\left[\mu/\rho \right]^B_{Spec}} \right] \cdot \left[\frac{1 - exp - \left\{ \left[\mu/\rho \right]^B_{Spec} \cdot \rho \cdot t \cdot \sec\alpha \right\}}{1 - exp - \left\{ \left[\mu/\rho \right]^A_{Spec} \cdot \rho \cdot t \cdot \sec\alpha \right\}} \right]}_{Absorption\,Correction\,Coefficient \equiv ACF} \tag{41}$$

The absorption path marked as $'x'$ in Figure 59 is actually $t \cdot \sec\alpha$ in the case where the incident beam is normal to the specimen.

The last effect that needs to be taken into consideration is fluorescence in the thin specimen. When measuring characteristic x-ray intensity from element *A* in a thin specimen, its consideration can sometimes appear higher than it really is, due to fluorescence effects. This happens when characteristic x-ray from *A* is enhanced by

secondary x-ray fluorescence from element *B*. Fluorescence of element *A* by element *B* can take place only if the energy of x-rays emitted by element *B* is greater than the excitation energy of element *A*, E_C.

The magnitude of fluorescence in thin specimens is smaller than in bulk samples, since the interaction or excited volume is smaller. A correction term for fluorescence effects was formulated by Nockolds et al. [152,153]. Using Figure 60, the term is:

$$\frac{I_A^F}{I_A} = C_B \cdot \omega_B \left(\frac{r_A^{-1}}{r_A} \right) \cdot \frac{A_A}{A_B} \cdot \left[\frac{\mu}{\rho} \right]_A^B \cdot \frac{U_B}{U_A} \cdot \frac{\ln U_B}{\ln U_A} \cdot \frac{\rho \cdot t}{2} \cdot \left[0.923 - \ln \left[\frac{\mu}{\rho} \right]_{Spec}^B \cdot \rho \cdot t \right] \cdot \sec\alpha \qquad (42)$$

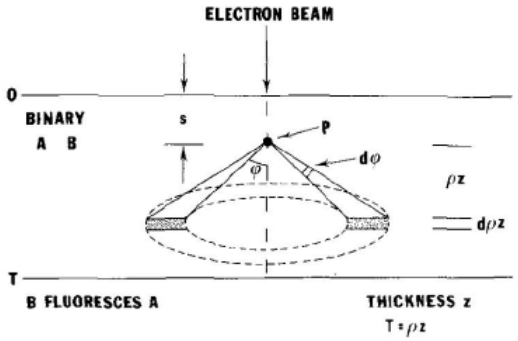

Figure 60: Illustration of the interaction of the incident beam with the specimen used to formulate the fluorescence correction term. Image taken from [153].

where I_A^F / I_A is the ratio of the fluorescence intensity to primary intensity, ω_B is the fluorescence yield of element B, r_A is the absorption edge jump ratio of element A, $[\mu/\rho]_A^B$ and $[\mu/\rho]_{Spec}^B$ are the mass absorption coefficients of element B radiation in element A and the specimen respectively, A_A and A_B are the atomic weights, U_A and U_B are the over voltages for the characteristic radiation of A and B and α is the tilt angle.

In the case where absorption and fluorescence effects have to be taken into account, eq.(38) turns into:

$$\frac{C_A}{C_B} = k_{AB} \cdot \frac{I_A}{I_B} \cdot [ACF] \cdot \frac{1}{\left[1 + \frac{I_A^F}{I_A} \right]} \qquad (43)$$

In most cases, the effects of absorption are greater than those of fluorescence. In addition, eq.(38) can be used in ternary systems:

$$C_A + C_B + C_C = 1$$
$$\frac{C_B}{C_C} = k_{BC} \cdot \frac{I_B}{I_C} \quad \Rightarrow\Rightarrow \quad k_{AB} = \frac{k_{AC}}{k_{BC}} \tag{44}$$

Eq.(38) can be used also to determine the detection limit for element A in a thin specimen. The minimum detectable limit (minimum mass fraction, MMF) is the limit for the smallest significant x-ray signal detected from element A that is above the background [152]. When looking for a peak for element B, the observed peak is thought to be real if it is larger than three standard deviations of the background intensity:

$$I_B \geq 3\sqrt{I_B^b} \tag{45}$$

where I_B is the intensity measured for element B and $\boldsymbol{I_B^b}$ is the background intensity under the peak of element B, or in its near surrounding. Now eq.(38) can be converted into weight percentages:

$$\frac{I_A}{I_B} = k_{AB} \cdot \frac{C_A}{C_B} \;\Rightarrow \overset{C_B \to min}{\Rightarrow} \Rightarrow \; \frac{I_A}{I_B} = k_{AB} \cdot \frac{C_A}{MMF_B}$$
$$\Rightarrow\Rightarrow\Rightarrow \; MMF_B = k_{AB}^{-1} \cdot \frac{3 \cdot C_A}{I_A} \cdot \sqrt{I_B^b} \tag{46}$$

Another formulation for the same matter was given by Keast and Williams [146], where grain boundary segregation was quantified in the analytical electron microscope. Grain boundary coverage was defined as:

$$\Gamma = \frac{V}{A} \cdot \rho \cdot k_{sm} \cdot \frac{A_m}{A_s} \cdot \frac{I_s}{I_m} \tag{47}$$

where ρ is the matrix density in [atom/nm^3], A_m, A_s, I_m and I_s are the atomic masses and the intensities of the matrix and the segregant, respectively. The ratio V/A is the ratio of the interaction volume to the area of the grain boundary inside this volume. This ratio is a function of the probe size and specimen thickness. When beam broadening can be

neglected, *V* and *A* refers to a cylindrical interaction volume with a diameter equal to the probe size, *d*:

$$\frac{V}{A} = \frac{\pi}{4} \cdot d \tag{48}$$

In cases where beam broadening cannot be neglected, the shape of the interaction volume is given as in Figure 58.a and the ratio *V/A* is:

$$\frac{V}{A} = \frac{\pi}{4} \cdot \left(\frac{d^2 + b \cdot d + b^2/3}{d + b/2} \right) \tag{49}$$

This kind of mathematical treatment assumes that electron density in the specimen is constant, and was used in the study of bismuth segregation in copper by Baumann & Williams [154] and Michael and Williams [155]. Additional formulations to the ratio V/A exist, depending on the shape of the interaction volume and distribution of electron density inside it as a function of sample thickness [146], but will not be given here.

One more way of treating the shape of the interaction volume is made possible when using a raster scan of the electron beam on the specimen surface rather than a stationary beam. When a raster scan is used (STEM mode), the ratio of *V/A* is the width of the scan normal to the area scanned, $\boldsymbol{V/A = w}$. There are several good reasons for using a raster scan across the specimen surface than a stationary probe. Although the sensitivity is lower in the raster mode, specimen damage caused by the incident beam is minimized; specimen drift can be detected and corrected accordingly and the interface of grain boundary examined does not have to be oriented directly parallel to the beam, since the raster scan can include a big part of it. One more thing to realize is that the smallest probe size available in a given microscope, will not lead directly to the best detectability. When the probe size becomes smaller, the probe current decreases, and the signals generated are thus fewer and weaker. In many cases, a better detectability will be achieved by choosing some intermediate probe size and not the smallest.

Using eq.(47), Keast and Williams [146] have formulated another expression for what was termed minimum detectability. A peak in an x-ray spectrum can be considered statistically real when:

$$I - I^b \geq 3\sqrt{I + I^b} \tag{50}$$

where I is the peak intensity, I^b is the background intensity under the peak. When searching for an element close to the detection limit, I is very close to I^b. This way, the minimum detectability can be defined as:

$$\Gamma_{min} = \rho \cdot k_{sm} \cdot \frac{A_m}{A_s} \cdot \frac{V}{A} \cdot 3 \cdot \frac{\sqrt{2 \cdot I_s^b}}{I_m} \tag{51}$$

where $\boldsymbol{I_s^b}$ is the background intensity under the peak of interest and Im is is the intensity of the matrix element. If one uses the simplest approximation of the interaction volume as a simple cylinder, the ratio V/A is given by eq.(48), and then eq.(51) becomes:

$$\Gamma_{min} = \rho \cdot k_{sm} \cdot \frac{A_m}{A_s} \cdot \frac{\pi}{4} \cdot d \cdot 3 \cdot \frac{\sqrt{2 \cdot I_s^b}}{I_m} \qquad \left[\frac{atoms}{nm^2}\right] \tag{52}$$

Besides the k-factor (k_{sm}), all parameters here can be measured from a specific TEM sample. In order to complete the parameters needed for the calculation of the detection limit, the k-factor needs to be determined.

A.1.3 Detection Limit Calculations

In order to extract the k-factor for Au-Ti, a sample of the AuTi intermetallic was prepared using an electric arc furnace. Suitable weights of titanium and gold (pure forms) were taken in order to prepare samples for arc furnace melting. The sample was melted inside a copper crucible, using a Miller Goldstar 500SS constant current DC arc welding power source, operated at 300 ampere. The sample was melted five times in the furnace under 99.999% Ar atmosphere. After melting, the sample was cut (in order to

expose the bulk) and heat treated at 1,000°C for 70 min in a vacuum level of ~1x10^{-5} torr. After heat treatment, the sample was cast in Bakelite, polished down to 1 µm and examined using EDS in SEM and TEM. The general microstructure of the sample can be seen in Figure 61.

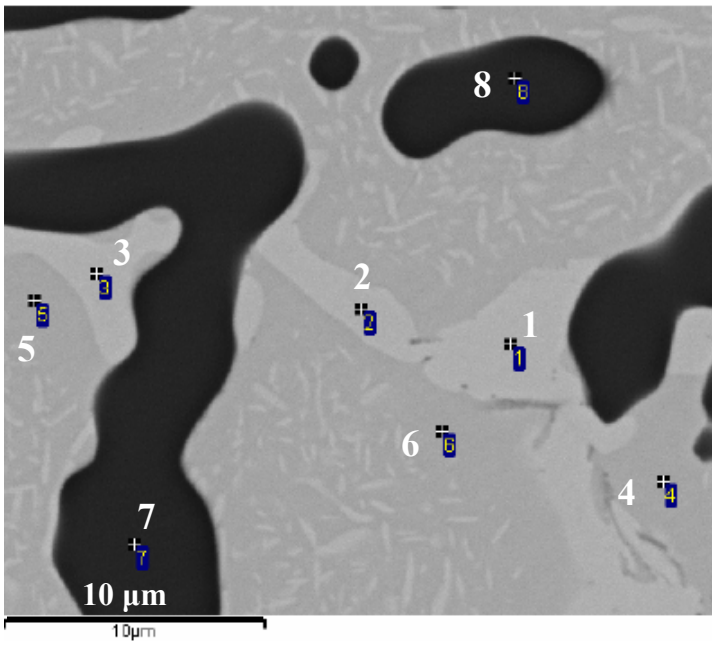

Figure 61: Backscattered electrons SEM micrograph of the microstructure of AuTi sample prepared in an electrical arc furnace. Three phases are visible.

As can be seen in Figure 61, three phases formed during arc melting and subsequent heat treatment:

1. White phase (points 1-3): having a composition of 89.78±0.34 wt. % Au (68.12±0.79 at. %) and 10.22±0.34 wt. % Ti (31.88±0.79 at. %). This phase was identified as the Au_2Ti intermetallic phase.
2. Grey phase (points 4-6): having a composition of 82.55±0.66 wt. % Au (53.50±1.16 at. %) and 17.45±0.66 wt. % Ti (46.50±1.16 at. %). This phase was identified as the α-AuTi intermetallic phase.
3. Black phase (points 7-8): having a composition of 83.82±0.02 wt. % Ti (56.50±0.06 at. %) and 16.18±0.04 wt. % C (43.50±0.06 at. %). This phase was identified as TiC. Carbon is from the graphite electrode used in the electric arc furnace.

From this sample, a TEM specimen was prepared using the 'lift-out' technique in the FIB. A grain of the white phase seen in Figure 61 was chosen for EDS analysis and 15 scan boxes were taken along it in the TEM (see Figure 62).

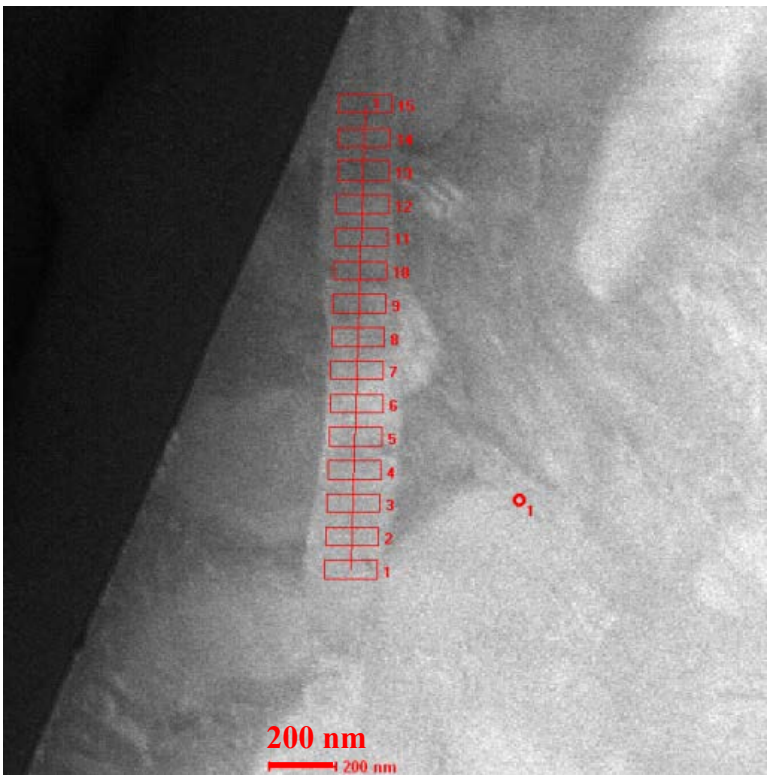

Figure 62: High angle annular dark field TEM micrograph of the white phase grain together with position of 15 EDS scan boxes taken along it.

Based on these scan boxes and using eq.(38) for k-factor formulated by Cliff and Lorimer [151], $k_{Au\text{-}Ti}$ was determined as $k_{Au\text{-}Ti}$=0.94±0.18.

In order to determine the excess of titanium at the gold-sapphire interface, a series of EDS scans were conducted on the particle from the 2nd dewetting experiment (see Figure 38), at three places - bulk of the particle, gold-sapphire interface and sapphire bulk. All three scans were conducted under the same conditions. As expected, no titanium was detected at the bulk of the sapphire substrate. The amounts of titanium at the bulk of the particle and at the gold-sapphire interface were calculated according to eq.(47). The excess of titanium was then obtained by subtracting the amount of titanium in the bulk from that in the interface. This way, the excess of titanium at the interface was determined as 2.2 $^{\text{Ti atoms}}/_{\text{nm}^2}$.

For the particle seen in **Figure 38**, the detection limit for titanium was also determined, using eq.(51). The value obtained was 1.8 $^{\text{Ti atoms}}/_{\text{nm}^2}$. Based on the Au(111)

plane as the interface plane the detection limit is 0.15 monolayer, and based on the Al-terminated c(0001) sapphire surface this value is 0.18 monolayer. The value obtained for the excess of titanium at the interface is significantly higher than the detection limit (expressed in terms of excess).

References

1. J. M. Howe, Bonding, *Structure and Properties of Metal/Ceramic Interfaces: part 1, Chemical Bonding, Chemical Reaction and Interfacial Structure*, International Materials Reviews, 38[5]:233-256, (1993).

2. G. Kaptay, *A unified Model for the Cohesive Enthalpy, Critical Temperature, Surface Tension and Volume Thermal Expansion Coefficient of Liquid Metals of BCC, FCC and HCP Crystals*, Materials Science and Engineering A 495[1-2]: 19-26, (2008).

3. A. B. Alchagirov, B. B. Alchagirov, T. M. Taova and K. B. Khokonov, *Surface Energy and Surface Tension of Solid and Liquid Metals. Recommended Values*, Trans. JWRI, 30: 287-291, (2001), special issue.

4. G. Levi and W. D. Kaplan, *Aluminum-Alumina Interface Morphology and Thermodynamics From Dewetting Experiments*, Acta Materialia 51[10]: 2793-2802, (2003).

5. L. E. Murr, *Interfacial Phenomena in Metals and Alloys*, 34; 1975, Reading, MA, Addison-Wesley Publishing Co.

6. E. D. Hondros, *Precipitation Processes in Solids*, 1; 1978, Warrendale, PA, The Metallurgical Society of AIME.

7. M. McLean and H. Mykura, *Orientation Dependence of Surface Tension (the Gamma Plot) for Face-Centered Cubic Iron*, Acta Metallurgica, 12[3]: 326-8, (1964).

8. H. Mykura, *The Variation of the Surface Tension of Nickel with Crystallographic Orientation*, Acta Metallurgica, 9[6]: 570-576, (1961).

9. P. Wynblatt and D. Chatain, *Anisotropy of Segregation at Grain Boundaries and Surfaces*, Metallurgical and Materials Transactions A, 37[9]: 2595-2620, (2006).

10. D. Chatain, P. Wynblatt and G. S. Rohrer, *Equilibrium Crystal Shape of Bi-Saturated Cu Crystals at 1223K*, Acta Materialia, 53[15]: 4057-4064, (2005).

11. M. Ramamoorthy, D. Vanderbilt, R. D. King-Smith, *First Principles Calculations of the Energetics of Stoichiometric TiO_2 Surfaces*, Physical Review B, 49[23]: 16721-16727, (1993).

12. P. Nikolopoulos, Surface, *Grain-Boundary and Interfacial Energies in Al_2O_3 and Al_2O_3-Sn, Al_2O_3-Co systems*, Journal of Materials Science, 20[11]: 3993-4000, (1985).

13. J. Guo, D. E. Ellis and D. J. Lam, *Electronic Structure and Energetics of Sapphire (0001) and $(1\bar{1}02)$ Surfaces*, Physical Review B, 45[23]: 13647-13656, (1992).

14. M. Gautier, G. Renaud, L. Pham Van, B. Villette, M. Pollak, N. Thromat, F. Jollet and J. P. Duraud, *α-Al_2O_3 (0001) Surfaces: Atomic and Electronic Structure*, Journal of the American Ceramic Society, 77[2]: 323-34, (1994).

15. J. Ahn and J. W. Rabalais, *Composition and Structure of the Al_2O_3{0001}-(1X1) Surface*, Surface Science, 388[1-3]: 121-131, (1997).

16. I. Manassidis and M. J. Gillan, *Structure and Energetics of Alumina Surfaces Calculated from First Principles*, Journal of the American Ceramic Society, 77[2]: 335-38, (1994).

17. H. Sadan and W. D. Kaplan, *Au-Sapphire (0001) Solid-Solid Interfacial Energy*, Journal of Materials Science, 41[16]: 5099-5107, (2006).

18. J. C. Heyraud and J. J. Metois, *Equilibrium Shape and Temperature; Lead on Graphite*, Surface Science, 128[2-3]: 334-342, (1983).

19. M. Kitayama, T. Narushima and A. M. Glaeser, *The Wulff Shape of Alumina: II, Experimental Measurements of Pore Shape Evolution Rates*, Journal of the American Ceramic Society, 83[10]: 2572-2583, (2000).

20. G. Wulff, *Zur Frage der Geschwindigkeit des Wachstums und der Auflosung der Krystalflachen*, Z. Krystallogr. Mineral., 34: 449-530, (1901).

21. W. T. Read, Jr., *Dislocation in Crystals*, McGraw-Hill, New York, pp.153 (1953).

22. J. M. Howe, Interfaces in Materials: *Atomistic Structure, Thermodynamics and Kinetics of Solid/Vapor, Solid/Liquid and Solid/Solid Interfaces*, John Wiley & Sons, London, (1997).

23. C. Herring, *The Physics of Powder Metallurgy*, New York, McGraw-Hill Book Co. 143-179, (1951).

24. B. K. Hodgson and H. Mykura, *Torque Terms and Grain-Boundary Energy Measurement*, Journal of Materials Science, 8[4]: 565-570, (1973).

25. D. Chatain, V. Ghetta and P. Wynblatt, *Equilibrium Shape of Copper Crystals Grown on Sapphire*, Surface Science, 12[1]: 7-18, (2004).

26. K. H. Hansen, T. Worren, S. Stempel, E. Laegsgaard, M. Baumer, H. J. Freund, F. Besenbacher and I. Stensgaard, *Palladium Nano Crystals on Al_2O_3: Structure and Adhesion Energy*, Physical Review Letters, 83[20]: 4120-4123, (1999).

27. F. A. Nichols and W. W. Mullins, *Surface (Interface) and Volume-Diffusion Contributions to Morphological Changes Driven by Capillarity*, Transactions of the American Institute of Mining, Metallurgical and Petroleum Engineers, 233[10]: 1840-1848, (1965).

28. J. R. Heffelfinger, M. W. Bench and C. B. Carter, *Steps and the Structure of the (0001) α-Alumina Surface*, Surface Science, 370[1]: L168-L172, (1997).

29. C. Noguera, *Insulating Oxides in Low Dimensionality: A Theoretical Review*, Surface Review and Letters, 8[1-2]: 121-167, (2001).

30. *The Surface Science of Metal Oxides*, Faraday Discussions, 114: 1-465, (1999). Entire volume.

31. C. Verdozzi, P. A. Schultz, R. Wu, A. H. Edwards and N. Kioussis, *Layer Intermixing During Metal/Metal Oxide Adsorption: Ti/Sapphire (0001)*, Physical Review B, 66[12]: 125408 (1-4), (2002).

32. T. Young, *An Essay on the Cohesion of Fluids*, Philosophical Transactions of the Royal Society of London, 95:65-87, (1805).

33. A. Dupré, *Théorie Mécanique de la Chaleur*, Chapter IX, Actions Moléculaires (suite), published by Gauthier-Villars, Paris, (1869).

34. N. Eustathopoulos, M. G. Nicholas and B. Drevet, *Wettability at High Temperatures*, 43-48, Pergamon Materials Series, Edited by R. W. Cahn, (1999).

35. J. T. Klomp, *Ceramic Microstructures '86, Role of Interfaces*, (ed. J. A. Pask and A. G. Evans), 307, New York, Plenum Press, (1987)

36. E. Saiz, A. P. Tomsia and R. M. Cannon, *Ridging Effects on Wetting and Spreading of Liquids on Solids*, Acta Materialia, 46[7]: 2349-2361, (1998).

37. E. Saiz, R. M. Cannon and A. P. Tomsia, *Reactive Spreading: Adsorption, Ridging and Compound Formation*, Acta Materialia, 48[18-19]: 4449-4462, (2000).

38. E. Saiz, R. M. Cannon and A. P. Tomsia, *High-Temperaure Wetting and the Work of Adhesion in Metal/Oxide Systems*, The Annual Review of Materials Research, 38: 197-226, (2008).

39. G. Levi, G. J. Abbaschian and R. Mehrabian, *Interface Interactions During Fabrication of Aluminum Alloy-Alumina Fiber Composites*, Metallurgical and Materials Transactions A, 9A[5]:697-711, (1978).

40. D. Chatain, F. Chabert and V. Ghetta, *New Experimental Setup for Wettability Characterization Under Monitored Oxygen Activity: I, Role of Oxidation State and Defect Concentration on Oxide Wettability by Gold*, Journal of the American Ceramic Society, 76[6]: 1568-1576, (1993).

41. B. Gallois, *Contribution to the Physical Chemistry of Metal-Gas and Metal-Alumina Interfaces*, Ph.D. Thesis, Carnegie Mellon University, Pittsburgh, PA, 1980.

42. I. Rivollet, D. Chatain and N. Eustathopoulos, *Mouillabilite de L'alumine Monocristalline par l'or et L'etain Entre Leur Point de Fusion et 1673K*, Acta Metallurgica, 35[4]: 835-844, (1987).

43. N. Eustathopoulos, M. G. Nicholas and B. Drevet, *Wettability at High Temperatures*, Pergamon Materials Series Vol. 3, Ed. R. W. Cahn, Pergamon, (1999).

44. R. Sangiorgi, G. Caracciolo and A. Passerone, *Factors Limiting the Accuracy of Measurements of Surface Tension by the Sessile Drop Method*, Journal of Materials Science, 17[10]:2895-2901, (1982).

45. J. C. Heyraud and J. J. Metois, *Equilibrium Shape of Gold Crystallites on a Graphite Cleavage Surface: Surface Energies and Interfacial Energy*, Acta Metallurgica, 28[12]: 1789-1797, (1980).

46. J. Lee, H. Ishimura and T. Tanaka, *Anisotropy of Wetting of Molten Au on Differently Oriented α-Al_2O_3 Single Crystals*, Scripta Materialia, 54[7]: 1369-1373, (2006).

47. W. L. Winterbottom, *Equilibrium Shape of a Small Particle in Contact With a Foreign Substrate*, Acta Metallurgica, 15[2]: 303-310, (1967).

48. D. McLean, *Grain Boundaries in Metals*, Oxford Press, London, 116-122, (1957).

49. R. Defay and I. Prigogine, A. Bellmans and D. H. Everett, *Surface Tension and Adsorption*, Wiley, New York, NY, 158-197, (1966).

50. P. Wynblatt and R. C. Ku, *Surface Energy and Solute Strain Energy Effects in Surface Segregation*, Surface Science, 65[2]: 511-531, (1977).

51. P. Wynblatt and R. C. Ku, *Interfacial Segregation*, Eds. W. C. Johnson and J. M. Blakely, ASM, Metals Park, OH, 115-136, (1979).

52. Y. W. Lee and H. I. Aaronson, *Surface Concentration Profile and Surface Energy in Binary Alloys*, Surface Science, 95[1]: 227-244, (1980).

53. Y. W. Lee and H. I. Aaronson, *Anisotropy of Coherent Interphase Boundary Energy*, Acta Metallurgica. 28[4]: 539-548, (1980).

54. E. D. Hondros, M. P. Seah, S. Hofmann and P. Lejcek, *Physical Metallurgy*, Ed. R. W. Cahn and P. Haasen, vol. II, Elsevier Science, 1202, (1996).

55. W. C. Mackrodt, *Ceramic Microstructures '86, Role of Interfaces*, Ed. J. A. Pask and A. G. Evans, New York, Plenum Press, 271, (1987).

56. W. D. Kingery, *Ceramic Microstructures '86, Role of Interfaces*, Ed. J. A. Pask and A. G. Evans, New York, Plenum Press, 281, (1987).

57. D. M. Lipkin, D. R. Clarke and A. G. Evans, *Effect of Interfacial Carbon on Adhesion and Toughness of Gold-Sapphire Interfaces*, Acta Materialia, 46[13]: 4835-4850, (1998).

58. G. Elssner, T. Suga and M. Turwitt, *Fracture of Ceramic to Metal Interfaces*, Journal de Physique Colloques, 46[C4]: C4-597-C4-612, (1985).

59. H. Fecht and H. Gleiter, *A Lock-In Model for the Atomic Structure of Interphase Boundaries Between Metals and Ionic Crystals*, Acta Metallurgica, 33[4]: 557-562, (1985).

60. D. A. Mortimer and M. G. Nicholas, *Ceramic/Metal Joining for Structural Applications*, Materials Science and Technology, 1[9]:657-665, (1985).

61. M. G. Nicholas, *Surface and Interfaces of Ceramic Materials*, (Ed. L. C. Dufour et al.), Norwell, MA, Kluwer Academic, 393, (1989).

62. H. Pulfrich, *Ceramic to Metal Seal*, U.S Patent 2,163,407 and 2,163,409, (1937).

63. H. Pulfrich, *Vacuum Tight Seal*, U.S Patent 2,163,408, (1937).

64. H. Pulfrich and R. Magner, *Ceramic to Metal Seal*, U.S Patent 2,163,410, (1937).

65. H. J. Nolte and R. F. Spurck, *Metal-Ceramic Sealing with Manganese*, Television Engineering, 1[11]:14-16, 18, 39, (1950).

66. G. R. Van Houten, *A Survey of Ceramic to Metal Bonding*, Journal of American Ceramic Society Bulletin, 38[6]: 301-307, (1959).

67. S. S. Cole Jr. and G. Sommer, *Glass Migration Mechanism of Ceramic to Metal Seal Adherence*, Journal of American Ceramic Society, 44[6], 265-271, (1961).

68. A. G. Pincus, *Metallographic Examination of Ceramic to Metal Seals*, Journal of American Ceramic Society, 36[5]: 152-158, (1953).

69. W. D. Kingery, *Densification During Sintering in the Presence of a Liquid Phase. I. Theory*, Journal of Applied Physics, 30[3]: 301-306, (1959).

70. M. Ushio and Y. Sumiyoshi, *The Wetting of an Alumina Substrate by Liquid Silver*, Bulletin of the Chemical Society of Japan, 60[6]: 2041-2045, (1987).

71. R. R. Kappor, E. S. Podszus and T. W. Eagar, *Wettability of Silver Based Reactive Metal Brazing Alloys on Alumina*, Scripta Metallurgica, 22[8]: 1277-1279, (1988).

72. O. M. Akselsen, *Review - Advances in Brazing of Ceramics*, Journal of Materials Science, 27[8]: 1989-2000, (1992).

73. J. G. Li, *Kinetics and Spreading of Cu-Ti Alloys on Alumina and Glassy Carbon Substrates*, Journal of Materials Science Letters, 11[23]: 1551-1554, (1992).

74. A. Meier, M. D. Baldwin, P. R. Chidambaram and G. R. Edwards, *The Effects of Large Oxygen Additions on the Wettability and Work of Adhesion of Copper-Oxygen Alloys on Polycrystalline Alumina*, Materials Science and Engineering A, 196[1-2]: 111-117, (1995).

75. P. Kritsalis, L. Coudurier and N. Eustathpoulos, *Contribution to the Study of Reactive Wetting in the $CuTi/Al_2O_3$ System*, Journal of Materials Science, 26[12]: 3400-3408, (1991).

76. A. Meier, M. D. Baldwin, P. R. Chidambaram and G. R. Edwards, *Generation of Isothermal Spreading Data and Interfacial Energy Data for Liquid Reactive Metals on Ceramic Substrates: The Copper-Titanium/Alumina System*, Journal of Materials Science, 30[5]: 3791-3798, (1995).

77. L. Gremillard, E. Saiz, J. Chavalier and A. P. Tomsia, *Wetting and Strength in the Tin-Silver-Titanium/Sapphire System*, Zeitschrift fur Metallkunde - International Journal of Materials Research and Advanced Techniques, 95[4]: 261-265, (2004).

78. P. T. Vianco, J. J. Stephens, P. F. Hlava and C. A. Walker, *Titanium Scavenging on Ag-Cu-Ti Active Braze Joints*, Welding Journal, 82[10]: 238.S-277.S, (2003).

79. C. Valette, M. F. Devismes, R. Voytovych and N. Eustathoupolos, *Interfacial Reactions in Alumina/CuAgTi Braze/CuNi System*, Scripta Materialia, 52[1]: 1-6, (2005).

80. N. Frage, N. Froumin, M. Aizenshtein, L. Kutsenko, D. Fuks and M. P. Dariel, *Reactive Wetting in Titanium Carbide/Non-Reactive Metal Systems*, Current Opinions in Solid State and Materials Science, 9[4-5]: 189-195, (2005).

81. E. Saiz, A. P. Tomsia and R. M. Cannon, *Ridging Effects on Wetting and Spreading of Liquids on Solids*, Acta Materialia, 46[7]: 2349-2361, (1998).

82. E. Saiz, R. M. Cannon and A. P. Tomsia, *Reactive Spreading: Adsorption, Ridging and Compound Formation*, Acta Materialia, 48[18-19]: 4449-4462, (2000).

83. E. Saiz, A. P. Tomsia and R. M. Cannon, *Triple Line Ridging and Attachment in High-Temperature Wetting*, Scripta Materialia, 44[1]: 159-164, (2001).

84. E. Saiz, R. M. Cannon and A. P. Tomsia, *Reactive Spreading in Ceramic/Metal Systems*, Oil and Gas Science and Technology, 56[1]: 89-96, (2001).

85. W. W. Mullins, *Theory of Thermal Grooving*, Journal of Applied Physics, 28[3]: 333-339, (1957).

86. E. Saiz, R. M. Cannon and A. P. Tomsia, *High-Temperature Wetting and the Work of Adhesion in Metal/Oxide Systems*, The Annual Review of Materials Research, 38:197-226, (2008).

87. G. Kaptay, *A Unified Model for the Cohesive Enthalpy, Critical Temperature, Surface Tension and Volume Thermal Expansion Coefficient of Liquid Metals of BCC, FCC and HCP Crystals*, Materials Science and Technology A, 495[1-2]: 19-26, (2008).

88. P. Xiao, B. Derby, J. Webster and J. Penfold, *The Characterization of Metal/Ceramic Interfaces Using Specular Neutron Reflection*, Acta Materialia, 45[1]: 273-279, (1997).

89. B. Derby, P. Xiao and J. Webster, *Neutron Reflection Studies of Titanium Segregation to Metal-Ceramic Interfaces*, Physica B, 248[1-4]:304-309, (1998).

90. N. Froumin, S. Barzilai, M. Aizenshtein, M. Lomberg and N. Frage, *Wetting Induced by Near-Surface Ti-Enrichment in the CaF_2/In-Ti and CaF_2/Cu-Ti Systems*, Materials Science and Engineering A, 495[1-2]: 181-186, (2008).

91. N. Eustathopoulos, *Dynamics of Wetting in Reactive Metal/Ceramic Systems*, Acta Materialia, 46[7]: 2319-2327, (1998).

92. O. Dezellus, N. Eustathopoulos, Fundamental Issues of Reactive Wetting by Liquid Metals, Journal of Materials Science, Euromat 2009, published online 8 January 2010.

93. K. Landry and N. Eustathopoulos, *Dynamics of Wetting in Reactive Metal/Ceramic Systems: Linear Spreading*, Acta Materialia, 44[10]: 3923-3932, (1996).

94. K. Landry, C. Rado, R. Voytovich and N. Eustathopoulos, *Mechanisms of Reactive Wetting: The Question of Triple Line Configuration*, Acta Materialia, 45[7]: 3079-3085, (1997).

95. N. Eustathopoulos, *Progress in Understanding and Modeling Reactive Wetting of Metals on Ceramics*, Current Opinions in Solid State and Materials Science, 9[4-5]: 152-160, (2005).

96. O. Dezellus, F. Hodaj, C. Rado, J. N. Barbier and N. Eustathopoulos, *Spreading of Cu-Si Alloys on Oxidized SiC in Vacuum: Experimental Results and Modelling*, Acta Materialia, 50[5]: 979-991, (2002).

97. O. Dezellus, F. Hodaj, N. Eustathopoulos, *Progress in Modeling of Chemical-Reaction Limited Wetting*, Journal of the European Ceramic Society, 23[15]: 2797-2803, (2003).

98. A. B. D. Cassie and S. Baxter, *Wettability of Porous Surfaces*, Transactions of the Faraday Society, 40: 546-551, (1944).

99. O. Dezellus, F. Hodaj and N. Eustathopoulos, *Chemical Reaction-Limited Spreading: The Triple Line Velocity Versus Contact Angle Relation*, Acta Materialia, 50[19]: 4741-4753, (2002).

100. M. L. Muolo, E. Ferrera, L. Morbelli and A. Passerone, *Wetting, Spreading and Joining in the Alumina-Zirconia-Inconel 738 System*, Scripta Materialia, 50[3]: 325-330, (2004).

101. R. Voytovich, F. Robaut and N. Eustathopoulos, *The Relation Between Wetting and Interfacial Chemistry in the CuAgTi/Alumina System*, Acta Materialia, 54[8]: 2205-2214, (2006).

102. J. J. Stephens, F. M. Hosking, T. J. Headley, P. F. Hlava and F. G. Yost, *Reaction Layers and Mechanisms for a Ti-Activated Braze on Sapphire*, Metallurgical and Materials Transactions A, 34[12]: 2963-2972, (2003).

103. A. H. Carim, *Convergent-Beam Electron Diffraction "Fingerprinting" of M_6X Phases at Brazed Ceramic Joints*, Scripta Metallurgica et Materialia, 25[1]: 51-54, (1991).

104. G. P. Kelkar, A. H. Carim, *Synthesis, Properties and Ternary Phase Stability of M_6X Compounds in the Ti-Cu-O System*, Journal of the American Ceramic Society, 76[7], 1815-1820, (1993).

105. A. Mortensen, B. Drevet and N. Eustathopoulos, *Kinetics of Diffusion-Limited Spreading of Sessile Drops in Reactive Wetting*, Scripta Materialia, 36[6]: 645-651, (1997).

106. O. V. Durov and V. P. Krasovskyy, *In Situ Observation of Ag-Cu-Ti Liquid Alloy/Solid Oxide Interfaces*, Materials Science and Engineering A, 495[1-2]: 164-167, (2008).

107. R. Voytovych, L. Y. Ljungberg and N. Eustathopoulos, *The Role of Adsorption and Reaction in Wetting in the CuAg-Ti/Alumina System*, Scripta Materialia, 51[5]: 431-435, (2004).

108. M. L. Santella, J. A. Horton and J. J. Pak, *Microstructure of Alumina Brazed With a Silver-Copper-Titanium Alloy*, Journal of the American Ceramic Society, 73[6]: 1785-1787, (1990).

109. L. Gremillard, E. Saiz, V. R. Radmilovic and A. P. Tomsia, *Role of Titanium on the Reactive Spreading of Lead-Free Solders on Alumina*, Journal of Materials Research, 21[12]: 3222-3233, (2006).

110. D. P. Woodruff, *The Chemical Physics of Solid Surfaces, Volume 9: Oxide Surfaces*, Elsevier Science B. V. 2001.

111. R. H. French and A. H. Heuer, *Science of Alumina*, Journal of the American Ceramic Society, 77[2]: 292, (1994).

112. M. Gautier, J. P. Duraud and L. Pham Van, *Influence of the Al_2O_3(0001) Surface Reconstruction on the Cu/Al_2O_3 Interface*, Surface Science Letters, 249[1-3]: L327-L332, (1991).

113. T. J. Godin and P. LaFemina, *Atomic and Electronic Structure of the Corundum (α-Alumina) Surface*, Physical Review B, 49[11]: 7691-7696, (1994).

114. M. Causa, R. Dovesi, C. Pissani and C. Roetti, *Ab Initio Characterization of the (0001) and ($10\bar{1}0$) Crystal Faces of α-Al_2O_3*, Surface Science, 215[1-2]: 259-271, (1989).

115. A. Kirfel and K. Eichorn, *Accurate Structure Analysis with Synchrotron Radiation. The Electron Density in Al_2O_3 and Cu_2O*, Acta Crystallographica Section A, A46[4]: 271-284, (1990).

116. Y. Shiratsuchi, M. Yamamoto and Y. Kamada, *Surface Structure of Self-Organized Sapphire (0001) Substrates with Various Inclined Angles*, Japanese Jounral of Applied Physics, 41[9A]: 5719-5725, (2002).

117. R. J. Kershner, J. W. Bullard and M. J. Cima, *Zeta Potential Orientation Dependence of Sapphire Substrates*, Langmuir 20[10]: 4101-4108, (2004).

118. H. E. Swanson and E. Tatge, *Data for 54 Inorganic Substances*, National Bureau of Standards Circular, 539[1]: 95, (1953).

119. R. Sailer and G. McCarthy, *JCPDS 44-1294 (α-titanium)*, International Centre for Diffraction Data, (1993).

120. Y. V. Naidich, *The Wettability of Solids by Liquid Metals*, Progress in Surface and Membrane Science, 353-484, Ed. By D. A. Cadenhead and J. F. Danielli, Academic Press, London, UK, (1981).

121. R. M. Pilliar and J. Nutting, *Solid-Solid Interfacial Energy Determinations in Metal-Ceramic Systems*, Philosophical Magazine, 16[139]: 181-188, (1967).

122. Z. Wang and P. Wynblatt, *Alloying Effects of Sn and Si on Wetting and Energetics of Solid Au/SiC Interfaces*, Materials Science and Engineering A, A259[2]: 287-295, (1999).

123. Z. Wang and P. Wynblatt, *Wetting and Energetics of Solid Au and Au-Ge/SiC Interfaces*, Acta Materialia, 46[14]: 4853-4859, (1998).

124. Y. V. Naidich, V. S. Zhuravlev and V. G. Chuprina, *Adhesion, Wetting and the Formation of Intermediate Phases in Titanium-Containing Melt-Oxide Systems*, Communication 2, Soviet Powder Metallurgy and Metal Ceramics, 13[3]: 82-85, (1974).

125. M. Singh, T. P. Shpargel, R. Asthana, *Brazing of Stainless Steel to Yttria Stabilized Zirconia Using Gold-Based Brazes for Solid Oxide Fuel Cell Applications*, International Journal of Applied Ceramic Technology, 4[2]: 119-133, (2007).

126. Z. Wang and P. Wynblatt, *The Equilibrium Form of Pure Gold Crystals*, Surface Science, 398[1-2]: 259-266, (1998).

127. R. Heffelfinger, M. W. Bench, C. B. Carter, *On the Faceting of Ceramic Surfaces*, Surface Science, 343[1-2]: L1161-L1166, (1995).

128. H. Choi, D. Y. Kim, B. J. Hockey, S. M. Wiederhorn, C. A. Handwerker, J. E. Blendell, W. C. Carter and A. R. Roosen, *Equilibrium Shape of Internal Cavities in Sapphire*, Journal of the American Ceramic Society, 80[1]: 62-68, (1997).

129. J. L. Murray, *The Au-Ti (Gold-Titanium) System*, Journal of Phase Equilibria, 4[3]: 278-283, (1983).

130. V. G. M. Sivel, J. Van Den Brand, W. R. Wang, H. Mohdadi, F. D. Tichelaar, P. F. A. Alkemade and H. W. Zandbergen, *Application of the Dual-Beam FIB/SEM to Metals Research*, Journal of Microscopy, 214[3]: 237-245, (2003).

131. M. Baram and W. D, Kaplan, *Quantitative HRTEM Analysis of FIB Prepared Specimens*, Journal of Microscopy, 232[3]: 395-405, (2008).

132. J. C. Heyraud and J. J. Metois, *Establishment of the Equilibrium Shape of Metal Crystallites on a Foreign Substrate: Gold on Graphite*, Journal of Crystal Growth, 50[2]: 571-574, (1980).

133. D. Brandon and W. D. Kaplan, *Microstructural Characterization of Materials, 2nd Edition*, John Wiley & Sons, (2008).

134. V. K. Kumikov and Kh. B. Khokonov, *On the Measurements of Surface Free Energy and Surface Tension of Solid Metals*, Journal of Applied Physics, 54[3]: 1346-1350, (1983).

135. R. E. Honig, *Vapor Pressure Data for the Solid and Liquid Elements*, R.C.A. Review, 23:567-586, (1962).

136. T. B. Massalski (editor in chief), *Binary Alloy Phase Diagrams*, Vol. 1, pp. 312, ASM 1986. original paper by H. Okamoto and T. B. Massalski, *Gold-Silicon Phase Diagram*, Alloy Phase Diagrams, 4[2], (1983).

137. S. Bernath, T. Wagner, S. Hofmann and M. Ruhle, *Interface Formation Between Ultra Thin Films of Titanium and (0001) Sapphire Substrates*, Surface Science, 400[1-3]: 335-344, (1998).

138. H. J. Kang, C. H. Kim, N. S. Park and M. W. Kim, *The Surface and Interface Reaction of Metal Thin Film on Sapphire Substrate*, Applied Surface Science, 100-101: 160-164, (1996).

139. M. Kitayama and A. Glaeser, *The Wulff Shape of Alumina: IV. Ti^{4+}-Doped Alumina*, Journal of the American Ceramic Society, 88[12]: 3492-3500, (2005).

140. P. Wynblatt, *Interfacial Segregation Effects in Wetting Phenomena*, The Annual Review of Materials Research, 38: 173-196, (2008).

141. H. P. Bonzel and M. Nowicki, *Absolute Surface Free Energies of Perfect Low-Index Orientations of Metals and Semiconductors*, Physical Review B, 70[24]: 245430-1-9, (2004).

142. C. J. Leadbeater, *The Surface Energies of Metals and Alloys*, Powder Metallurgy, 9: 1-21, (1951).

143. R. E. Loehman, A. P. Tomsia, *Wetting and Joining of Mullite Ceramics by Active-Metal Braze Alloys*, Journal of the American Society, 77[1]: 271-274, (1994).

144. V. J. Keast and D. B. Williams, *Quantitative Compositional Mapping of Bi Segregation to Grain Boundaries in Cu*, Acta Materialia, 47[15-16]: 3999-4008, (1999).

145. D. B. Williams and C. B. Carter, *Transmission Electron Microscopy. A Textbook for Materials Science*, Plenum Press. New York and London, (1996).

146. V. J. Keast and D. B. Williams, *Quantification of Boundary Segregation in the Analytical Electron Microscope*, Journal of Microscopy, 199[1]: 45-55, (2000).

147. D. B. Williams, J. R. Michael, J. I. Goldstein and D. A. Romig Jr., *Definition of the Spatial Resolution of X-Ray Microanalysis in Thin Foils*, Ultramicroscopy, 47[1-3]: 121-132, (1992).

148. J. I. Goldstein, J. L. Costley, G. W. Lorimer and S. J. B. Reed, *Quantitative X-Ray Analysis in the Electron Microscope*, Scanning Electron Microscopy (Ed. By O. Johari), IITRI Chicago, 315, (1977).

149. V. D. Scott and G. Love, *Quantitative Electron Probe Microanalysis*, Ellis Horwood Series PHYSICS, (1983).

150. P. Duncomb and S. J. B. Reed, *Quantitative Electron Probe Microanalysis*, Ed. K. F. J. Heinrich, National Bureau of Standards Special Publication 298, (Washington: US Department of Commerce), 133, (1968).

151. G. Cliff and G. W. Lorimer, *The Quantitative Analysis of Thin Films*, Journal of Microscopy, 103[2]: 203-207, (1975).

152. G. W. Lorimer, *Quantitative X-Ray Microanalysis of Thin Specimens in the Transmission Electron Microscope; A Review*, Mineralogical Magazine, 51[1]: 49-60, (1987).

153. C. Nockolds, M. J. Nasir and G. W. Lorimer, *Electron Microscopy and Analysis*, Ed. T. Mulvey, I.O.P London, 417, (1979).

154. S. F. Bauman and D. B. Williams, *A STEM/X-Ray Microanalytical Study of the Equilibrium Segregation of Bismuth in Copper*, Journal of Microscopy, 123[1]: 299-305, (1981).

155. J. R. Michael and D. B. Williams, *An Analytical Electron Microscope Study of the Kinetics of the Equilibrium Segregation of Bismuth in Copper*, Metallurgical and Materials Transactions A, 15[1]: 99-105, (1984).

השפעת טיטניום על
משטח הביניים מתכת-קרמיקה

אלעד נוסבאום

השפעת טיטניום על
משטח הביניים מתכת-קרמיקה

חיבור על מחקר

לשם מילוי חלקי של הדרישות לקבלת תואר מגיסטר
למדעים בהנדסת חומרים

אלעד נוסבאום

הוגש לסנט הטכניון - מכון טכנולוגי לישראל

ניסן תשע״א חיפה אפריל 2011

תודות

מחקר זה נעשה תחת הנחיית פרופ׳ וויין ד. קפלן מהפקולטה להנדסת חומרים בטכניון - מכון טכנולוגי לישראל וכמחקר משותף יחד עם רפאל - מערכות הגנה מתקדמות.

ברצוני להביע את תודתי והערכתי לפרופ׳ וויין ד. קפלן על ההנחיה, הסבלנות ושיתוף הפעולה במחקר זה.

ברצוני להביע את תודתי לרפאל - מערכות הגנה מתקדמות, על כך שנתנה לי את ההזדמנות, האפשרות והמימון הכספי לבצע מחקר זהת על השימוש במתקנים ובתשתיות השונות ועל תמיכה בלתי נלאית. תודה מיוחדת ניתנת לד״ר אפרים ו. ויגאל פ. על התמיכה הקרובה והאישור לתואר ולמחקר, נתן ג., צביקה ב., נאוה כ., אבי מ., מיכל ס., יורם מ. ואריה מ. על התמיכה אותה העניקו לי ועל הגיבוי בזמנים בהם נעדרתי, שלומית ז. וזיו א. על הייעוץ, סיעור המוחות, התמיכה והעזרה באנאליזה ולד״ר שי ז., על ההתייעצויות והעזרה באנאליזת דיפרקציית קרני איקס ועוד.

ברצוני להודות גם לחברי קבוצת המחקר של פרופ׳ וויין ד. קפלן, Metal-Ceramic Interface group, בפקולטה להנדסת חומרים בטכניון - מכון טכנולוגי לישראל. תודה ענקית ומיוחדת ניתנת להילה סדן-מלצמן על שעות אין סופיות של דיונים, שעות TEM, אין סוף שיחות טלפון ומסרונים (SMS) והנחייה. תודתי נתונה גם לד״ר ציפי כהן היימס על עזרתה האדירה ב-FIB, ד״ר ירון קאופמן, מור ברעם ומירי דרוזדוב על העזרה ב-TEM ועל דיונים פוריים, מייק ליברטל על התמיכה והעזרה בנושאי מחשוב ומשה כץ על העזרה הטכנית האדירה בעריכת הניסויים.

תודה מיוחדת ניתנת גם לד״ר אלכס ברנר, על העזרה ב-SEM ועל ההנחיה בנושאי חישוב סף הגילוי.

הקדשה

ברצוני להקדיש עבודה זו למשפחתי שלי, אשתי ושני ילדיי (אשר נולדו במהלך תקופת המחקר), על כך שעמדו לצידי כל הזמן, תמכו, עודדו, עזרו ובעיקר חיכו בסבלנות ארבע שנים ארוכות עד לתום העבודה.

תוכן עניינים

תקציר.....I

רשימת סמלים וקיצורים.....III

1. הקדמה.....1

2. סקר ספרות.....3

2.1. אנרגיית פני שטח של מוצקים.....3

2.2. צורת שיווי המשקל (ECS).....8

2.3. פרמטרים תרמו דינאמיים במשטח הביניים מתכת-קרמיקה.....14

2.3.1. זוויות מגע והעבודה התרמו דינאמית של אדהזיה.....14

2.3.2. חישוב פרמטרים תרמו דינאמיים - מהלך ניסויים.....18

2.3.2.1. ניסויי טיפה - Sessile Drop.....18

2.3.2.2. ניסויי הרטבה (Dewetting).....20

2.3.2.3. אנאליזת Winterbottom.....22

2.3.2.4. סגרגציה לפני שטח ולמשטחי ביניים.....26

2.3.2.5. יחסי אוריינטציה במשטחי ביניים מוצק-מוצק.....27

2.4. חיבורי מתכת-קרמיקה, התפשטות והתפשטות ריאקטיבית.....28

2.4.1. התפשטות המוכתבת על ידי ספיחה/היווצרות רכס (גישת "ספיחה קודמת").....31

2.4.2. התפשטות המוכתבת על ידי תוצר הריאקציה.....37

2.5. מערכת זהב - טיטניום - ספיר.....43

2.5.1. צורות שיווי המשקל.....46

2.5.1.1. צורת שיווי המשקל של זהב.....46

2.5.1.2. צורת שיווי המשקל של ספיר.....47

3. מטרות המחקר.....48

4. שיטות ותהליכים ניסיוניים.....49

4.1. ניסויי הרטבה (Dewetting) ושיווי משקל (מערכת זהב-טיטניום-ספיר).....49

4.2. אפיון מיקרו מבנה של סגסוגת ברייזינג מסחרית פעילה על בסיס זהב.....52

4.3. שיטות אפיון.....53

4.3.1. הכנת דגם TEM.....54

5. תוצאות.....55

5.1. ניסויי הרטבה (Dewetting) ושיווי משקל (מערכת זהב-טיטניום-ספיר).....55

5.1.1. מורפולוגית החלקיקים וצורתם 55
5.1.2. אפיון SEM ו-EDS..... 56
5.1.3. אפיון TEM..... 58
5.1.4. מורפולוגית החלקיקים וצורתם - ניסוי הרטבה שני..... 63
5.1.5. אפיון TEM - ניסוי הרטבה שני..... 66
5.2. סגסוגת ברייזינג פעילה מסחרית על בסיס זהב (gold ABA®)..... 77
5.2.1. אפיון SEM ו-EDS של משטח הביניים זהב-ספיר 77
5.2.2. אפיון TEM של משטח הביניים זהב-ספיר..... 79
6. דיון..... 83
6.1. ניסויי הרטבה (Dewetting) ושיווי משקל..... 83
6.1.1. מורפולוגיית החלקיקים שבשיווי משקל וצורתם..... 83
6.1.2. משטח הביניים זהב-ספיר..... 90
6.1.3. אנרגיית משטח הביניים זהב (טיטניום)-ספיר..... 91
6.2. מבנה משטח הביניים זהב (gold ABA®)-ספיר..... 94
7. סיכום ומסקנות..... 98
8. המלצות למחקר עתידי..... 101
נספח מס' 1: גבול גילוי - תיאוריה וחישובים..... 102
1.1. רקע תיאורטי..... 102
1.2. דגמים דקים..... 104
1.3. חישוב סף הגילוי..... 110
מקורות ספרות..... 114

תקציר

משטחי ביניים מתכת-קרמיקה נמצאים בליבם של יישומים תעשייתיים ומחקריים רבים מספור בתחומי עניין שונים ומגוונים. תחומים נפוצים הם מיקרו-אלקטרוניקה, רפואה, תעשיית הרכב והחלל, טכנולוגיית שכבות דקות ועבות, מערכות ואקום, לייזרים ועוד רבים אחרים. הודות לכך, משטחי ביניים אלו נלמדים ונחקרים לעומק מאז אמצע המאה ה-20. ההתקדמות והשיפורים אשר חלו בעשרים-שלושים השנים האחרונות בתחום אפיון החומרים בכלל ובתחום המיקרוסקופים האלקטרוניים (על סוגיהם השונים) בפרט מאפשר כיום לבצע אנאליזה מדוקדקת של משטחי ביניים אלו.

יישומים רבים בהם קיימים משטחי ביניים מסוג זה דורשים את חיבורו של חלק מתכתי לחלק קראמי. לסוג חיבור זה ישנן מגבלות רבות כאשר העיקריות שבהן נובעות מאי-התאמה בין מקדמי ההתפשטות התרמיים של שני החומרים השונים זה מזה ומההבדלים בתכונות הפיזיקאליות. לבעיות אלו ניתן מענה לרוב על ידי בחירה נכונה של חומרים לחיבורים מסוג זה ועל ידי תכן מכאני מתאים. בעיה נוספת אליה יש לתת מענה בעת חיבור נמסוג זה היא בעיית אי ההרטבה של פני השטח הקראמיים. רוב המתכות המשמשות כיום בתעשייה מרטיבות את פני שטח של הרכיב הקראמי בצורה גרועה ביותר ($90^o<\theta<180^o$) וכתוצאה מכך איכות המחבר הנוצר וחוזקו המכאני נמוכים ביותר. על מנת להתגבר על בעיית זו, פותחו שיטות חיבור שונות. שתי השיטות הנפוצות ביותר בשימוש כיום ליצירת משטחי ביניים מסוג מתכת-קרמיקה הן שיטת המטאליזציה (Metallization process) ושיטת החיבור הפעיל (Active Brazing process). בשיטה המטאליזציה, שכבה מתכתית מיושמת על פני השטח הקראמיים ולאחר מכן מסונטרת על פניהם. החיבור אל החלק המתכתי נעשה לאחר מכן באמצעות תהליך ברייזינג (Brazing), לרוב באווירת ואקום או מימן. בשיטת החיבור הפעיל, תוספות של יסודות פעילים (כדוגמת טיטניום, ונדיום, הפניום ועוד) לסגסוגות חומרי הלחם מאפשרת למעשה לבצע חיבור מתכת לקרמיקה בתהליך אחד. בשיטה זו, ספיחה של המרכיב הפעיל אל משטח הביניים מתכת-קרמיקה משפרת את ההרטבה ומורידה את אנרגיית פני השטח שם.

על בסיס השיטה האחרונה פותחו שתי תיאוריות מובילות במהלך עשרים-שלושים השנים האחרונות בנוגע לתפקידו של המרכיב הפעיל בהרטבה/התפשטות ריאקטיבית ואלו גם נפוצות כיום. התיאוריה הראשונה (N. Eustathopoulos ושותפיו) המבוססת על מודל תוצר הריאקציה (RPC - Reaction Product Control), טוענת כי השיפור המתקבל בהרטבה כתוצאה מתוספת של מרכיב פעיל הינו הודות ליצירת תוצר ריאקציה במשטח הביניים מתכת-קרמיקה, כתוצאה מריאקציה בין המרכיב הפעיל ופני השטח הקראמיים. על פי תיאוריה זו, סגסוגת חומר הלחם יכולה להרטיב כעת את תוצר הריאקציה במקום את פני השטח הקראמיים. כך מתאפשרת הקטנה של זווית המגע ושיפור באיכותו של המחבר המתקבל. התיאוריה השנייה (E. Saiz, R. M. Cannon, A. P. Tomsia ושותפיהם) טוענת כי הספיחה של המרכיב הפעיל במשטח הביניים מתכת-קרמיקה היא האחראית לבדה על השיפור בהרטבה. ספיחה זו תורמת לירידה באנרגיית משטח הביניים מתכת-קרמיקה ולעלייה בעבודת האדהזיה.

מטרת עבודה זו היא לנסות ולהבהיר מהי השפעתו של הטיטניום (כתוספת של מרכיב פעיל) על משטחי ביניים מסוג מתכת-קרמיקה.

במהלך הניסויים שנערכו, פילם משולב של זהב-טיטניום-זהב עבר הרטבה במצב הנוזלי (1100 מע' צלזיוס) על פני מצע ספיר בעל אוריינטציה (0001) ותחת אווירה מבוקרת (גז ארגון 99.999% אשר הועבר דרך מלכודת לחמצן שנבנתה משבבי נחושת וטיטניום), אשר אפשרה לקיים תהליך עם לחץ חלקי של חמצן בערך של 10^{-21} atm. במהלך תהליך ההרטבה נוצרו חלקיקים בגודל מיקרוני ותת-מיקרוני אשר לאחר מכן עברו טיפול תרמי במצב המוצק ב-900 מע' צלזיוס, על מנת להביאם למצב של שיווי משקל. הדגם שעבר את התהליך אופיין בדיפרקציית קרני איקס לקביעת אוריינטציה מועדפת של החלקיקים על פני מצע הספיר, מיקרוסקופ אלקטרונים סורק (SEM) לאפיון מורפולוגית החלקיקים ובמיקרוסקופ אלקטרונים חודר (TEM) לבחינת משטח הביניים זהב-ספיר.

החלקיקים אשר נוצרו במהלך תהליך ההרטבה היו עגולים בצורתם, אך הכילו פאות בעלות גודל קטן אשר היו מקושרות ביניהן על ידי משטחים מעוגלים גדלים. דיפרקציית קרני איקס של כל הדגם הראתה כי זהב (111) הוא האוריינטציה המועדפת של החלקיקים על גבי מצע הספיר (0001) ואילו דיפרקציית אלקטרונים הראתה כי אותו יחס אוריינטציה קיים עבור מישורי האינדקסים הנמוכים (low-index orientation relationship) עבור חלקיק בודד. בחינה של משטח הביניים זהב-ספיר הראתה כי שכבת ספיחה (אדסורפציה) בעלת סדר חלקי המכילה אטומי טיטניום נוצרה שם ועובייה כ-1~ ננומטר. על מנת לאפיין את ריכוז הטיטניום בשכבת הספיחה הזו הוכן דגם ייחוס (standard) של סגסוגת זהב וטיטניום, אשר על בסיסו חושב פקטור הכיול עבור זהב וטיטניום, $k_{Au\text{-}Ti}$. שימוש בפקטור כיול זה אפשר חישוב של סף הגילוי עבור טיטניום בדגם הנבדק כמו גם מדידה וחישוב של ריכוז הטיטניום העודף (excess) במשטח ביניים זה. ריכוז זה חושב כ- 2.2 אטומי טיטניום לננומטר מרובע, ריכוז המתייחס לממוצע של 0.2 מונולייר. שכבת ספיחה (אדסורפציה) המכילה אטומי טיטניום, בעובי קטן יותר נצפתה גם כן כאשר היא מכסה את פני השטח החופשיים של הספיר, מחוץ לגבולות חלקיק הזהב ותורמת לירידה באנרגיית פני השטח של הספיר. באותו אופן חושב ריכוז הטיטניום העודף (excess) שם ונמצא כי הוא כ- 4.6 אטומי טיטניום לננומטר מרובע. ריכוז זה מתייחס לממוצע של 0.5 מונולייר.

על מנת לחשב את אנרגיית משטח הביניים זהב-ספיר במערכת הנוכחית נבחנו שתי שיטות - על פי יאנג ועל פי אנאליזת Winterbottom. לאחר בחינה של הצומת המשולשת (triple junction) הובהר כי שיטת יאנג איננה ניתנת ליישום במערכת מסוג זה שכן היא איננה מתחשבת בביטויי המומנט (torque term) בנקודת הצומת וכי אין ודאות כי לא קיימת פאה (facet) בפני השטח של החלקיק באזור זה. לאור זאת, אנאליזת Winterbottom שימשה לחישוב אנרגיית משטח הביניים ועבודת האדהזיה. עבור המערכת הנבדקת, לאחר שיווי משקל ב-900 מע' צלזיוס ותחת אווירה של ארגון מטוהר 99.999%, אנרגיית משטח הביניים שחושבה (ערך עליון אבסולוטי) היא γ_{SP} = 2.02±0.05 [J/m^2] ועבודת האדהזיה (ערך תחתון אבסולוטי) היא W_{ad} = 0.62±0.05 [J/m^2]. מאחר ואנרגיית פני השטח של מצע הספיר עם שכבת הספיחה לא חושבה, ערכים אלו ניתנים בצורה

המצוינת לעיל. ברור כי שכבת הספיחה תרמה לירידה באנרגיית פני השטח של מצע הספיר (אחרת לא הייתה קיימת שם) וכי אנרגיית משטח הביניים זהב-ספיר נמוכה יותר מהערך שצוין לעיל.

כאמצעי להשוואה כללית למערכת ברייזינג מסחרית בשיטת המתכת הפעילה, יוצר מחבר קרמיקה-קרמיקה ממצעי ספיר (0001) באמצעות ברייזינג בואקום עם סגסוגת פעילה מסוג gold-ABA®. משטח הביניים מתכת-קרמיקה שנוצר לאחר תהליך הברייזינג ב-1080 מע' צלזיוס למשך 30 דקות נבדק באמצעות TEM. 'איים' של תוצרי ריאקציה (תחמוצות טיטניום) לא רציפים נוצרו במשטח הביניים, ככל הנראה כתוצאה מחיזור פני השטח של הספיר על ידי הטיטניום. לא ניתן לדעת האם תחמוצות אלו נוצרו במהלך תהליך הברייזינג, בשלב בו סגסוגת הזהב הייתה במצבה הנוזלי, או מאוחר יותר במהלך הקירור, מאחר והדגם נבדק רק לאחר התהליך.

התוצאות אשר התקבלו בעבודה זו תומכות בתיאוריה לפיה הירידה באנרגיית משטח הביניים והשיפור בהרטבה מתקבלים כתוצאה מספיחה של המרכיב הפעיל (טיטניום במקרה הנוכחי) במשטח הביניים מתכת-קרמיקה.